MULTIWIRE PROPORTIONAL CHAMBER DEVELOPMENT

R.F. Doolittle, U. Pollvogt, A.J. Eskovitz
TRW Systems Group
One Space Park, Redondo Beach, Calif.

NAS9-11315

FINAL REPORT
January 1973

Prepared for
NATIONAL AERONAUTICS AND SPACE ADMINISTRATION
MANNED SPACECRAFT CENTER
HOUSTON, TEXAS 77058
CONTRACT NO. NAS9-11315

1. Report No.	2. Government Accession No.	3. Recipient's Catalog No.

4. Title and Subtitle	5. Report Date
Multiwire Proportional Chamber Development Final Report	January 1973
	6. Performing Organization Code
7. Author(s)	8. Performing Organization Report No.
R. F. Doolittle, U. Pollvogt, A. J. Eskovitz	
	10. Work Unit No.
9. Performing Organization Name and Address	
TRW Systems One Space Park Redondo Beach, California 90278	11. Contract or Grant No. NAS9-11315
	13. Type of Report and Period Covered Final Report 11-1-70 to 12-31-72
12. Sponsoring Agency Name and Address	14. Sponsoring Agency Code
National Aeronautics and Space Administration Manned Spacecraft Center Houston, Texas 77058	

15. Supplementary Notes

None

16. Abstract

This report describes theoretical and experimental work that has been carried out towards the development of large area multiwire proportional chambers, to be used as high resolution spatial detectors in cosmic ray experiments. A MWPC readout system was developed which uses a directly coupled, lumped element delay-line whose characteristics are independent of the MWPC design. A complete analysis of the delay-line and the readout electronic system shows that a spatial resolution of about 0.1 mm can be reached with the MWPC operating in the strictly proportional region. This was confirmed by measurements with a small MWPC and Fe-55 x-rays. A simplified analyis was carried out to estimate the theoretical limit of spatial resolution due to delta-rays, spread of the discharge along the anode wire, inclined trajectories, etc. To calculate the gas gain of MWPC's of different geometrical configurations a method was developed which is based on the knowledge of the first Townsend coefficient of the chamber gas. Good agreement between calculated and measured gas gains was obtained. Saturation of MWPC's was studied analytically and experimentally by comparing gas gain data obtained with Fe-55 x-rays and relativistic C^{12} and O^{16} nuclei at the Bevatron.

17. Key Words (Suggested by Author(s))	18. Distribution Statement
Multiwire Proportional Chamber High Resolution Spatial Detector for Cosmic Ray Experiments Delay-Line Readout System	Unclassified - Unlimited

19. Security Classif. (of this report)	20. Security Classif. (of this page)	21. No. of Pages	22. Price*
Unclassified	Unclassified	115	

* For sale by the National Technical Information Service, Springfield, Virginia 22151

TABLE OF CONTENTS

MULTIWIRE PROPORTIONAL CHAMBERS FOR TRAJECTORY MEASUREMENTS IN HIGH ENERGY COSMIC RAY EXPERIMENTS

1. INTRODUCTION

One of the most important measurements in high energy physics experiments - be it in elementary particle physics or in cosmic ray physics - is the exact determination of the trajectory of the particle or particles under investigation. In high energy cosmic ray experiments the trajectory of particles has to be known for the following reasons:

1. In order to determine the charge of a high energy (i.e., relativistic) charged particle with high resolution, it is necessary to know the location and length of the path of that particle through the charge measuring detectors, which can be scintillators, Cerenkov counters or ionization chambers.

2. In a magnetic spectrometer experiment such as the Superconducting Magnetic Spectrometer Experiment BCR-5[1] on HEAO-B the exact incoming and outgoing trajectory of the particle has to be known in order to determine the "bending" of the particle's path in the magnetic field. The amount of bending is a measure of the rigidity of the traversing particle and the direction of bending allows to distinguish between positively and negatively charged particles.

3. In an ionization spectrometer experiment such as the ACR-6[2] experiment on HEAO-A the trajectory of the incoming particle has to be measured in order to determine the shower axis of the resulting nuclear-electromagnetic cascade in the ionization spectrometer. The knowledge of the shower axis allows for certain corrections of the energy measurement due to the leakage of the cascade out of the side and bottom of the spectrometer.

4. In order to recognize and to determine the nature of simultaneous background particles (e.g., from backscattering from heavy absorbers like the Total Absorbtion Shower Counter in BCR-5 or the Ionization Spectrometer in ACR-6), it is necessary to simultaneously measure the trajectory of more than one particle which will then help to determine the trajectory of the primary particle.

5. A very important reason for measuring the trajectory of high energy cosmic ray particles is the investigation of anisotropy of the cosmic ray flux. Without good directional resolution it will not be possible to investigate anisotropies of a scale size that is smaller than the angular aperture of the experiment.

6. In magnetic spectrometer experiments like the one that was developed by R. Golden[3] of NASA's Manned Space Center in Houston for balloon flights and which will be developed for shuttle flights, spatial detectors are used in combination with nuclear emulsion to greatly increase the resolving power of such spectrometers and to extend their range to higher energies. The spatial detector locates the particle with sufficient accuracy to enable automatic location of tracks in the nuclear emulsion which has superior spatial resolution.

In the past mostly spark chambers were used to measure the trajectory of high energy particles and it is interesting to see that the original HEAO proposals for the BCR-5 and ACR-6 experiments contained spark chamber systems for trajectory measurements.

Since the successful operation of large area multiwire proportional chambers (MWPC) by Charpak et al.[4] at CERN in 1968, these detectors have come into widespread use, and a significant amount of development work has been done in recent years. The work at TRW was directed towards the development of large area MWPC-systems with high spatial resolution for eventual use in balloon and satellite experiments like the ones that were proposed for the HEAO missions and which will later be flown on shuttle. Much of the work on high resolution MWPC's is also applicable to the development of imaging proportional chambers for x-ray experiments in x-ray astronomy. Especially the delay-line readout technique for MWPC's is ideal for x-ray imaging proportional chambers.

This report describes the work that was performed by TRW under NASA contract No. NAS9-11315, towards the development of high resolution, large area MWPC's. In the following sections we present first a set of typical requirements for a spatial detector system for a cosmic ray experiment (Section 2). We discuss the advantages of MWPC's over spark chambers as

spatial detectors.

In Section 3 we give a short description of the principle of operation of MWPC's, and we present a summary of various readout systems which have been used and/or have been proposed. We close with a brief characterization of the lumped element delay-line concept which has been used at TRW. This leads into a summary of the parameters which influence the achievable spatial resolution.

After that we describe in more detail the experimental and theoretical work that has been carried out at TRW. Gas gain calculations and saturation effects due to space charge buildup are presented in Section 4, and the results of our gas gain measurements are presented. We then discuss in more detail limits on spatial resolution and the results of spatial resolution measurements (Section 5 and 7). A complete analysis of the lumped element dealy-line is given in Section 6. Section 8 presents our attempts to evaluate the delta-ray problem with the help of Monte Carlo calculations which were used to simulate delta-ray effects. In Section 9 we describe the results of a set of measurements we have carried out with MWPC's in a high energy (2.1 GeV/Nucleon), heavy ion beam (C^{12} and O^{16}) at the Bevatron. Some design considerations and results of load calculations for MWPC frames are presented in Section 10. All references which were used during preparation of this report are also listed. In addition we have compiled a bibliography of selected papers dealing with various aspects of MWPC's.

2. REQUIREMENTS ON SPATIAL DETECTORS IN SATELLITE EXPERIMENTS

The use of spatial detectors in high energy cosmic ray experiments on satellites imposes strict requirements on the design, construction and performance of the detectors due to limitations in available weight, volume and power and due to the requirement of high reliability and long lifetime.

A representative set of requirements are the requirements for the spatial detectors in the Superconducting Magnetic Spectrometer Experiment (BCR-5)

which was selected to fly on the HEAO-B spacecraft.

The experiment required 8 sets of detectors to measure the position of cosmic rays with unit charge up to Z=26 with a resolution of 0.1 mm in each set in X-and Y-direction. Assuming the position can be determined with an accuracy of 0.2 mm in a single spatial detector gap each set has to contain 8 gaps (4-x and 4-y) to achieve the required resolution per spatial detector set. This leads to a total of 64 gaps with the following parameters:

Effective area:	4 sets 66 cm x 53.3 cm
	4 sets 45 cm x 42 cm
Maximum Thickness:	4 inch per set
Weight:	52 lbs for large sets
	48 lbs for small sets
Average weight per gap:	approx. 6 lbs
Power dissipation:	4 watts per set
	or 500 mW per gap

It was further required that the septum width of the detector frame along the cryostat of the superconducting magnet be kept as small as possible in order to minimize the loss of high magnetic field regions for penetrating particles. The electronic readout system was required to measure two simultaneous trajectories for $Z \leq 2$ events. The lifetime of the experiment in orbit was to be at least one year and preferably two years.

2.1 MWPC vs Spark Chambers in Cosmic Ray Experiments

In this chapter we discuss the main advantages of MWPC's over spark chambers in high energy cosmic ray experiments (balloon-borne or satellite-borne). Because of these advantages the decision was made to replace spark chambers with MWPC's in the BCR-5 and ACR-6 experiments on HEAO. In addition to the advantages discussed here there are others which are responsible for the usefulness of MWPC's in nuclear and elementary particle physics experiments at accelerators, like the considerably higher event rate that a MWPC can process.

MWPC's operate with a dc-potential between anode and cathode and are constantly sensitive to penetrating particles. Because the recovery time is

short (about 100 nsec), dc-operation is possible even in the presense of high background rates, and other detectors within the experiment can decide whether or not the trajectory of a penetrating particle is to be read out.

Spark chambers, on the other hand, are triggered devices and in order to sensitize the spark chamber, a high voltage pulse has to be applied immediately after the passage of a particle whose trajectory has to be determined. This not only requires fast, high voltage trigger circuits with very high reliability (now under development), but it also creates a very severe electromagnetic interference (EMI) problem. EMI from the spark chambers requires special precautions to be taken to protect other electronic circuitry and to reduce errors due to EMI in the measurement of low-level analog signals. Spark chambers have to be either extremely carefully shielded or the measurement and analysis of low-level analog signals from detectors like scintillation-counters has to be completed before the spark chambers are triggered. This requires fast electronic circuitry. While shielding adds weight and complexity, fast electronics consumes considerable amounts of electrical power. Both might be prohibitive in a given experiment.

MWPC's only require stable and programmable high voltage power supplies, which are readily available, and they do not emit EMI which allows the use of low power, slow electronics for the other detectors in the same experiment which leads to lower power consumption. The complexity of the readout electronics is roughly the same for both types of detectors.

Another advantage of MWPC's is their expected longer lifetime. Spark chambers use small amounts of organic quenching agents like ethanol for stable operation. These additives, however, can be disassociated during spark breakdown and have to be replaced. The disassociation products also can be the source of serious contamination through the buildup of permanent deposits on spark chamber wires which leads to unstable operation. MWPC's can successfully be operated with gas mixtures of argon, xenon, and carbon dioxide, i.e., without organic quenchers. These gas mixtures are not very prone to decomposition and it is believed that even sealed, large area MWPC's can be constructed and operated over long periods of time

without significant deterioration. It should be pointed out, however, that decomposition and contamination of MWPC gases can present a serious problem if gas mixtures with complex organic components like methane, isobutane, or freon are used, especially if the chambers have to be operated in a high gas gain mode.

A further very important advantage of MWPC's is their better ability to discriminate against delta-rays. Delta-rays are energetic electrons which are created when charged particles traverse any kind of material. The number of delta-rays increases with Z^2 (Z is the charge of the penetrating particle) which means that especially high-Z cosmic ray nuclei can be accompanied by considerable numbers of them. The task of the spatial detectors is then to determine the position information of the high-Z particle out of the background of simultaneous delta-rays. Normally the difference in energy loss between a delta-ray and a high-Z particle is quite significant in the sensitive volume around a MWPC anode wire, and because of the proportionality between energy loss and MWPC output signal it is in principle possible to discriminate against delta-rays by electronic means and to measure the trajectory of a high-Z cosmic ray nuclei unambigiously. Delta-ray discrimination with spark chambers is inherently much more difficult because the spark mode of operation produces an output signal of a spark chamber that is not proportional to the energy loss in the spark chamber gap.

3. MWPC - PRINCIPLE OF OPERATION

Single wire proportional counters have been used for a long time and their operation is well understood. The gas multiplication process around the anode wires of a MWPC is the same as in a single wire cylindrical counter and will, therefore, not be discussed in any detail, unless it is necessary for the understanding of a MWPC as a spatial detector. Charpak[5] has written a very good review article about MWPC's and their application in high energy physics experiments, and we will frequently refer to this article.

The typical MWPC configuration that has been under investigation at TRW is shown in Figure 3-1. The anode and cathode wires were wound on round fiberglass frames and soldered to a pc-board, which was glued into the fiber-

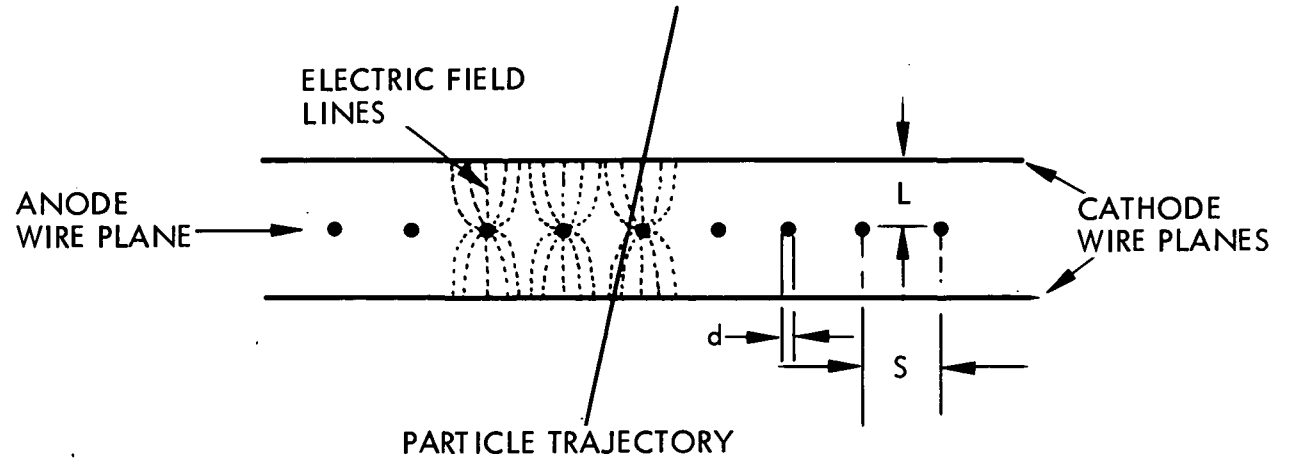

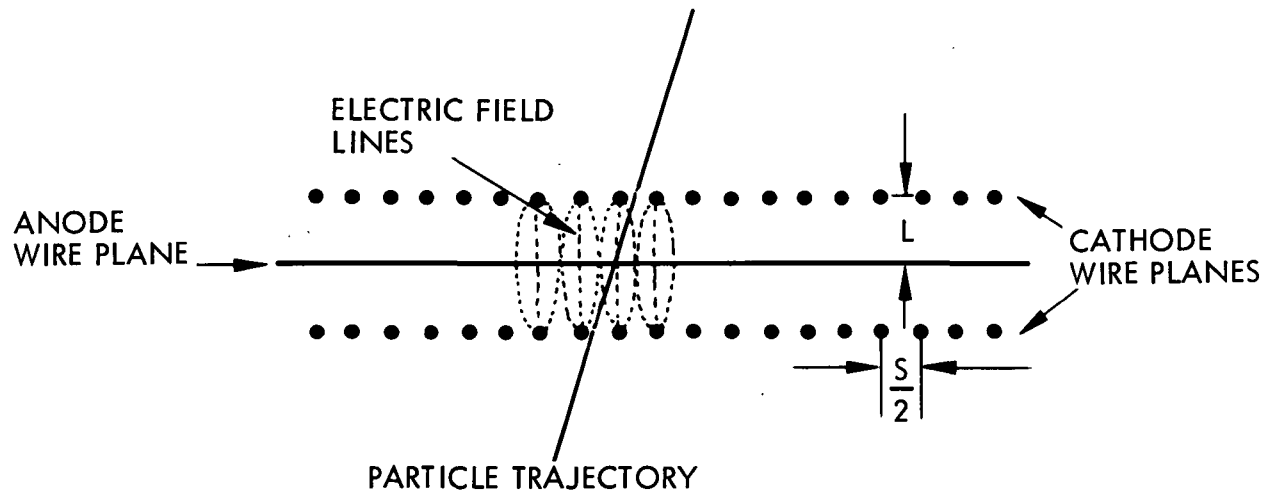

STANDARD LABORATORY CHAMBER:

ACTIVE AREA: 2" X 2"

L: 0.5 CM

S: 0.4 CM

d : 20 MICRONS

FIGURE 3-1 MWPC-Configuration

glass frames. The fiberglass rings were then clamped together with O-rings in between to seal off the chamber volume. Two additional fiberglass rings with thin Mylar films were used as gas windows. The chambers were operated in the gas flow-through mode. Typical chamber parameters are:

Anode - Cathode Gap: 5 mm
Anode wire spacing: 4 mm
Cathode wire spacing: 2 mm
Anode wires perpendicular to Cathode wires
Anode wires: 20μ diameter gold plated tungsten, the two end wires on each side of the anode plane wire 50μ diameter wires
Cathode wires: 50μ diameter gold plated tungsten

Also shown is the field configuration around the anode wires. Although the anode wires are not separated by cathodes it can be seem that the electric field forms a well defined sensitive cell around each anode wire. It is also indicated that the electric field close to the anode wire is nearly cylindrical.

When a charged particle enters the MWPC gap it produces a number of electron-ion pairs through ionization of the chamber gas. The electrons then start drifting towards the anode and the positive ions towards the cathodes. Because of the high field strength close to the anode wire the primary electrons are accelerated to sufficient energies to ionize further gas atoms and to initiate a cascade process which greatly multiplies the original number of ion-electron pairs and, therefore, leads to an observable signal. The cascade process occurs in very close proximity to the anode wire, i.e. in a cylinder around the wire with a radius of about one or two wire diameters. (See Ref. 5). Direct collection at the anode of the electrons is only responsible for a small fraction of the total proportional chamber signal, the largest part of the signal is due to the movement of the positive ions along electric field lines away from the anode. This can be explained as follows: The movement of electrons and positive ions induces currents (1) in the anode wire which collects the

electrons, (2) in neighboring anode wires in a MWPC, and (3) in both cathode planes. The induced current is

$$i = \frac{\Delta Q}{\Delta t} = \frac{\Delta Q}{\Delta r}\,\frac{\Delta r}{\Delta t} = \frac{Ne}{V_o}\,\frac{\Delta U}{\Delta r}\,w$$

Ne is the charge moving through a potential drop ΔU around the anode wire inducing the charge ΔQ which varies with time and causes the current i to flow. V_o is the applied voltage and w is the mobility of the charges.

In low-field regions the mobility of the positive ions w_+ is much lower than the mobility of the electrons w_-. However, in the high field region close to the collecting anode wire the mobilities are about equal: $w_+ \approx w_-$. The electrons of the multiplication region see only a small value of ΔU before being collected while the positive ions must move through the full potential drop across the chamber. The drift of the positive ions away from the anode is, therefore, responsible for most of the total MWPC signal. Since the electrons and initially also the positive ions move very fast one sees a fast rising current pulse with a slow decay. The slow decay represents the movement of the positive ion cloud in low field regions. Figure 3-2 shows some current pulses taken from one of our MWPC's. The pulses were produced by 5.9 KeV x-rays from a Fe-55 source. The chamber gas was 90% Ar + 10% CO_2 and operating voltage was 2100 volts.

Table III-1 shows the time development of the charge pulse in our chamber configuration, based on equations given by Charpak[5]. The important thing to notice here is the fact that it takes many μsec to collect the total charge and that only about 40% of the charge is collected during the first μsec, i.e. during the fast part of the pulse buildup.

In many MWPC applications it is not feasible to make use of the total charge. Typically, the output of a charge sensitive preamplifier is shaped by a post amplifier with RC shaping time constants of one or two microseconds in order to operate at reasonable pulse rates. This means that normally less than 10% - 50% of the charge is seen, depending on chambers configuration and operating parameters. This is also important with respect to the term "gas gain" of a proportional counter. Gas gain is the numerical factor which states by how many times the number of pri-

TABLE III-1

Time development of the MWPC charge pulse Q(t) in percent of the total charge (see also Ref. 5)

t	d = 20μ V_o = 2000V	d = 50μ V_o = 2500V	d = 100μ V_o = 3000V
1 nsec	3.0	.9	.4
.2 nsec	5.1	1.8	.7
10 nsec	12.4	6.2	3.0
100 nsec	26	19	13
0.5 μsec	36	30	25
1 μsec	40	35	30
10 μsec	54	51	48

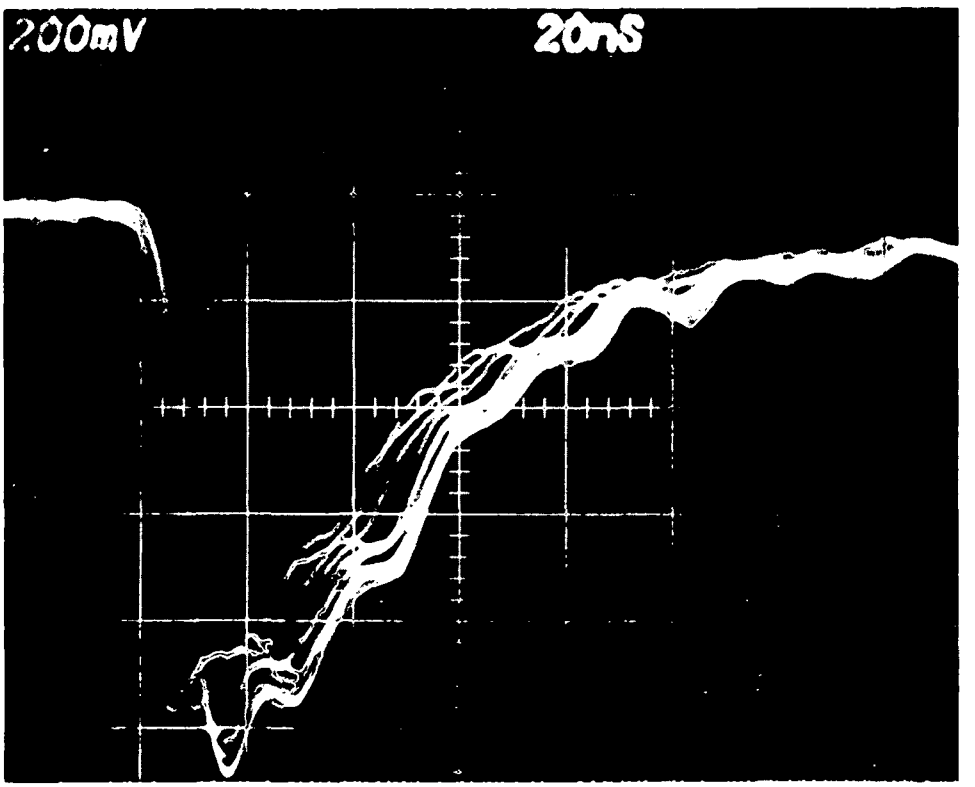

FIGURE 3-2. Photograph of Fe-55 current pulses in 90% Ar + 10% CO_2 at 2100 Volts

many electrons has been multiplied in the cascade process. Numbers which are quoted often do not represent the total gas gain, but rather a relative gas gain referring only to the fast part of the charge pulse because shaping amplifiers are used.

The movement of the positive ions away from the collecting anode wire induces a negative current pulse in that wire and positive current pulses in the neighboring anode wires and the two cathode planes (total induced charge = 0). The way the positive charge is divided between the cathode planes and the neighboring anodes depends on the geometrical configuration of the MWPC. In order to have most of the charge induced in the cathode planes it is important to make the ratio of anode wire spacing to anode-cathode gap as large as feasible.

The output pulse of a MWPC is over a large region strictly proportional to the initial ionization. However, if the charge density of the positive ions in the cascade region becomes comparable to the charge density on the anode wire, saturation occurs due to space charge effects and the strict proportionality ceases to exist. Because of the delta ray problem in high energy cosmic ray experiments it is desirable to operate MWPC's well within the proportional region and not at such a high gas gain that saturation occurs. In this respect it is important to note that the range of strict proportionality can be influenced to some extent by the choice of the MWPC gas[6].

The results of our MWPC investigation which are described in this report have all been obtained with "normal" gas mixtures as opposed to "magic" gas mixtures. MWPC's operated with normal gas show a region of strict proportionality before going into saturation and eventual breakdown. Saturation is due to space charge effects and breakdown is due to photon processes. With magic gas mixtures it is possible to prevent chamber breakdown and to obtain considerably higher gas gains than with normal gases, however, without maintaining proportionality.

R. Bouclier et al.[7] who first reported measurements with magic gas obtained the gas by adding small amounts of highly electronegative freon - 13B1 to their argon/isobutane mixtures. Extensive investigation of MWPC's operated with magic gas have been reported by J. Lacy.[8] According to

Bouclier et al. it is the formation of heavy negative ions due to the electronegative nature of freon - 13B1 that seems to neutralize the positive ions of the space charge, and thus makes it possible to achieve higher gas gains. Lacy believes and has indications that a basic change in the discharge process is responsible for the much higher gas gain. Indications are that only the first or first few electrons reaching the anode region are responsible for initiating the cascade process and that the high gas gain might be provided by a photon propogation mechanism which is controlled and confined by the photon absorbtion properties of the freon. Lacy has pointed out some attractive properties of MWPC's with coaxial delay-line readout operating at high gas gain with magic gas. At TRW we have concentrated on normal gases because extremely high gas gains are not necessary to achieve the desired spatial resolution, and because of some difficult problems that arise from magic gas operation. One severe problem arises from the loss of the ability to discriminate against delta-rays which is based on the proportionality of the chamber. Another potential problem is the fact that MWPC gases with organic constituents are subject to decomposition which can cause contamination of the MWPC and limit its lifetime.

It is well known that the performance of MWPC's deteriorates due to contamination [9, 10]. Two forms of contamination exist: Contamination of the MWPC gas and contamination of MWPC wires. The MWPC gas can become contaminated with outgassing products from the materials that are used in manufacturing of the chambers. This requires the use of low outgassing materials and careful cleaning techniques. In the BCR-5 experiment the materials had to be limited to non-magnetic materials (except for the anode and cathode wires). A way to overcome the gas contamination problem is to constantly flow fresh gas through the chambers (BCR-5 approach), or to dump the old gas and refill with new gas in periodic intervals.

Another and potentially more troublesome problem is the possible contamination of MWPC wires. It has been observed that solid and liquid deposits form on the wires after the accumulation of a large number of counts in gases containing organic constituents, especially hydrocarbons. The deposits apparently are polymerization and/or disintegration products of the organic constituents. The level of contamination is a function of

the total accumulated charge and thus depends on the number of counts and the gas gain. While the flux of high energy cosmic rays itself is not high enough even in two years to reach the critical number of counts, it has to be remembered that MWPC's are constantly sensitive so that the total number of counts is actually appreciable higher due to low energy background radiation. In this respect it is particularly important that the chambers can be turned off when the spacecraft passes through the South Atlantic Anomaly of the radiation belt with its high fluxes of low energy electrons and protons.

The contamination problem not only requires careful material selection for the construction of MWPC's for space applications but also makes it desirable to operate the chambers with gases not containing organic constituents.

3.1 Readout Concepts

Several techniques have been used to read out the spatial information contained in a MWPC-signal after the passage of, for instance, a high energy cosmic ray particle or the conversion of an x-ray. The readout method which is actually chosen depends on several parameters, the most important of which is usually the spatial resolution that is required.

Single wire readout systems and coding techniques are being used in large area MWPC systems if spatial resolution of a few millimeters is sufficient. This is often the case in large accelerator experiments and also in certain cosmic ray experiments like the ionization spectrometer experiment ACR-6 on HEAO-A. In a single wire readout system each wire is connected to its own amplifier and subsequent chain of post amplifiers, gates, discriminators and storage elements[11]. Readout electronics then determines the address of each wire that has responded. The uncertainty with which the position of a track can be determined in this way is equal to the anode wire spacing. In other words, a single wire readout system quantizes the position information and the quantum size corresponds to the anode wire spacing. An important advantage of this system is its capability to read out many simultaneous events. The disadvantage of such a system is the large number of electronic channels, with its impact on cost, power, weight, volume and reliability, especially if a large number of MWPC's has to be

used. For space applications a single wire readout system, therefore, becomes very easily prohibitive. For accelerator experiments the single wire readout system is still feasible[12], even if it involves thousands of channels, because of the much more relaxed requirements on weight, power, volume and reliability which allow the cost to be kept at a few dollars per channel[13].

The amount of electronics can be reduced if coding techniques can be used in which the signal coming off the anode wires are split and routed into several electronic channels which then can be decoded to give the address of the wire that has responded. The disadvantage of such coding systems is the reduced signal to noise ratio because of the large number of signal splits which could require operation of the MWPC at uncomfortably high gas gains. An additional disadvantage is the reduced capability to analyze several simultaneous events, and in large MWPC systems the amount of electronics will still be large. Single anode-wire readout systems become totally impractical if spatial resolution on the order of a fraction of a millimeter is required due to limitations in anode wire spacing.

This problem can be overcome by making use of the induced charge on the cathode planes of a MWPC. The induced charge distribution peaks exactly above that point of the anode wire that collects the electron cascade, which makes it possible to retrieve position information perpendicular to the anode wire direction with considerable accuracy. Delay-line read-out systems have been developed which can interpolate the peak of the induced charge distribution to within .1 mm to .2 mm, i.e. considerably more accurately than the anode wire spacing.

In the literature and also in this report we frequently use the term "spatial resolution" when we actually mean the accuracy of position determination. Spatial resolution more accurately should describe the ability to resolve two closely spaced particle tracks or x-ray events. Spatial resolution defined in this way would, of course, depend on the accuracy of position determination, which is characterized by the width of the measured position distribution.

In a delay-line readout system the delay-line is coupled to either one or both of the cathode planes with the cathode wires running perpendicular to the anode wires. The position of the peak of the induced charge distribution is determined by measuring the difference in arrival time of the delay-line signal at both ends of the line. Figure 3-3 shows the basic block diagram of a MWPC with delay line readout.

It is obvious that such a system significantly reduces the amount of electronics necessary and that it can therefore reduce the complexity of a MWPC - system even when very good spatial resolution is not required. At TRW we have therefore, also designed and tested MWPC's with delay-line readout of the anode wires. The disadvantage of a delay-line readout system that replaces a single wire readout system is it's reduced capability of handling a large number of simultaneous events. However, in many applications the handling of two or three simultaneous events is the most that is required, and this can be achieved with delay-line systems with some added complexity in the electronics.

The spatial resolution is determined by the accuracy with which the peak of the induced charge distribution represents the position of the ionizing event in the MWPC gap, and by the timing accuracy of the delay-line readout system. The electronic resolution or the jitter in timing Δt of the two delay-line signals is basically proportional to the risetime of the delay line pulse and to the signal to noise ratio of the output of the delay-line amplifiers:

$$\Delta t \sim \Delta R \frac{A_n}{A_s} \quad \text{(RMS)}$$

As will be pointed out in the delay-line analysis in Section 6, the risetime is determined by the bandwidth of the line and/or the risetime of the MWPC current pulses. The signal level A_s is a function of the chamber's gas gain and of the delay-line impedance. The impedance can also contribute significantly to the noise level A_n with the other major contribution coming from the delay-line amplifier.

Grove et al.[14] developed a distributed delay-line consisting of a solenoidal winding on a rectangular fiberglass core which forms the inductance. The distributed capacitance is formed by copper strips running along the core. To compensate for the inherent dispersion of the line the floating

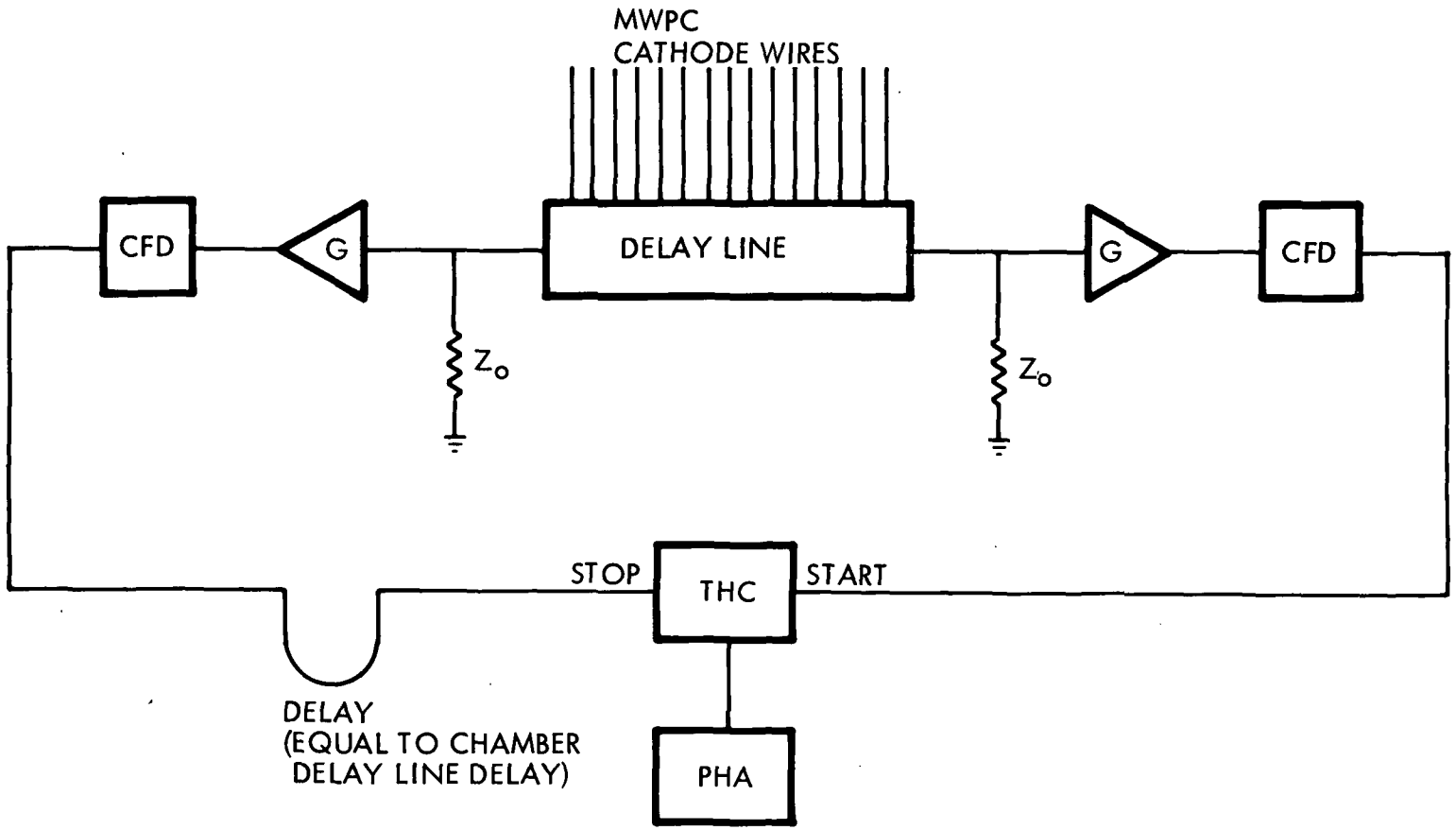

FIGURE 3-3 Block diagram of a delay-line readout system. G = Delay-Line Amplifier, CFD = Constant Fraction Discriminator, THC = Time to Pulse Height Converter, PHA = Pulse-Height Analyzer, Z_o = Delay-Line Impedance

patch technique was used. Strips of Mylar with thin metallic strips on it was glued to the line. The delay-line was capacitively coupled to one of the cathode planes of the MWPC by clamping it to a flat PC-board with copper lands to which the cathode wires were connected. At TRW we have built and used a number of similar delay-lines.

While excellent resolution (0.1 mm with collimated Fe-55 sources) and good linearity can be achieved with this delay-line, if it is carefully constructed, it has a number of disadvantages which make it less desirable for large area MWPC systems in space applications. Considerable parastic capacitances in large MWPC's limit the coupling efficiency between chamber and delay-line to only 5% - 10%, which requires operation of the chamber of a much higher gain than would be necessary for a delay-line with the same impedance but larger coupling efficiency. There are also significant end effects of the line which are difficult to compensate and to control, and the adequate packaging of the line would result in a relatively heavy mechanical structure. Since the original work of Rindi et al.[15] and Grove et al.[14] various other methods of implementing delay-line readout systems have been developed.

A basically very simple way to implement a delay line with excellent coupling efficiency, linearity and no end effects is to connect adjacent cathode wires with pieces of coaxial cable. The use of coaxial delay-lines has been reported by D. P. Boyd et al.[16] of Stanford and by J. Lacy[8] of Houston. The main advantage of coaxial delay-lines is their large bandwidth when used in connection with MWPC's operating with magic gas which results in considerably faster current pulses than those obtainable with normal gas for penetrating particles. Because of the large bandwidth of coaxial delay-lines the chamber risetime can be maintained and excellent spatial resolution can be achieved even with the reduced impedance of the line (50Ω to 100Ω as compared to close to 1 KΩ for the line of Grove et al.)

There are again, however, severe disadvantages for space applications. Because of the fast risetime (which allows smaller delays between wires than with the distributed line) fast timing electronics has to be used, which can lead to prohibitively large power consumption especially when a large

number of MWPC's has to be used. Another problem is the packaging of coaxial delay-lines, which become bulky and heavy in large systems. In order to improve the packaging, printed circuit delay-lines have been developed (D. P. Boyd et al[16].) with characteristics similar to coaxial cable.

A third method of implementing a delay-line readout system, which was first mentioned by Charpak et al.[17], has been investigated by Lee et al.[18] and Gilland and Emming.[19] In this case the chamber electrodes themselves form the delay-line (integral delay-line). In Lee's chamber the cathode consists of a bifilar helical winding of which one winding is grounded at every turn. The distance between windings was 0.5 mm and the cathode wire diameter was 50μ. This resulted in such a high attenuation of the line that it was necessary to connect electrical tabs every 3.65 cm and to measure signals at these points. The obvious disadvantage for space applications of the otherwise simple approach is the considerable complexity and large amount of readout electronics due to the many taps along the line for large area chambers.

A somewhat different approach was taken by Gilland and Emming who introduced sense planes located symmetrically between the anode and cathode planes of a MWPC and which were wound as a continuous coil. The coil inductance and its distributed capacitance to the anode and cathode planes determine the delay line characteristics. Again, while the basic approach is elegant there are potential disadvantages of the readout system in space applications, especially for cosmic ray experiments. The major problem as we see it is the fact that the delay-line parameters and the achievable resolution are strong functions of the geometrical configuration of the chamber. This allows little flexibility in chamber design and can lead to difficult mechanical problems in chamber construction. This is especially true if the gap width of the chamber has to be kept small because of potential problems due to delta-rays and inclined particles in cosmic ray experiments.

At TRW we have developed a fourth approach to implement a delay-line readout system that overcomes most of the difficulties of the other systems. Our delay-line which is called the "lumped element delay-line" consists of

individual L's and C's, which are directly coupled to both cathode planes and which determine the delay-line characteristics. A complete analysis of the delay-line is given in Section 6.

In this analysis we first calculate the impulse response of a lumped element delay-line for a 50 cm chamber with the geometrical configuration of our standard chamber (Figure 3-1) operated with Ar/CO_2 gas, using the known design equations for the delay-line (e.g. equations for the risetime and delay per section, for the risetime and delay for n sections, and for the characteristics impedance). Knowledge of the impulse response is necessary to calculate the delay-line output which is the weighted sum of the individual, induced cathode current pulses. The current pulses have been modeled according to the shape of observed current pulses for 5.9 KeV x-rays from Fe-55 sources. When the delay line output pulse is known it is possible to calculate the spatial resolution (electronic resolution only) of the readout system in Figure 3-2, taking into account the risetime and impedance of the delay-line, the amplitude of the delay-line signal, the noise of the preamplifiers, and the timing jitter of the CFD's. The analysis shows that an optimum interwire delay or delay per delay-line section exists for optimum spatial resolution of the particular MWPC under consideration. It is also shown considering the electronic system only, that a spatial resolution of at least 100μ for Fe-55 x-rays can be achieved at gas gains for which the chamber is in the proportional region.

The advantages of the lumped element delay-line can be summarized as follows:

1. The delay-line characteristics are independent of the MWPC design (MWPC parasitic capacitances are taken into account in the delay-line optimization analysis). This allows flexibility in chamber design and independent optimization of chamber and delay-line.
2. Direct coupling of both cathodes into the delay line assures maximum coupling efficiency.
3. Compact construction is possible, providing minimum weight and volume.
4. Uniformity of the line makes it amenable to optimization studies.

3.2 Summary of Parameters Which Influence Spatial Resolution.

It is possible to achieve good spatial resolution with large area MWPC's by using delay-line readout systems which measure the position of the peak of the induced charge distribution on the cathode planes of a MWPC. The accuracy with which the position can be determined depends on a number of parameters which determine how accurately the peak represents the position of the ionizing event and parameters which determine how accurately the electronic readout system can determine the position of the peak. These parameters are:

1. Parameters associated with the gas multiplication process
   a. Diffusion of electrons and positive ions
   b. Spread of the discharge along the anode wire
2. Parameters associated with the penetrating particle
   a. Inclination of the particle's track
   b. Delta rays
3. The signal to noise ratio which, in a given system, depends on the gas gain.

A detailed discussion of these parameters follows in Section 5 through 8 of this report in conjunction with theoretical investigations and experimental results. The effect of electronic noise will be discussed in Section 6.

In principle it is desirable to minimize electronic noise to the point where it is not the determining factor that limits the achievable spatial resolution, and our analysis will show that this is possible without having to operate the MWPC at such high gas gains (large signal to noise ratio) that one leaves the strictly proportional region.

Attempts have been made to calculate the effect of electron diffusion and spread of the discharge along the anode wire on spatial resolution. Indications are that both effects do not prevent a resolution of better than 100μ. Our measurements show, however, that some limiting effect does exist which results in a plateau in the measured resolution instead of a continuous improvement with improving signal to noise ratio. The conclusion that has to be drawn from this apparent discrepancy is that it is

difficult to accurately calculate the effects of electron diffusion and discharge spreading because of some simplifying assumptions that have to be made and because some of the gas dependent parameters entering the calculations are not very well known.

To estimate the effect of delta rays on spatial resolution we have carried out Monte Carlo calculations to simulate the effect of delta rays. The results of the computer calculations show that low energy delta rays broaden the main core of ionization which can definitely limit the achievable spatial resolution for high-Z nuclei (Z>4) to greater than the desired value of 100μ to 200μ. For $Z \leq 4$ the delta ray effect is in the order of other limiting effects, and particularly for minimum ionizing, singly-charged particles (electrons and protons)delta rays are not important.

In cosmic ray experiments particles enter the spatial detectors on the average under some angle of inclination. The performance of MWPC's with collimated radioactive sources and normally incident particles is, therefore, not necessarily representative for the performance under the conditions of the actual experiment. We have measured the dependence of the spatial resolution on the angle of incidence and the result is that the resolution deteriorates with increasing angle of incidence.

For measurements with collimated radioactive sources the collimation needs to be good enough so that the source width does not limit the achievable resolution. While good collimation of an Fe-55 source is no problem, it is more difficult to adequately collimate electron sources because of multiple scattering of the electrons. An arrangement to limit multiple scattering will be described in Section 7.

4. GAS GAIN OF MWPC's

In order to optimize MWPC configurations it is desirable to be able to calculate the expected gas gain as a function of the MWPC geometrical configuration, operating parameters and chamber gas. Several methods are available from the literature to calculate the gas gain of single wire cylindrical proportional counters.[20] We will show, however, that the method usually used fails to predict the gas gain of MWPC's of different con-

figurations (e.g. different anode wire diameters).

We will then describe a straight forward calculation which is based on the knowledge of the first Townsend coefficient. The problem with this method is that the Townsend coefficient is not known for most gas mixtures used in MWPC's. We have, therefore, measured the Townsend coefficient for 80% Ar + 20% CO_2, and we show that the calculations using the Townsend coefficient are self consistent and predict the gas gain for different geometrical configurations with fairly good accuracy. This points out the need for accurate measurements of the Townsend coefficient for the various MWPC gases over the E/p ranges encountered in MWPC's.

4.1 Calculations Based on a Formula Given by Rose and Korff[20]

The calculation of the gain of a cylindrical proportional counter is usually based on a formula derived by Rose and Korff as given by Curran and Craggs:

$$\ln G = 2(2C V_o a r_1)^{1/2} \{(V_o/V_s)^{1/2} - 1\} \qquad (4\text{-}1)$$

G = gas gain
C = capacitance per unit length of anode wire
a = constant
r_1 = anode wire radius
V_o = applied voltage
V_s = threshold voltage, onset of gas amplification

This formula can be applied without changes to a MWPC since the field around the anode wire is cylindrical and the gas multiplication process takes place in that region.

Figure 4-1 shows the geometrical parameters of a MWPC:

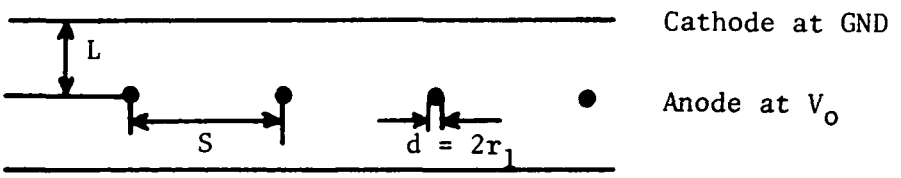

FIGURE 4-1

We define

$$X = \ln \frac{\sin h\ (\frac{\pi L}{s})}{\sin h\ (\frac{\pi r_1}{s})}$$

or approximately

$$X \cong \frac{\pi L}{s} - \ln \frac{2\pi r_1}{s} \tag{4-2}$$

The electric field around the anode wire is

$$E\ (r) = \frac{V_o}{Xr} \tag{4-3}$$

The charge per unit length of anode wire is

$$q = \frac{V_o}{2X} \tag{4-4}$$

and the capacitance per unit length is

$$C = \frac{q}{V_o} = \frac{1}{2X} \tag{4-5}$$

With that we can write

$$\ln G = 2(V_o a r_1/X)^{1/2}\{(V_o/V_s)^{1/2} - 1\} \tag{4-6}$$

which gives the gas gain as a function of the geometrical configuration and operating voltage of the MWPC. Equation (4-6) contains the constant "a" and the parameter V_s which have to be determined.

The constant "a" is gas dependent and is defined through

$$\sigma_i = \frac{1}{n\lambda_i} = a(V-V_i)$$

σ_i is the ionization cross section, λ_i is the mean free path between ionizing collision, n is the number of atoms per cm^3, V_i is the ionization potential, and V is defined by the energy eV of the ionizing electron. The value of "a" thus expresses the rate of increase of the ionization cross section with energy. This has been measured for a number of gases but unfortunately not for the gas mixtures usually used in MWPC's.

At the threshold voltage V_s the electric field at the anode wire is such that the ionization potential can be reached by the electron in a mean free path λ_i:

$$E = \frac{V_i}{\lambda_i} = \frac{V_s}{Xr_1}$$

and

$$V_s = \frac{Xr_1 V_i}{\lambda_i}$$

V_s is not only gas dependent but depends also on the geometry of the chamber.

Because of insufficient knowledge and lack of measurements of gas parameters for proportional counter gases both "a" and V_s cannot be determined accurately. V_s also cannot be measured by pulse techniques because the signal level at the threshold voltage is too low to be recovered out of the noise.

Good agreement between the predictions of equation (4-6) and experimental measurements has been achieved with suitable adjustment of the two parameters "a" and V_s for one set of conditions, i.e., for a particular gas and a given geometrical configuration. If the geometrical configuration is changed, e.g. by changing the anode wire diameter, equation (4-6) however, does not predict the gas gain dependence with any reasonable accuracy. To show this we used three MWPC's which were identical except for the anode wire diameter which were 100μ, 50μ, and 20μ and we measured the gas gain as a function of V_o for all three chambers in 80% Ar + 20% CO_2. Figure 4-2 shows the measured gas gain curves. If we fit equation (4-6) to the 20μ data and predict the 100μ data we get the results plotted in Figure 4-2. As one can see, there is poor agreement between the calculated and measured curves. The discrepancy has to be due partly to the inaccurate knowledge of "a" and V_s and partly to the simplifying assumptions in the derivation of equation (4-6). It was assumed that the electron energy after each collision is always equal to eV_i and fluctuations in energy loss have been neglected.

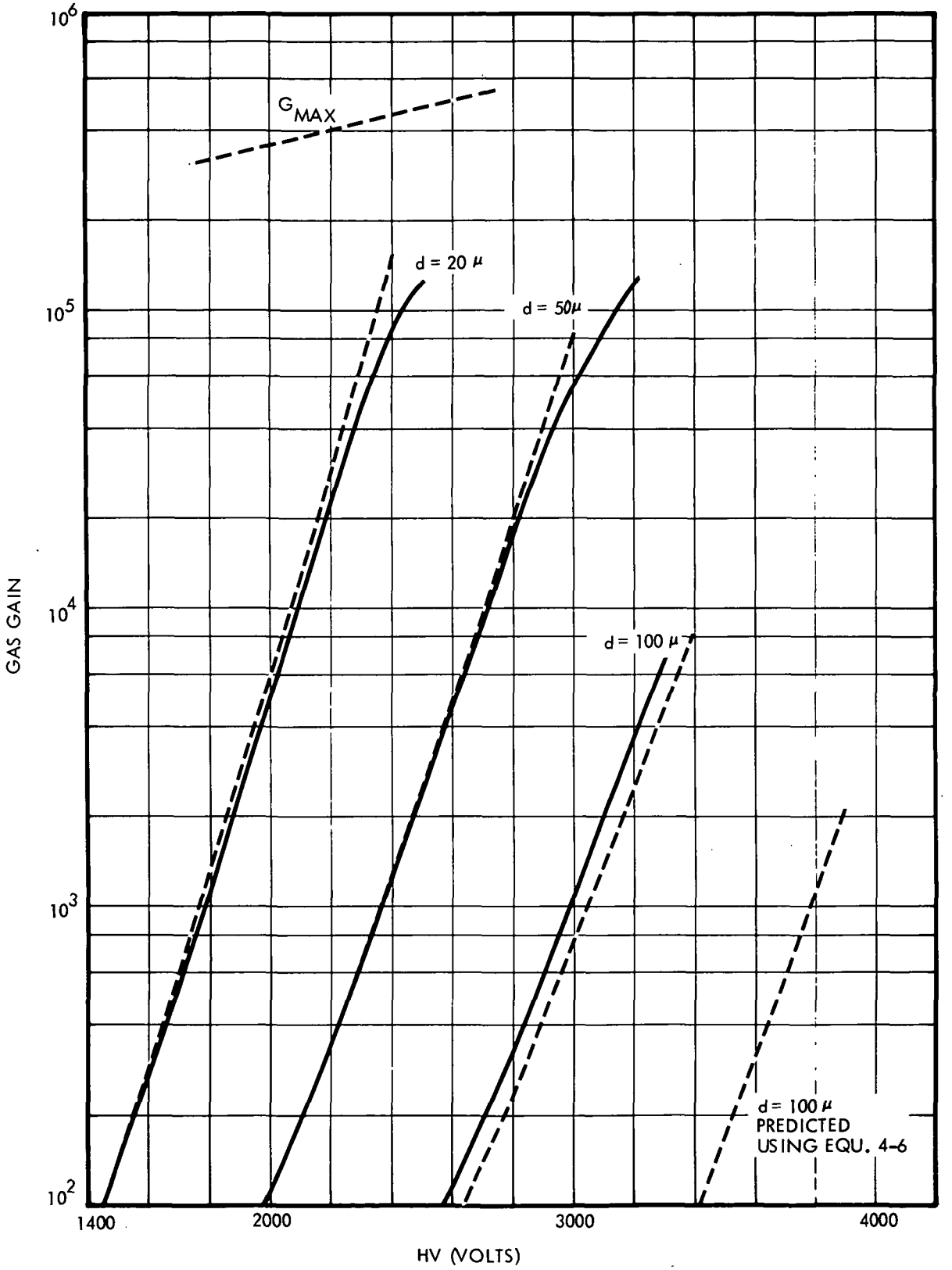

FIGURE 4-2. Gas gain for 5.9 KeV x-rays in 80% Ar + 20% CO_2 in chambers with different anode-wire diameter

We have attempted another approach to calculate the gas gain which parallels the one of Rose and Korff, but which uses a different set of simplifying assumptions. It leads again to an equation with two adjustable parameters which allow a good fit to one set of measurements, but which also do not predict another set of measurements taken with a different geometry.

4.2 Calculation Based on Townsend Coefficient

A straight forward way of calculating the gas gain of a proportional counter is possible by using the first Townsend coefficient, α, which characterizes the gas multiplication process. The Townsend coefficient is a function of the electric field E and depends on the gas mixture.

When α is known the gas gain can be directly calculated from the formula

$$G = \exp\left\{\int_{r_1}^{r2} \alpha(E)\, dr\right\} \tag{4-7}$$

or

$$\ln G = \int_{r_1}^{r_2} \alpha(E)\, dr \tag{4-8}$$

r_1 is the anode wire radius and r_2 would be the cathode radius in case of a cylindrical counter. In a MWPC r_2 has to be large enough so that the multiplication process occurs inside a cylinder with radius r_2 around the anode wire. The Townsend coefficient has been measured as a function of E/p (p = gas pressure) for a number of pure gases and some gas mixtures, but again not for most of the gas mixtures used in MWPC's.

The value of α can be derived from measured gain-voltage curves by differentiating equation (4-8):

$$\ln G = \int_{r_1}^{r_2} \alpha(E)\, dr$$

$$E = E(r) = \frac{V_o}{Xr}$$

$$\ln G = \int_{\frac{V_o}{Xr_2}}^{\frac{V_o}{Xr_1}} \alpha(E)\, \frac{V_o}{X}\, \frac{dE}{E^2} \tag{4-9}$$

After differentiation:

$$d\ln G / dV_o = \frac{\ln G}{V_o} + \alpha\left(\frac{V_o}{X r_1}\right) \cdot \frac{r_1}{V_o} - \alpha\left(\frac{V_o}{X r_2}\right) \cdot \frac{r_2}{V_o}$$

As we will show below, because of the rapid decrease of α with E at low values of E the term $\alpha(r_2)\,\frac{r2}{V_o}$ is less than 1% of the term $\alpha(r_1)\,\frac{r_1}{V_o}$ and can be neglected.

The field at the anode wire is

$$E = \frac{V_o}{X r_1}$$

and close to the cathodes it is

$$E = \frac{V_o \pi}{X s}$$

For our three chambers with r_1 = 10μ, 25μ, and 50μ we had s = .4 cm, $6.48 \leq X \leq 8.09$, and $1500 \leq V_o \leq 3000$. Near the anodes we get

$$E/p > 105 \text{ V cm}^{-1} \text{ Torr}^{-1}$$

$$\alpha/p > 1$$

$$\alpha/p \cdot r_1 > 50 \times 10^{-4}$$

Near the cathodes we get

$$E/p \leq 4.8 \text{ V cm}^{-1} \text{ Torr}^{-1}$$

$$\alpha/p < 10^{-4}$$

$$\alpha/p \cdot L < 0.5 \times 10^{-4}$$

which is less than 1% of the anode value.

We can now express the Townsend coefficient as a function of the electric field at the anode wire as

$$\alpha\,(V_o/X r_1) = \frac{d\ln G}{dV_o} - \frac{\ln G}{V_o} \qquad (4\text{-}10)$$

Before we calculate α/p as a function of E/p from our gas gain measurements with 20μ, 50μ and 100μ anode wires, we have to remember that the measured values do not represent the total gas gain but the relative gas gain as pointed out in Section 3. Therefore, before we calculated α/p we calculated the absolute gas gain from the measured relative gas gain. The fraction of the total charge which is represented by the relative gain was given in Table III-1, which shows the time development of the MWPC pulse for the three different chambers. Figure 4-3 shows α/p as a function of E/p as derived from our adjusted gas gain measurements.

To calculate the gas gain for 20μ, 50μ and 100μ diameter anode wire we used a linear approximation of α/p, which is the solid curve in Figure 4-3. With that it is easy to integrate equation (4-8):

$$\ln G = \int_{r_1}^{r_o} \alpha(r)dr$$

Approximation for α:

$$\alpha = D(E-E_o) \quad \text{for } E > E_o$$

$$\alpha = 0 \qquad \text{for } E \leq E_o$$

Close to the anode we have

$$E = V_o/Xr \text{ or, } r = V_o/XE$$

and $r_o = V_o/XE_o$ which is the radius at which $\alpha = 0$.

With that is follows:

$$\ln G = \int_{r_1}^{r_o} D(E(r) - E_o)dr$$

$$= D \int_{r_1}^{V_o/XE_o} (V_o/Xr - E_o)\, dr$$

$$= D \{V_o/X \ln r - E_o r\}_{r_1}^{V_o/XE.}$$

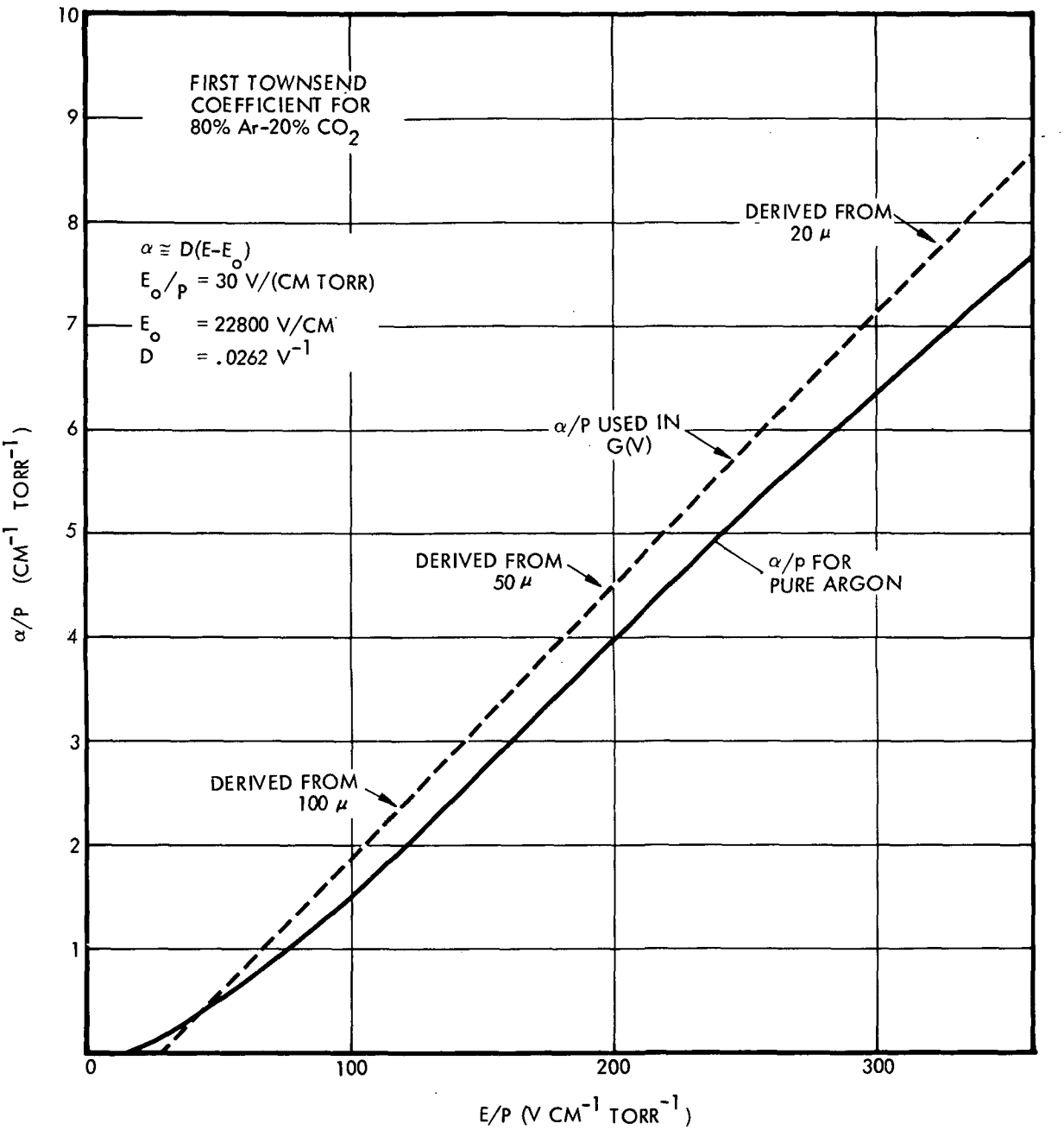

FIGURE 4-3. Townsend Coefficient α/p v.s. E/p

$$= D \{V_o/X \ln \frac{V_o}{XE_o r_1} - E_o \left(\frac{V_o}{XE_o} - r_1 \right)\}$$

$$\ln G = Dq \frac{V_o}{X} \{\ln \frac{V_o}{XE_o r_1} + \frac{XE_o r_1}{qV_o} - 1\} \qquad (4\text{-}11)$$

which allows one to calculate the gas gain as a function of the geometrical configuration and operating voltage.

The calculated gas gain curves using equation (4-11) for 20μ, 50μ and 100μ anode wires are also plotted in Figure 4-2 using $E_o/p = 30$ V cm^{-1} Torr^{-1}, E_o (STP) = 22,800 V and D = .0262 V^{-1}. The plotted values are the relative gas gains which were obtained after adjusting the absolute gain of equation (4-11) according to the percentage numbers given in Table III-1.

The agreement between measured and calculated curves is quite good for 20μ and 50μ. The discrepancy for 100μ could indicate that the chosen approximation for α/p does not hold for low E/p values which is expected. However, the internal consistency of this method has been demonstrated and it would, therefore, be desirable to have accurate measurements of α/p available for the commonly used MWPC gases over the E/p range normally encountered in MWPC's.

4.3 Gas Gain Measurements for Different Gases

We have measured relative gas gain curves for four different gases in our standard MWPC which was operated in a flow-through mode. The measurements were made using a radioactive Fe-55 source. The anode wires in the center of the chamber were interconnected and then connected to an Ortec 109 PC charge sensitive preamplifier (see Figure 9-2 which shows the setup of our MWPC's for measurements in a heavy ion beam at the Bevatron). The amplifier output signal was routed through an Ortec 410 main amplifier into a pulse height analyser. The double differentiation, single integration time constants of the 410-amplifiers were set at 1 μsec (this applies to all our measurements in this report).

Four different gases have been used:

1. 90% Ar + 10% CO_2
2. 80% Ar + 20% CO_2
3. 75% Ar + 25% Isobutane
4. 81% Ar + 14% Xe + 5% CO_2

The measured gas gain curves are shown in Figure 4-4, in which we have plotted the number of electrons at the amplifier input v.s. the operating voltage of the chamber. The number of electrons represents the fraction of the total charge which is accumulated in 1 μsec. To calculate the relative gas gain one has to divide the number of electrons by the number of primary electrons in the chamber gap. This was done in Table IV-1 for the measurements in 80% Ar + 20% CO_2.

For comparison purposes we have also included some of the measurements of Charpak et al.[21] in Figure 4-5. Our measurements are consistent with the conclusions that can be drawn from Charpak's more extensive results:

1. The operating voltage necessary to achieve a certain gas gain increases with increasing percentage of quenching agent in the chamber gas.
2. The onset of deviation from strict (i.e. linear) proportionality shifts to lower gas gains with increasing percentage of quenching agent.

From an operational standpoint it might seem, therefore, desirable to use a chamber gas with a minimum amount of quenching agent. According to results of Charpak et al.[21], which are shown in Figure 4-6, one has to be careful, however, in reducing the amount of quenching agent because at low percentages of quenching agent the voltages at the limit of the strictly proportional region and at the limit of chamber breakdown merge together.

Our measurement with 81% Ar + 14% Xe + 5% CO_2 also confirms the results of R.Z. Fuzesy et al.[6] that mixtures with Ar/Xe/CO_2 produce larger regions of strict proportionality than Ar/CO_2 or Ar/Isobutane mixtures. A result of practical importance is also the fact that Ar/Xe/CO_2 mixtures achieve high gas gains at considerably lower voltages than the other mixtures.

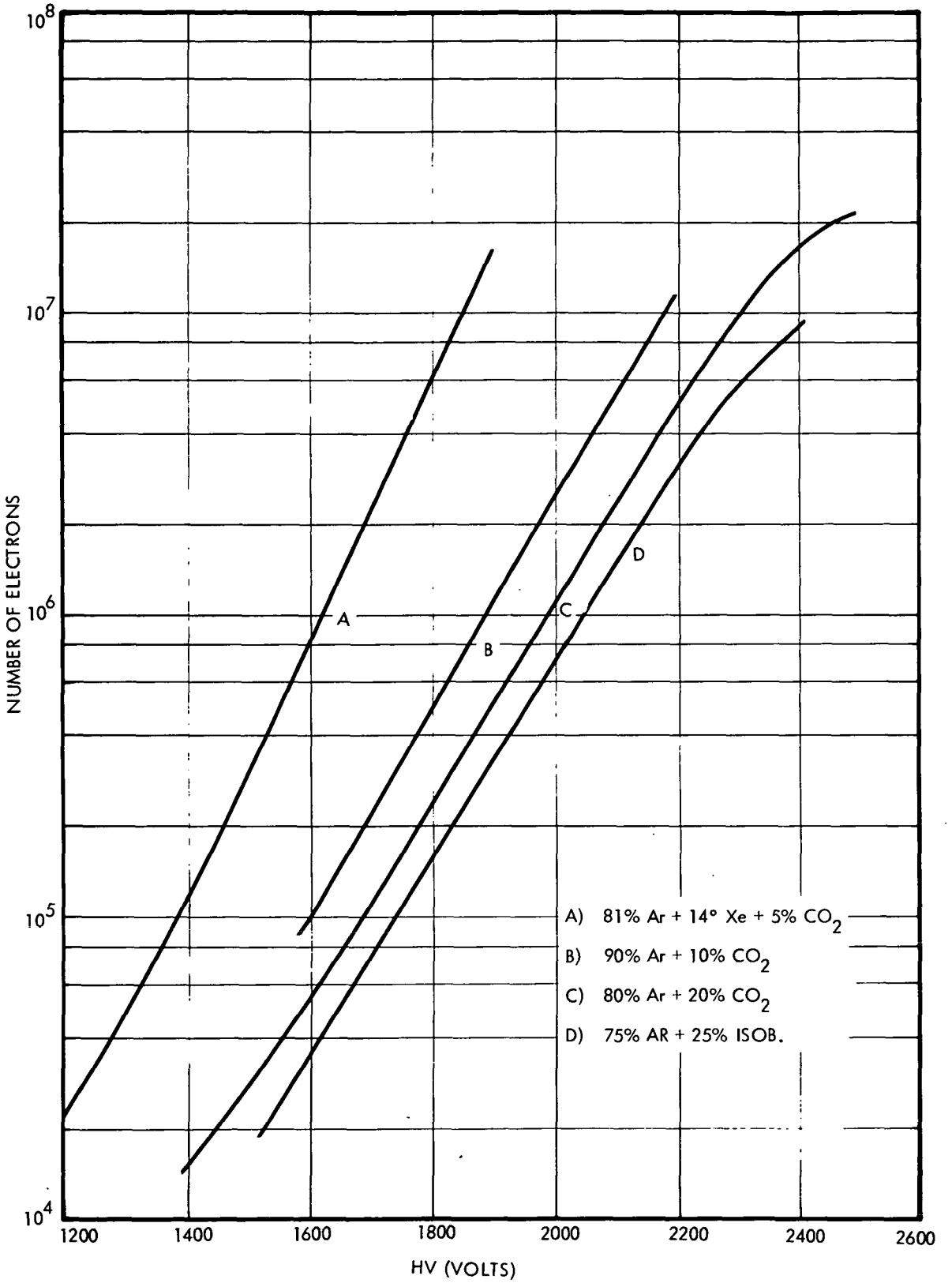

FIGURE 4-4. Gas gain for 5.9 KeV x-rays in different gases

TABLE IV-1

GAS GAIN IN 80% Ar + 20% CO_2

- Energy per ion pair: 27.2 eV
- Fe-55 main peak: 5.9 KeV
- No. of ion pairs in 1cm 80% Ar + 20% CO_2: 217

HV	No. of Electrons	Gas Gain
1400	1.52×10^4	7×10^1
1500	2.82×10^4	1.3×10^2
1600	5.4×10^4	2.49×10^2
1700	1.08×10^5	4.98×10^2
1800	2.33×10^5	1.07×10^3
1900	5.02×10^5	2.31×10^3
2000	1.08×10^6	4.98×10^3
2100	2.28×10^6	1.05×10^4
2200	4.93×10^6	2.27×10^4
2300	9.42×10^6	4.34×10^4
2400	1.64×10^7	7.56×10^4
2500	2.21×10^7	1.02×10^5

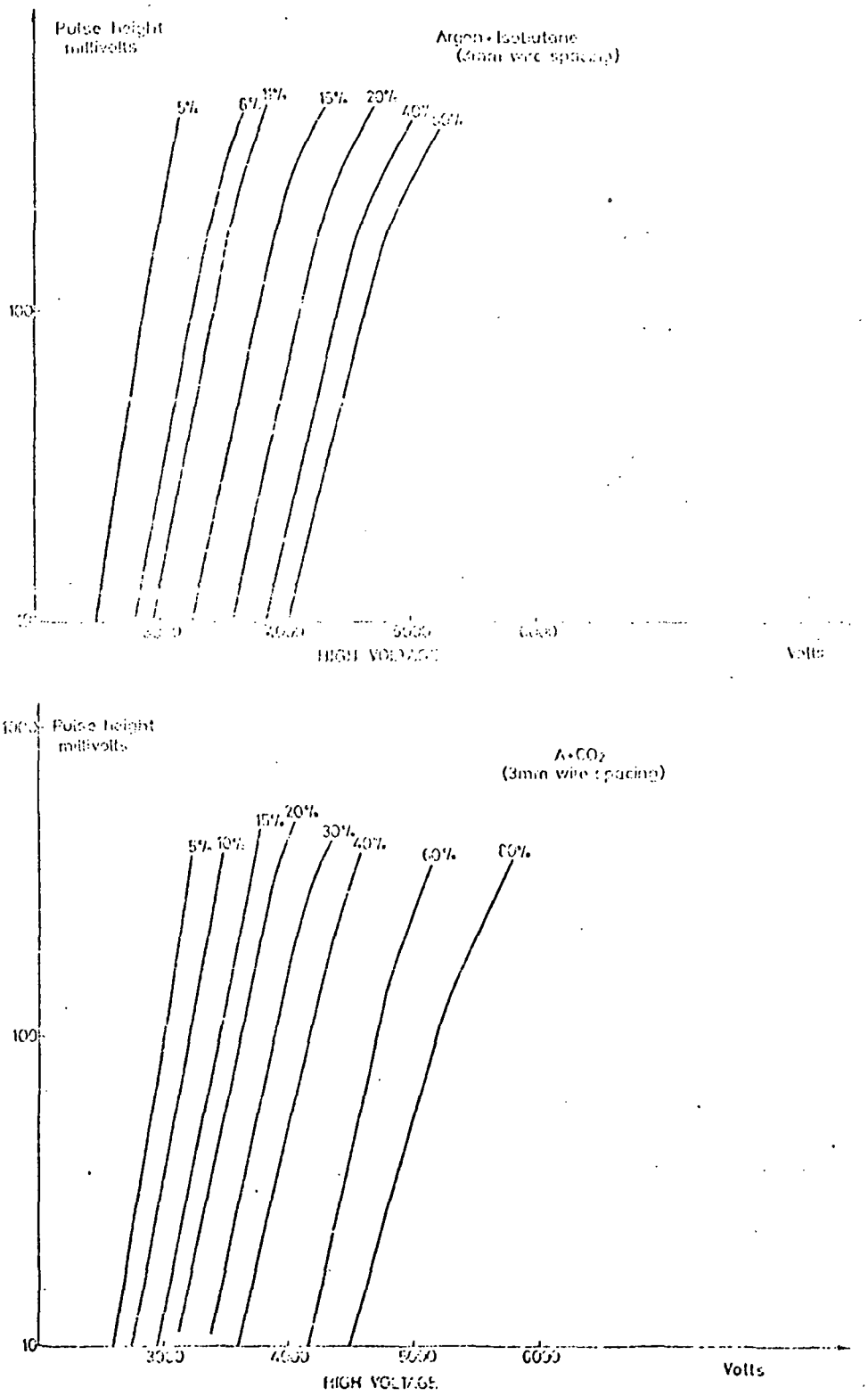

FIGURE 4-5. Gas gain curves from Charpak's measurements (Ref. 21)

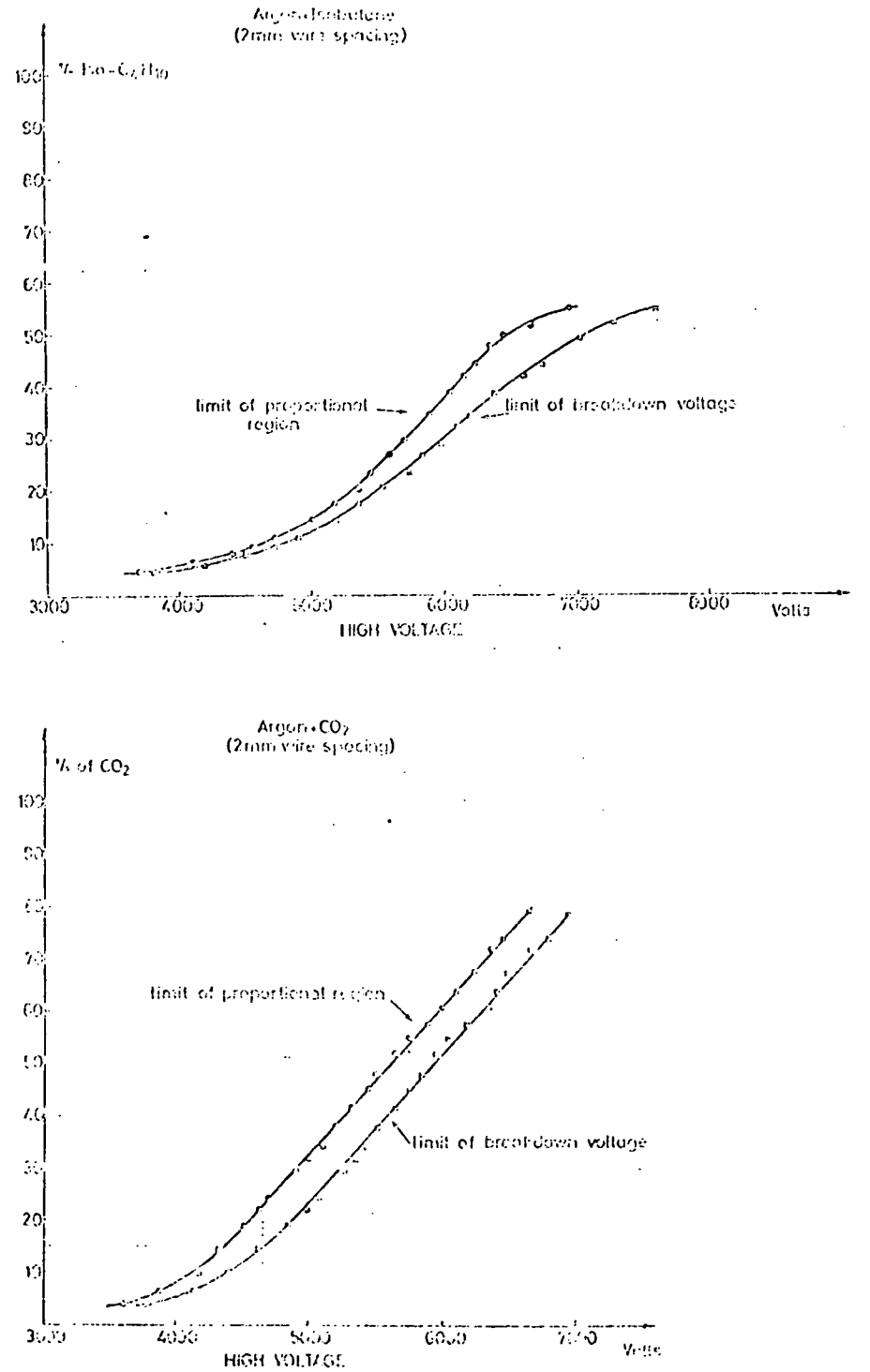

FIGURE 4-6. Limit of proportionality v.s. limit of breakdown from Charpak's measurements (Ref. 21)

4.4 Space Charge Effects

It has been pointed out before that the cloud of electrons and ions produced in the multiplication region near the anode constitutes a space charge that modifies the electric field configuration. This leads to a reduction in gain from the value that would be expected as a result of a calculation, such as we previously carried out, which neglects the presence of the space charge. The actual phenomenon is a complex time and space dependent process that would be very difficult to analyze. We have performed some calculations on the space charge effect with very simplistic assumptions. The most important of these are to completely neglect any time dependence, to use cylindrical geometry, and to use the simple linear expression for the first Townsend coefficient that was previously developed. As we shall see, the value of these calculations is to enable us to infer some limits on the effective width of the charge distribution along the anode wire. Because the space charge effects depend on charge per unit length along the anode they are inversely proportional to the length over which a particular amount of charge is spread.

Unless otherwise specified, we will be dealing with the following case:

Chamber configuration:	$d = 2 \times 10^{-3}$ cm
	$L = 0.5$ cm
	$s = 0.4$ cm
Gas:	80% Argon - 20% CO_2
Source:	5.9 KeV Fe^{55} x-ray
	(i.e. $\simeq$ 220 electron-ion pairs primary ionization)

We shall first calculate the reduction in gain near the onset of space charge effects. For our operating conditions this occurs at about 2300 volts (See Figure 4-4). In the case where the effects of space charge are small, we calculate the charge distribution without taking account of space charge, and then estimate the effect on the gain of this distribution. If the calculated effect is small, the method is consistent;

if not, we shall have overestimated the reduction due to space charge. In the next section we will estimate the upper limit on the charge that can be delivered under the extreme condition of space charge saturation.

At a radius, r, the number of electrons inside r is equal to the initial number electrons times the gain due to multiplication up to that radius, i.e.,

$$n_{-}(r) = n_o \exp\{\int_{r_o}^{r} \alpha dr'\}$$

There is obviously also an equal number of ions outside of r. If the charge distribution has an effective length along the anode, w, the total charge per unit length inside r is,

$$q' = q - \frac{n_o e}{w} \exp\{\int_{r_o}^{r} \alpha dr'\}$$

where,

$$q = V_o/2X$$

is the original charge per unit length on the anode wire. The reduction in the electric field at r is consequently,

$$\Delta E(r) = 2\Delta q(r)/r = - \frac{2n_o e}{w} \exp\{\int_{r_o}^{r} \alpha dr'\}$$

We will use the following simple form for the first Townsend coefficient,

$$\alpha = D\ (E - E_o), \text{ with,}$$

$$D = 0.0262\ V^{-1}$$

$$E_o = 22{,}800\ V/cm$$

For V_o = 2300 V, the radius at which α goes to zero is,

$$r_o = V_o/E_o X = .0125 \text{ cm, and}$$

$$\Delta E(r) = - \frac{2n_o e}{w} \exp\{\int_{r_o}^{r} D(V_o/X)\ (\frac{1}{r'} - \frac{1}{r_o})\ dr'\}$$

$$= - \frac{2n_o e}{w} \exp\{\frac{DV_o}{X} (\ln \frac{r_o}{r} + \frac{r}{r_o} - 1)\}$$

Using the numberical values above, we get,

$$\Delta E(r) = \frac{n_o}{w} (2.88 \times 10^{-7}) \{(\frac{.0046}{r})^{7.45} e^{596r}\} \text{ V/cm}$$

The change in gain is given by,

$$\Delta \ln G = \int_{r_1}^{r_o} \Delta\alpha(r)dr$$

$$= \int_{r_1}^{r_o} D\Delta E(r)dr$$

Using the expression for $\Delta E(r)$, above, and plugging in the numbers, we get;

$$\Delta \ln G = 1.8 \times 10^{-4}\ n_o/w$$

In order to estimate w, we will use the measured relative gains for the main Fe^{55} peak ($n_o = 220$) and the escape peak ($n_o = 110$). At 2300 V we observed a gain ratio of 1.2 therefore,

$$\ln(1.2) = \Delta \ln G_{main} - \Delta \ln G_{escape}$$

$$0.175 = \frac{1.8 \times 10^{-4}}{w} \quad \frac{n_o}{2} = \frac{.02}{w}$$

This result can be used to establish an upper limit on w, because the actual time dependence of the process can only decrease the space charge effects. Hence, we have,

$$w \leq 0.11 \text{ cm}$$

We can compare this effective width with what we would expect from electron diffusion that was estimated earlier. The effective width of the lateral distribution is,

$$w = \sqrt{\pi}\ \sigma \simeq 0.08 \text{ cm}$$

The comparison with measurement above essentially amounts to examining the change in the space charge effects due to a change in the initial charge with the effective width assumed to be constant. Alternatively, we can make use of the observed variation of gain with angle of incidence of a penetrating particle for a chamber that is being operated in conditions for which space charge effects are significant. We have such measurements with C^{+6} ions at the Bevatron with a chamber using 75% Argon

- 25% Isobutane at 0, 10, and 20 degrees incidence. All we need from the analysis above is the result that:

$$\Delta \ln G \propto n_o/w$$

In this case, in addition to the spread of the discharge along the anode, we have a known geometrical contribution to the effective width of the charge distribution which is equal to $2L\tan\theta$. The number of primary electron-ion pairs is proportional to $\sec\theta$ due to the increased path length of an inclined track. The results are shown in Figure 4-7, in which we have plotted $\Delta \ln G \cdot \cos\theta$ v.s. w^{-1}. The relationship should be linear. In addition to the measured points at 10° and 20°, we know that $\Delta \ln G$ must go to zero for large θ because the charge would be spread over a very large length. If we extrapolate to the value of $\Delta \ln G$ observed at normal incidence we get

$$.050 \leq w \leq .070 \text{ cm}$$

Again, we have no indication of an effective width of the discharge that is not consistent with that expected from electron diffusion.

4.5 Space Charge Saturation

As positive charge accumulates around the wire, the field near the wire decreases, and the field at larger radii increases, in such a way as to keep the integral from anode to cathode equal to the applied voltage. The limiting value to which the field strength near the wire can be reduced is that value at which α decreases to zero and multiplication ceases. For the 80% Ar - 20% CO_2 mixture with our simple form for α this happens at $E_o/p=30$ V cm^{-1}Torr^{-1}.

The maximum space charge per cm that can be accumulated corresponds to a field which is equal to E_o out to some radius r_o, and then drops off: There can be no further multiplication beyond this point. There is an accumulation of charge out to r_o, but none beyond because the field there has always been less than E_o.

In order to simplify the calculation, we now approximate the MWPC by a cylindrical counter with the same anode wire radius, r_1, and the same capacitance per cm, C. For our MWPC configuration we have,

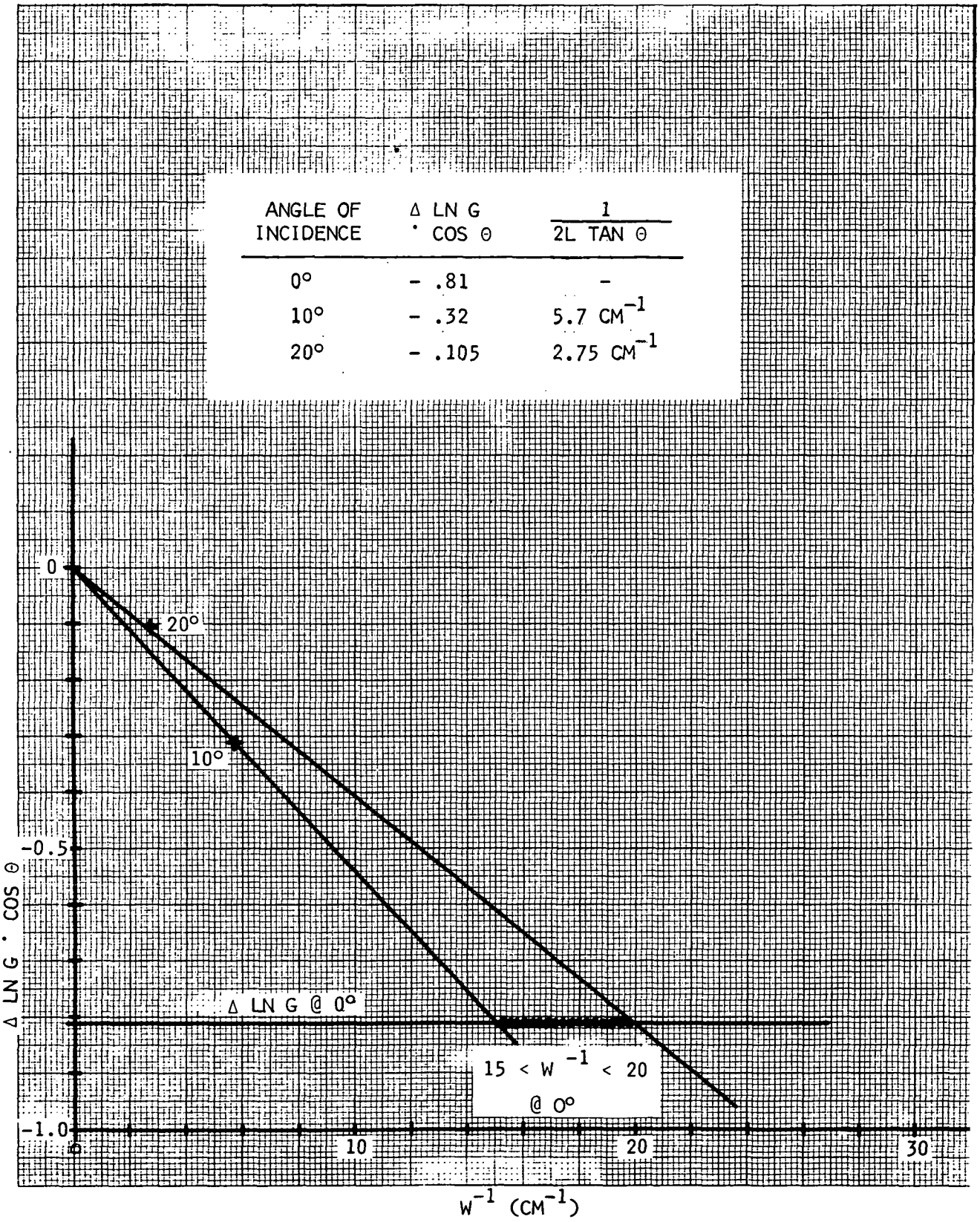

FIGURE 4-7. Analysis of the variation of gain with angle of incidence

$$C = 1/2\ X.$$

For a cylindrical counter,

$$C = 1/2\ \ln \frac{r_2}{r_1}$$

where r_2 is the cathode radius. Therefore,

$$\ln r_2 = X + \ln r_1. \tag{4-12}$$

The value of r_o is determined by the condition that the integral of the field from r_1 to r_2 be equal to the applied voltage. At the wire surface:

$$E_o = \frac{2q}{r_1}$$

In the same way, the field at the surface of any cylinder of radius r is determined by the charge inside the cylinder:

$$\int_{r_1}^{r_2} 2\pi r'\ Q(r')dr' = \frac{1}{2} E_o r$$

where Q is the charge density.

The solution is, $$Q(r) = \frac{E_o}{4\pi r}$$

The space charge per cm is,

$$q' = \int_{r_1}^{r_o} 2\pi r'\ Q(r')dr'$$

$$= \frac{1}{2} E_o\ (r_o - r_1) \tag{4-13}$$

and the total charge is

$$q+q' = \frac{1}{2} E_o r_o$$

The applied voltage is

$$V_o = E_o\ (r_o - r_1) + \int_{r_o}^{r_2} E_o r_o \frac{dr}{r}$$

$$V_o = E_o\ (r_o - r_1) + E_o\ r_o\ \ln \frac{r_2}{r_o}$$

Substituting $\ln r_2$ from equation (4-12), we get,

$$V_o = E_o(r_o - r_1) + E_o r_o(X + \ln r_1 - \ln r_o), \text{ or}$$

$$r_o/r_1 = \frac{1 + V_o/E_o r_1}{1 + X - \ln r_o/r_1} \qquad (4\text{-}14)$$

This equation can be solved for a given set of operating conditions (i.e. X, V_o, r_1, and E_o) to obtain r_o. The maximum charge per unit length, q', can then be determined from equation (4-14). We have calculated q' as a function of V_o for our chamber configuration with 20 micron anode wire diameter. The results are shown in Figure 4-8. The value of q' is seen to be comparable to the charge per unit length on the anode as would be expected. We can arrive at an estimate of the maximum gain realizable as a function of voltage under the assumption that the effective width of the discharge is equal to that due to electron diffusion ($\simeq$ 0.08 cm) and constant, since:

$$q' = n_o e\, G_{max}/w, \text{ or for } Fe^{55} \text{ X-rays,}$$

$$G_{max} = w\, q'/n_o e = .8 \times 10^6\, q' \text{ (esu/cm).}$$

The result is shown in Figure 4-2 along with the measured gas gain. If the measured gas gain exceeded G_{max} we would have a clear indication that the discharge must be spreading along the anode. Since, in fact, this is not the case we can only obtain an estimated lower limit on the effective width of the discharge by assuming that the maximum output signal that we measured corresponds to the space charge saturated gain. At 2500 V, we obtained an estimated total charge output of about 5×10^7 electrons. Therefore,

$$w \geq \frac{(5 \times 10^7)(4.8 \times 10^{-10})}{.6 \text{ esu/cm}} \text{ esu}$$

$$\geq 0.04 \text{ cm}$$

In conclusion, we have seen that the highly simplified analysis of space charge effects has placed the following limits on the effective width of the charge distribution of:

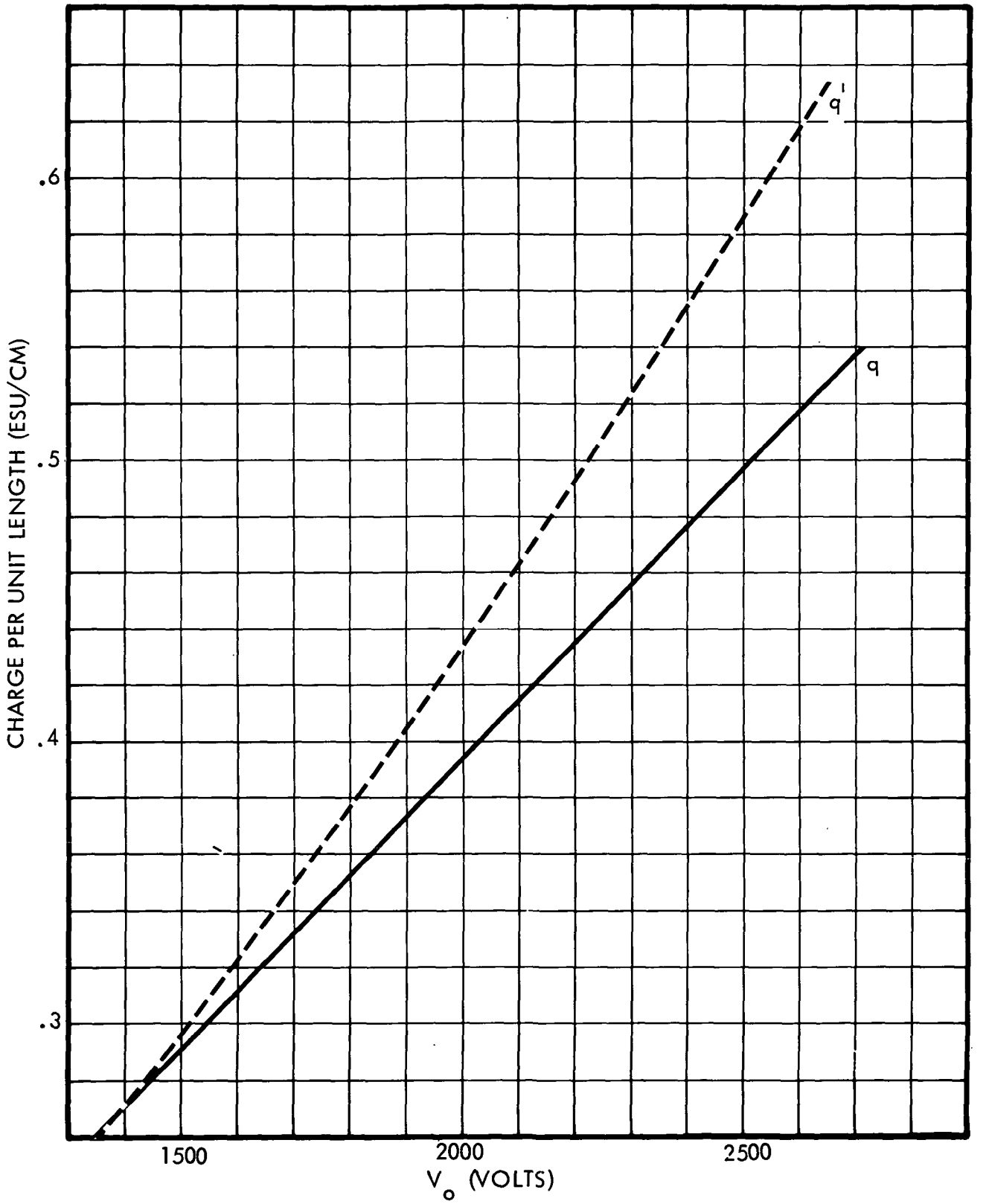

FIGURE 4-8. Charge per unit length and maximum charge per unit length v.s. high voltage V_o

$$0.04 \text{ cm} \leq w \leq 0.11 \text{ cm},$$

for operating conditions above the linear region but probably well below complete space charge saturation. This width is roughly the same as the effective width due to electron diffusion in the drift region. Therefore, we see no indication of significant spreading of the discharge along the anode under these conditions. It is possible that in the complex real situation of the space charge phenomenon, the shape of the charge distribution or the time dependence of the MWPC current pulse is being distorted in a manner that causes a degradation of spatial resolution.

5. SPATIAL RESOLUTION

Position determination using MWPC's with delay-line readout systems is usually based upon measuring the position of the peak of the induced distribution on the cathode planes. The accuracy of the position measurement is conceivably influenced by a number of parameters, which were mentioned in Section 3.2. These parameters are:

a. Diffusion of electrons and positive ions
b. Spread of the discharge along the anode wire
c. Inclination of the particle track
d. Delta rays
e. Signal to noise ratio

5.1 Diffusion of Electrons and Positive Ions

It turns out that the lateral diffusion of electrons and positive ions in the cascade region in the immediate vicinity of the anode wire does not contribute to errors in the position measurement because of the large number of these charge carriers in this region and because of the small radial extension of this region. However, the diffusion of the primary electrons in the drift region from the cathode to the anode until the cascade process starts can contribute significantly towards a position uncertainty.

The r.m.s. diffusion distance (one-dimensional) is given by,

$$\langle x \rangle = \sqrt{2Dt},$$

where D is the diffusion constant and t is the drift time through the anode-cathode gap. The problem would be straightforward if measured diffusion coefficients were available. Again we find that unfortunately such data does not exist for the commonly used MWPC gases. The diffusion coefficient is known for pure Argon, but it is not possible to enter a value for MWPC mixtures because a principle effect of the quenching additive (e.g. CO_2) is to radically reduce the mean electron kinetic energy which directly influences the diffusion coefficient. It is possible to calculate the diffusion coefficient if the mean electron kinetic energy is known. Hough[22] indirectly arrives at an estimate of mean electron kinetic energy and diffusion coefficients for Argon-methane mixtures. For 90% Argon - 10% methane he estimates and experimentally verifies a FWHM single-electron resolution of approximately 1 mm. This value includes electronic noise and source width contributions of 0.3 mm each. The diffusion contribution that we infer from these results is 0.65 mm FWHM or about 0.3 mm rms. We have estimated the mean electron kinetic energy in 80% Argon - 20% CO_2 to be about 3eV for the drift region electric fields in our normal operating conditions. This leads to an estimated rms diffusion distance of 0.24 mm for a 5 mm drift distance.

For n primary electrons the r.m.s. diffusion is

$$\sigma = \langle x \rangle / \sqrt{n}$$

For a minimum ionizing, singly changed particle which produces about 100 primary electrons in our chamber, the position uncertainty of the peak of the induced charge distribution due to diffusion thus is approximately

$$\sigma = 25\mu$$

at normal incidence.

The position uncertainty of 5.9 KeV Fe-55 x-rays, which produce about 220 primary electrons, is according to our calculations $\sigma = 16\mu$. This does not take into account, however, the lateral extent of the primary ionization due to the conversion process of the x-rays into electrons.

The x-rays are almost entirely absorbed by the argon atoms. The probability that absorption leads to the emission of an electron from the K-shell is:

$$P_K = 0.90$$

and for the L-shell:

$$P_L = 0.10$$

The fluorescence yields are:

$$\omega_K = 0.11$$

$$\omega_L = 0.01$$

The probability of escape of the K x-ray is:

$$\epsilon_K \simeq 0.9$$

Eighty-one percent of the time we get K-shell absorption followed by de-excitation via the Auger effect. This will result in the production of two 3-KeV electrons at the point of interaction.

Eight-to-nine percent of the time there is one 3-KeV electron (escape peak).

Zero-to-one percent of this time there are two ~ 3-KeV electrons at different points in the chamber (reabsorption of the Ar K x-ray). The mean free path of the Ar K x-ray is $\lambda = 3.8$ cm; the two points will, therefore, in general be several millimeters apart.

Ten percent of the time there are one 5.65-KeV electron and one 0.24-KeV electron (L-shell absorption).

The range of a 3-KeV electron in the gas is about 0.1 mm. For the two-electron case, if the directions of emission are not correlated, the r.m.s. distance along one axis between the point of origin and the centroid of the ionization distribution is 20 microns. If there is only one 3-KeV electron, this distance becomes 30 microns. These two cases between them cover 90% of the events. Since the value of σ, the r.m.s. position error, is in general determined on the basis of the width of the curve at the 50% or 60% point, it will not be affected by the other 10% of the cases, it appears that electron ranges contribute about 20-25 microns to the measured value of σ for Fe^{55} x-rays.

5.2 Spread of the Discharge Along the Anode Wire

The symmetry of the induced charges on both cathode planes and in the neighboring anode wires indicates that the discharge spreads around the whole anode wire regardless of the position of the primary ionization. Therefore, with an anode wire diameter of 20 microns, the discharge spreads 20 to 40 microns in each direction around the wire. It seems reasonable to assume that the discharge spreads at least this far along the wire. As a matter of fact, due to the diffusion of the primary electrons, which is $\langle x \rangle = 240\mu$ for a single electron, the spread is several times this distance. As long, however, as the discharge spreads equally in both directions, the peak of the induced charge distribution accurately represents the position of the primary ionization. This is true as long as the peak remains well defined and doesn't spread significantly.

We can get a rough idea of the upper limit on the spread of the discharge along the anode by observing the spatial distribution of the induced signals on the cathode wires. The expected induced charge distribution varies with position as

$$\frac{1}{L^2+x^2}$$

where L is the distance from anode to cathode. The f.w.h.m. of this distribution is 2L or about 10 mm in our chamber. We have measured the induced charge distribution in the strictly proportional region of our chamber and find a f.w.h.m. of 11 mm. This difference can be accounted for by the contribution of electron diffusion discussed above. This indicates that the discharge does not significantly spread along the anode wire in the proportional region, and that it might not contribute significantly to uncertainties in position measurements. There is the possibility that at sufficiently high gains, space charge effects might significantly affect the spread of the discharge along the anode. We examined this possibility in more detail in Section 4.5 and came to the conclusion that the width of the charge distribution at high gas gain is still roughly the same as the effective width due to electron diffusion.

The results of our spatial resolution measurements, which will be pre-

sented below, show,however, that the measured spatial resolution saturates with increasing gas gain or signal to noise ratio, which can be interpreted as an indication that our simplified analysis does not represent the complex real situation at high gas gains, and that the shape of the charge distribution is distorted in such a manner as to degrade the spatial resolution.

5.3 Inclined Trajectories

If a particle enters a MWPC with an inclined trajectory (inclined in the anode wire plane) the discharge will spread out along the anode wire and the amount of spread will depend on the degree of inclination. Measurements we have carried out with collimated electron sources show that a serious deterioration of the spatial resolution occurs for inclined tracks. This does present a problem for cosmic ray experiments which accept inclined particles over a wide range of angles. One way to reduce the effect of inclined tracks in MWPC's operated with normal gas is to reduce the gap width in order to reduce the length of the discharge along the anode wire.

5.4 Delta Rays

A limitation on the spatial resolution of MWPC's is the spatial distribution of the primary ionization produced by the passage of a charged particle through the MWPC gas. Specifically, secondary electrons (delta rays) are produced which have energies such that their range is greater than the magnitude of the uncertainties in position location that we have discussed above. On the average, delta rays are produced symmetrically around the particle's trajectory and should have no first order effect on the position of the peak of the induced cathode charge. However, the frequency of high energy delta ray production is low enough that the statistical fluctuations in delta ray production can lead to asymmetries in the induced charge distribution and thus to significant uncertainties in the position measurement of individual events. In addition, the problem can be aggrevated if the MWPC is operated above the strictly proportional region, in which case the primary ionization does not multiply linearily. In effect, the ionization produced by delta rays outside the main core of ionization will be weighted more heavily.

In order to make a quantitative estimate of the potential severity of the delta ray problem, a computer program was generated that uses Monte Carlo techniques to simulate delta ray effects (see Section 8). The results of these calculations, which have been carried out for particles with an energy of 2.1 GeV/nucleon and different Z values, show that delta rays can have a serious effect on position measurements. Indications are that the irreducible delta ray effects are essentially of the order of or less than the spatial resolution we want to achieve (100-200 microns) for relativistic nuclei with $Z \leq 4$, and increases to about 1 mm for $Z = 26$.

5.5 Signal to Noise Ratio

The electronic noise of the readout system and the resolution limitations due to the signal to noise ratio will be discussed in the next section. The analysis of the delay-line readout system shows that the signal to noise ratio at moderately high gas gains in the proportional region is not a limiting factor.

5.6 Summary

In summarizing the above discussion we can conclude that none of the discussed effects seems to significantly limit the achievable spatial resolution for minimum ionizing, singly charged particles at normal incidence and for Fe-55 x-rays. A resolution of $\sigma \leq 100\mu$ should be achievable in the proportional region of our chamber. We have to remember, however, the assumption that the spread of the discharge along the anode wire is insignificant in that region.

Accordingly we can calculate the theoretical limit of spatial resolution for our chamber for 5.9 KeV x-rays for the conditions of our measurements:

Diffusion: 16μ
Lateral extension of primary ionization: 20μ
Source width: 45μ (see Section 7.1)
Electronic Resolution: 45μ (see Section 6.4 and Figure 6-10 for 2100 volts)
Theoretical Resolution: $\sigma = \sqrt{16^2+20^2+45^2+45^2} = 70\mu$

The real limitations in spatial resolution in high energy cosmic ray experiments are posed by the delta-ray problem and by inclined trajectories.

6.0 LUMPED ELEMENT DELAY-LINE ANALYSIS

6.1 Introduction

Various MWPC readout systems and their advantages and disadvantages have been discussed in Section 3.1. It was pointed out that accurate position determination of an ionizing event can be achieved with delay line readout systems which determine the position of the induced charge distribution on the cathode planes of the MWPC.

Since the achievable spatial resolution is proportional to the signal to noise ratio of the readout system, delay lines which are directly coupled to both cathode planes are preferred over delay lines which, for example, are capacitively coupled to only one cathode plane. The integral delay line of Gilland and Emming[19] could be considered the ultimate realization of a directly coupled delay line concept since it uses the MWPC itself as the line. However, as we have pointed out before, the strong dependence of the characteristics and performance of the integral delay line upon the MWPC geometrical configuration leads to a significant loss in chamber design flexibility. In fact, the dependence upon chamber configuration could lead to constraints in chamber design which are unacceptable to the experiment's objectives. Another disadvantage of the integral delay line is the added mechanical complexity due to the introduction of sense planes between the anode and cathodes, and the requirement that relatively large diameter wires have to be used for the sense planes in order to reduce the line attenuation to reasonable numbers.

The lumped delay line readout system presented here allows near perfect charge coupling efficiency, independent optimization of chamber and delay line parameters and spatial resolutions of the order of 100 μm (for Fe^{55} X-rays) with the chamber operating at a reasonable gain in the proportional region. The use of lumped element delay lines for MWPC readout is not new, having been proposed by Charpak, et al.[17]; however, an analysis has not been presented that identifies the key design parameters and predicts the achievable performance. This section describes an approximate analysis that may be used to choose optimum delay line parameters and to evaluate the effect of electronics noise on the achievable spatial resolution.

6.2 Delay-Line Analysis

The creation of an avalanche in the small region surrounding an anode wire causes charge to be induced on adjacent anode wires and on the cathode planes. If we defined Q_A as the total charge on the active anode wire and Q_I, the total charge induced on the neighboring anode wires, then the total charge induced on the cathode wires, Q, is given by

$$Q = Q_A - Q_I \tag{6-1}$$

Q_I is dependent upon the geometrical configuration of the chamber and can typically be 10 to 20% of Q_A. The induced cathode charge may be expressed as

$$\frac{Q_N}{Q} = \frac{1}{\pi} \frac{L/S}{(\frac{L}{S})^2 + N^2} \tag{6-2}$$

for wire cathode planes. In Equation (6-2), L is the anode plane to cathode plane spacing, S is the cathode wire spacing and N is the wire number (with N = 0 being that cathode wire directly below the anode charge).

The analysis of the lumped element delay line readout system requires a mathematical representation of the cathode current pulses. Measurements performed on a small chamber indicate that the anode current pulse (and hence the induced cathode current pulse) may be modeled as

$$i(t) = Q \frac{t}{\tau^2} e^{-t/\tau} \tag{6-3}$$

For Fe^{55} X-rays in a 90% A, 10% CO_2 gas mixture we measured a model pulse time constant, τ, of 20 ns. The model pulse used in this analysis exhibits a risetime of approximately 11 ns, a FWHM of 49 ns and a peaking time of 20ns. The model pulse time constant for X-rays is actually not very sensitive to changes in operating conditions (gas and high voltage) over our operating range, due to the concentration of the primary ionization in a small, localized region. Non X-ray events can be expected to have different τ's.

The amplitude of the model cathode current pulse of Equation 6-3 is de-

pendent upon the location of the cathode wire with respect to the anode charge (Equation 6-2). Therefore, the current pulse on the N^{th} cathode wire can be written as

$$i_N(t) = Q_N \frac{t}{\tau^2} e^{-t/\tau}$$

$$= \frac{Q}{\pi} \frac{L/S}{(L/S)^2 + N^2} \frac{t}{\tau^2} e^{-t/\tau} \qquad (6\text{-}4)$$

Consider a tapped delay line of infinite bandwidth and a constant group delay of t_{dl} seconds between taps. Each tap is connected to its corresponding cathode wire. The delay line output may be written as

$$i_T(t) = \sum_{N=-M}^{M} \frac{Q_N}{\tau^2} (t-Nt_{dl}) e^{-(t-Nt_{dl})/\tau} U(t-Nt_{dl}) \qquad (6\text{-}5)$$

where M wires either side of the zeroeth are assumed to contribute significantly to the output. The function U(t) is the unit step function defined as

$$U(t) = \begin{cases} 0 & t < 0 \\ 1 & t \geq 0+ \end{cases}$$

(The delay from N = 0 to the end of the line has been ignored here since all wires are affected equally.)

The effect of a bandwidth-limited, lossless delay line is to reduce the amplitude of the pulse and to spread it in time. As will be demonstrated, the bandwidth of the line as measured from an input applied to one of the taps is a function of the number of delay line sections between the tap and the line output. One may model the physically realizable delay line of Figure 6-1 (a) as shown in Figure 6-1 (b). Here the individual inputs are applied to ideal delay lines whose delay is a function of the distance between the input and the line output. Each delay line output is then applied to a filter representing the bandwidth of the line as seen by an input applied to the particular tap in question. The delay line output is therefore the weighted sum of the individual cathode current pulses. Knowledge cf the impulse response of the component

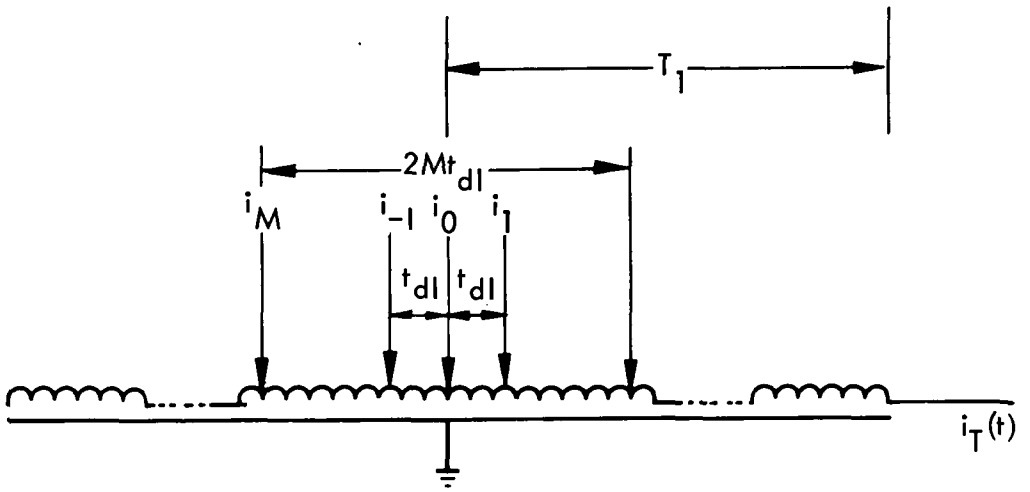

(a)

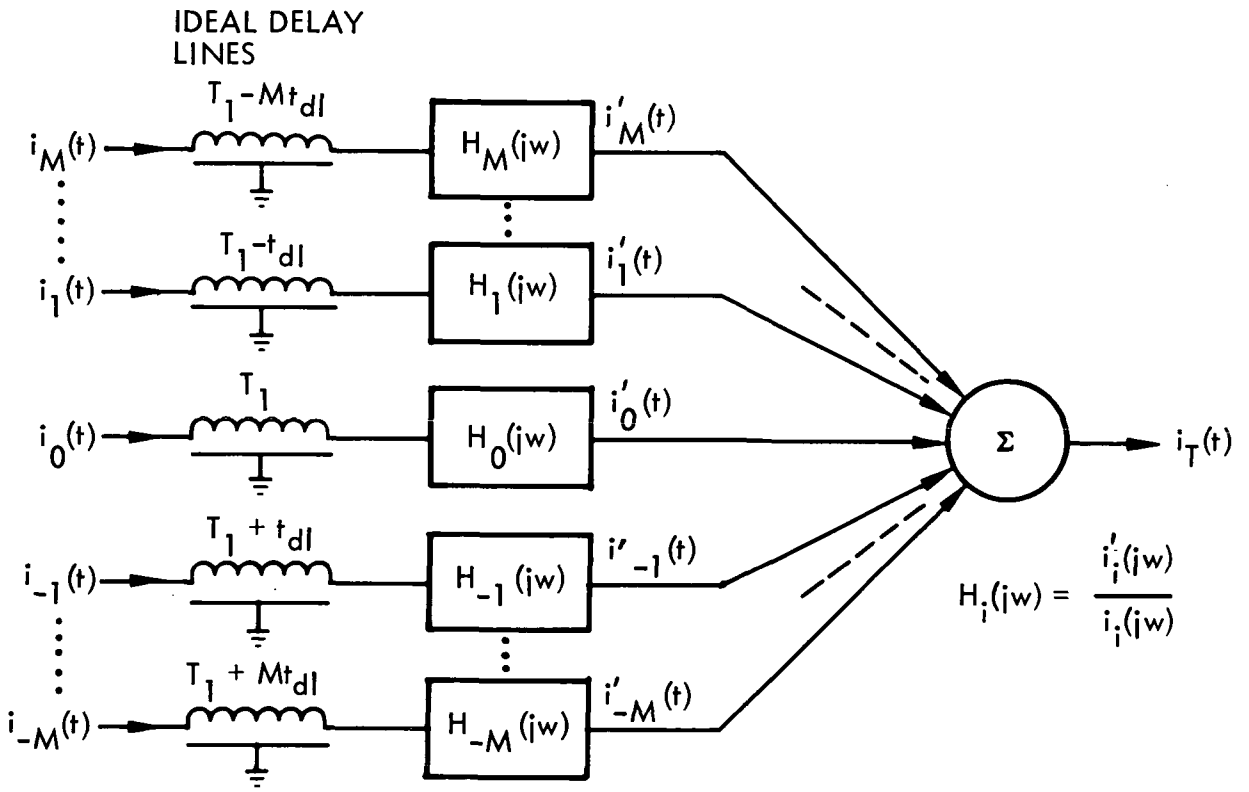

(b)

FIGURE 6-1. Development of delay-line model

filters shown in Figure 6-1 (b) is required in order to calculate the delay line output. The following paragraphs will present a discussion of a lumped element delay line and an approximation to its impulse response.

A lumped element approximation to a delay line having equal delay between taps may be realized by cascading constant-k T sections, as shown in Figure 6-2. The end termination networds are m-derived half-sections including to improve the matching between the line and R_o.

The delay line design equations are:[23]

$$t_{rl} = 1.13\sqrt{LC}, \text{ risetime per section}$$

$$t_{dl} = 1.07\sqrt{LC}, \text{ delay per section}$$

$$t_d = n\, t_{dl}, \text{ delay for n sections}$$

$$t_r = \sqrt[3]{n}\, t_{rl}, \text{ risetime for n sections}$$

$$R_o = \sqrt{\left(\frac{L}{C}\right)} \text{ characteristic impedance}$$

Therefore, for fixed n the delay to risetime ratio is constant. (Note: Should a faster risetime be desired for the same delay, additional T sections may be added to the line between tap locations.)

The theoretical impulse response of an equal element lumped delay line involves Bessel functions of high order. Convolution of the model pulse and the line's impulse response yields the line's output signal. This problem in itself is a time consuming computer operation and when one considers that it must be done for each cathode wire containing a "significant" fraction of the charge (because of the dependence of the order of the Bessel function on wire number), it becomes apparent that obtaining the theoretical solution is very expensive.

In light of the computational difficulties just described, the following simplified analysis will be employed. The impulse response of the delay line can be approximated in the form shown below (neglecting the fixed delay):

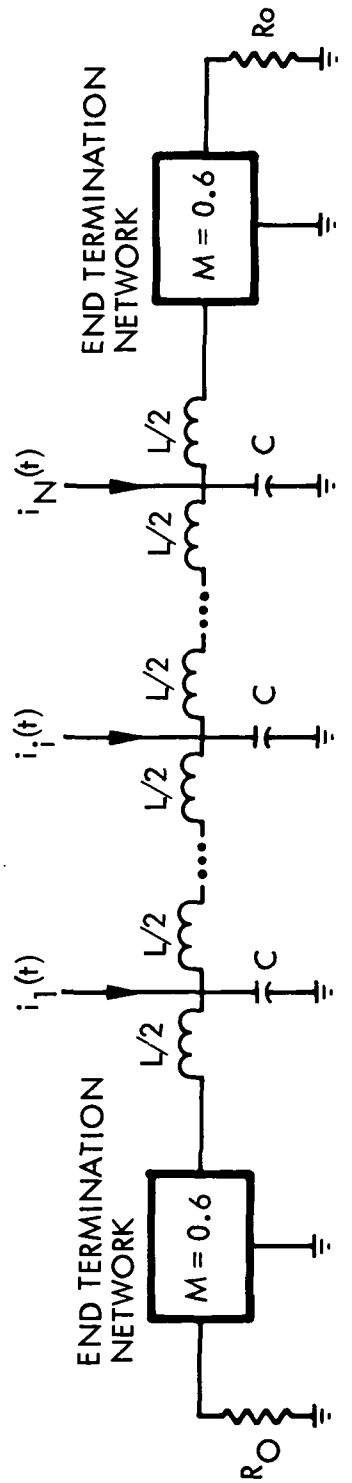

FIGURE 6-2 Lumped element delay-line

$$K(t)=\begin{cases}\frac{2}{T}\sin^2\frac{\pi t}{T} & 0\leq t\leq T\\ 0 & t\leq 0, t\geq T\end{cases} \qquad (6\text{-}6)$$

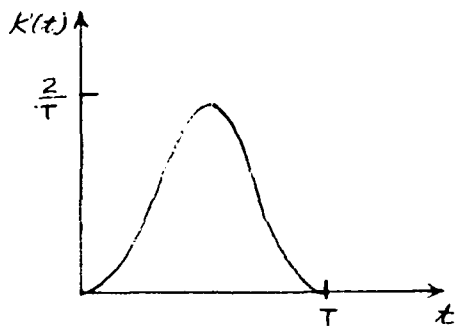

Integrating K(t) yields the step response:

$$S(t)=\begin{cases}0 & t<0\\ \frac{t}{T}-\frac{1}{2\pi}\sin\frac{2\pi t}{T} & 0\leq t\leq T\\ 1 & t\geq T\end{cases} \qquad (6\text{-}7)$$

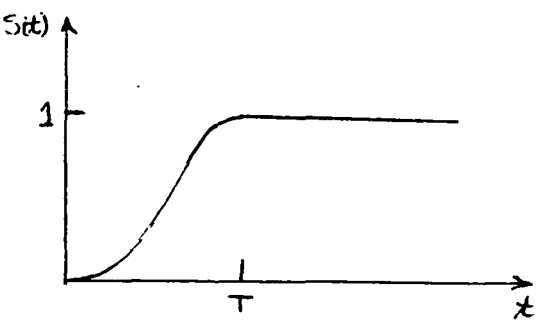

The 10 to 90% risetime of the waveform of Equation (6-7) is calculated to be $t_r = 0.4822T$. As before, the risetime of the line is given by

$$t_r = \sqrt[3]{n}\, t_{r1}$$

or

$$T = 2.19 \sqrt[3]{n}\, t_{d1} \tag{6-8}$$

Convolving the model pulse,

$$i(t) = \frac{Q_0 t}{\tau^2} e^{-t/\tau}$$

with the impulse response approximation, Equation (6-6) yields, after a considerable amount of arithmetic, the delay line output for a single input:

$$i'(t) = \begin{cases} \frac{Q_0}{T}\left[1-(1+\frac{t}{\tau})e^{-t/\tau}+\frac{2}{(1+\beta^2)^2}\left(\frac{\beta^2-1}{2}\cos\omega t-\beta\sin\omega t\right)+\frac{e^{-t/\tau}}{1+\beta^2}\left(\frac{t}{\tau}-\frac{\beta^2-1}{\beta^2+1}\right)\right], & 0\le t<T \\ 0, & t<0 \\ \frac{Q_0}{T}e^{-t/\tau}\left\{(1+\frac{t-T}{\tau})e^{T/\tau}-1-\frac{t}{\tau}+\frac{1}{1+\beta^2}\left[\frac{t}{\tau}-\frac{\beta^2-1}{\beta^2+1}-(\frac{t-T}{\tau}-\frac{\beta^2-1}{\beta^2+1})e^{T/\tau}\right]\right\}, & t\ge T \end{cases} \tag{6-9}$$

where $\omega = \frac{2\pi}{T}$, $\beta = \frac{2\pi\tau}{T}$ and T is given by Equation 6-8.

Let the line have N_1 sections in total with the anode point charge located above the N_oth tap, as shown in Figure 6-3.

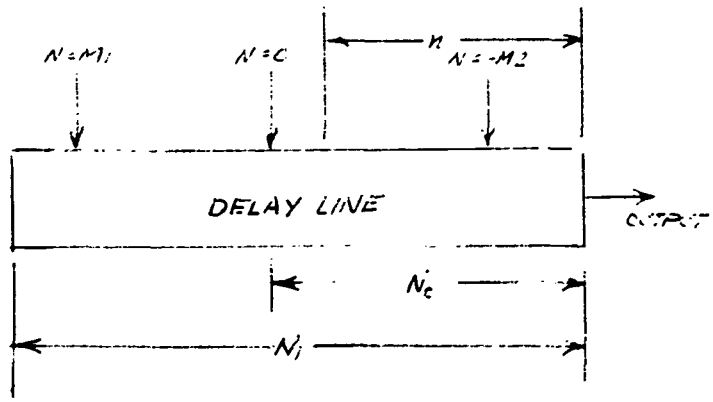

FIGURE 6-3

It will be assumed that the M1 + M2 wires located around the center of mirrored charge distribution contribute significantly to the output pulse. (Note that as long as $M1 \leq N_1 - N_o$ and $M2 \leq N_o$, we will have $M1 = M2 = M$). The delay line output, $i_T(t)$, may now be written (from Figure 6-1) as

$$i_T(t) = \sum_{N=-M2}^{M1} i'_N(t-Nt_{dl})U(t-Nt_{dl}) \tag{6-10}$$

Substituting Equation (6-9) into 10 yields

$$i_T(t)= \sum_{-M2}^{M1} \frac{Q_N}{T} \{i_1(t-Nt_{dl})[U(t-Nt_{dl})-U(t-Nt_{dl}-T)]+i_2(t-Nt_{dl})U(t-Nt_{dl}-T)\} \tag{6-11}$$

where Q_N is given by Equation 6-2 and i_1 and i_2 are defined below:

$$i_1(t)=1 - (1+ \frac{t}{\tau})e^{-t/\tau}+ \frac{2}{(1+\beta^2)^2} (\frac{\beta^2-1}{2} \cos\omega t-\beta\sin\omega t) + \frac{e^{-t/\tau}}{1+\beta^2} (\frac{t}{\tau} - \frac{\beta^2-1}{\beta^2+1})$$

$$i_2(t) = e^{-t/\tau}\{(1 + \frac{t-T}{\tau})e^{T/\tau}-1- \frac{t}{\tau} + \frac{1}{1+\beta^2} [\frac{t}{\tau} - \frac{\beta^2-1}{\beta^2+1} -(\frac{t-T}{\tau} - \frac{\beta^2-1}{\beta^2+1})e^{T/\tau}]\}$$

It should be noted that the output waveform described by Equation 6-11 has been shifted in time so that the cathode pulse applied at section N = 0 occurs at t = 0 at the output. The effect of the bandwidth variation with input position is treated by noting that

$$T = 2.19 \sqrt[3]{N_o + N}\, t_{dl} \tag{6-12}$$

The delay line, when electrically connected to the chamber, exhibits an increase in risetime over the isolated line. Computer simulation of the delay line indicates that intertap parasitic capacitance added by the printed circuit pattern interconnecting the chamber and line is responsible for this effect. In order to account for the reduced delay line

bandwidth, the value for T given by Equation (6-12) is increased. For our typical laboratory delay line (L = 4.7 μh, C = 20 pf, $C_{intertap}$ = 2 pf), the observed risetime is approximately twice that predicted by the design equations and hence we will see $T = 4.38 \sqrt[3]{N_O + N}\, t_{dl}$ when referring to the "loaded" case. Accompanying the increased risetime is an increase in the overshoot in the step response; from approximately 6% for the isolated line to 30% for the loaded line. Because of the smoothing effect of the multiple cathode inputs, the output waveform appears relatively clean. In some applications, however, the ringing may be objectionable and a suitable phase correction filter should be incorporated at the delay line output.

6.3 Implementation of the Lumped Element Delay-Line

The method of interconnecting the cathode planes and the technique of coupling them to the delay line warrants some comment. For illustration, the chamber will be assumed to be 50 x 50 cm with a cathode wire spacing of 2 mm. The resultant 500 cathode wires must be connected to the delay line. It has been previously mentioned that in order to achieve the highest charge coupling efficiency, both cathode planes must be directly connected to the delay line.

Figure 6-4 indicates the evolution of the adopted configuration. Figure 6-4 (a) shows a straight-forward mechanization of the constant-k delay line which is further simplified to the configuration of Figure 6-4 (b). Employing the self-inductance of the cathode wires and the anode-cathode capacitance (augmented with external capacitance, if necessary) yields the delay line-chamber system of Figure 6-4 (c). Notice that in all three drawings the winding sense of the cathode wires, i.e. essentially bifilar, is such as to minimize the mutal inductance thereby maintaining a constant-k delay line. An m-derived delay line may be easily developed from the last figure as shown in Figure 6-4 (d). Although the m-derived form (similar to that achieved in the integral delay line chamber) offers a small potential improvement in group delay constancy with frequency over the constant-k line, it does require that the chamber be so sized as to yield the proper amounts of self and mutual inductances. The constraint imposed here may require a compromise between chamber parameters (such as gap width) and delay line parameters.

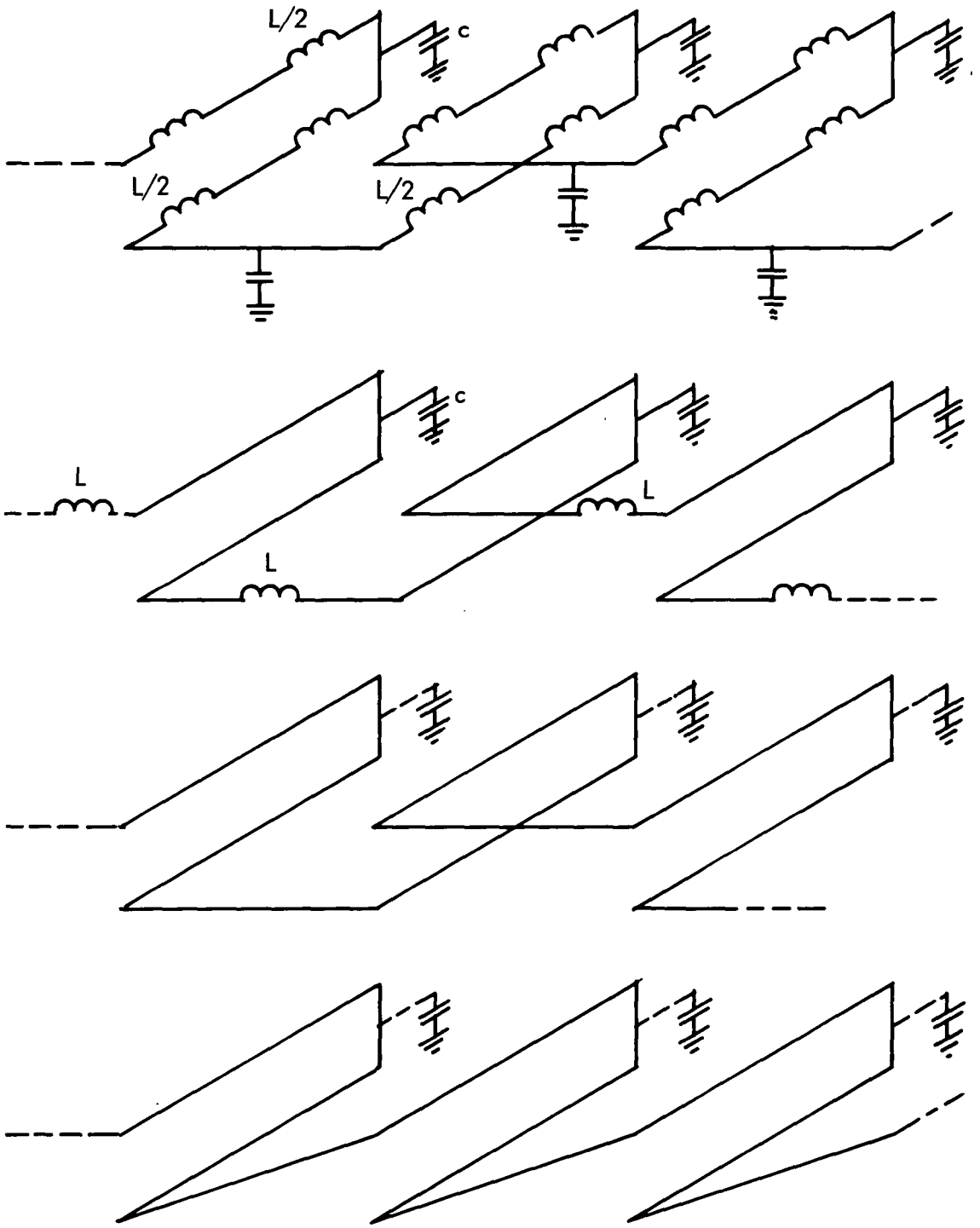

FIGURE 6-4 Mechanization of chamber delay-line system
(a) Realization of constant-k delay-line using the canonic T-sections
(b) Simplification of (a)
(c) Same as (a) and (b) but employing self-inductance of cathode wires
(d) M-derived line employing self and mutual inductance of cathode wires.

Each of the chamber-delay line systems of Figure 6-4 have the cathode wires in series with the delay line elements. If one uses the smallest cathode wire size compatible with mechanical and electrostatic stability, then a serious attenuation and noise source results from the wire resistance. For example, 50 μ diameter Cu-Be cathode wires (spaced 2 mm in the 50 x 50 cm chamber) contribute over 6000 ohms in series with the line. Of course larger wire sizes may be used at the cost of increased mass density across the MWPC sensitive area and possibly larger frame-width if additional tensioning of the wires becomes necessary.

The adopted configuration of Figure 6-5 avoids the aforementioned problems while still allowing for direct coupling to both cathode planes. The cathode wire-delay line connection alternates between the upper and lower cathode planes in order to achieve a bifilar winding. Connection between the cathode wires and the discrete delay line components are made by a printed circuit board.

6.4 Effect of Electronic Noise on Spatial Resolution

The effect of electronics noise upon system spatial resolution is readily determined. For the purposes of this report the readout system is as shown in Figure 6-6 and consists of electronics viewing each end of the delay line. Each delay line output is amplified by a low noise voltage preamplifier. The preamp outputs are then fed to two identical constant fraction discriminators (CFD's). The individual CFD outputs then become the start and stop inputs to a pulse height to time converter whose output is then accumulated in a multichannel analyzer.

The preamplifier is modeled as an ideal (noiseless) amplifier with current and voltage noise represented explicitly by the two noise sources (assumed to be uncorrelated) of noise spectral densities $\overline{i_A^2}$ and $\overline{e_A^2}$, respectively, Figure 6-7. The delay line and its termination resistance, R_0, has associated with it the Johnson noise voltage represented by the noise spectral density, $\overline{i_R^2}$. The signal, derived from the superposition of the individual cathode pulses, is labeled i_T.

The total equivalent amplifier output noise spectral power density is found to be

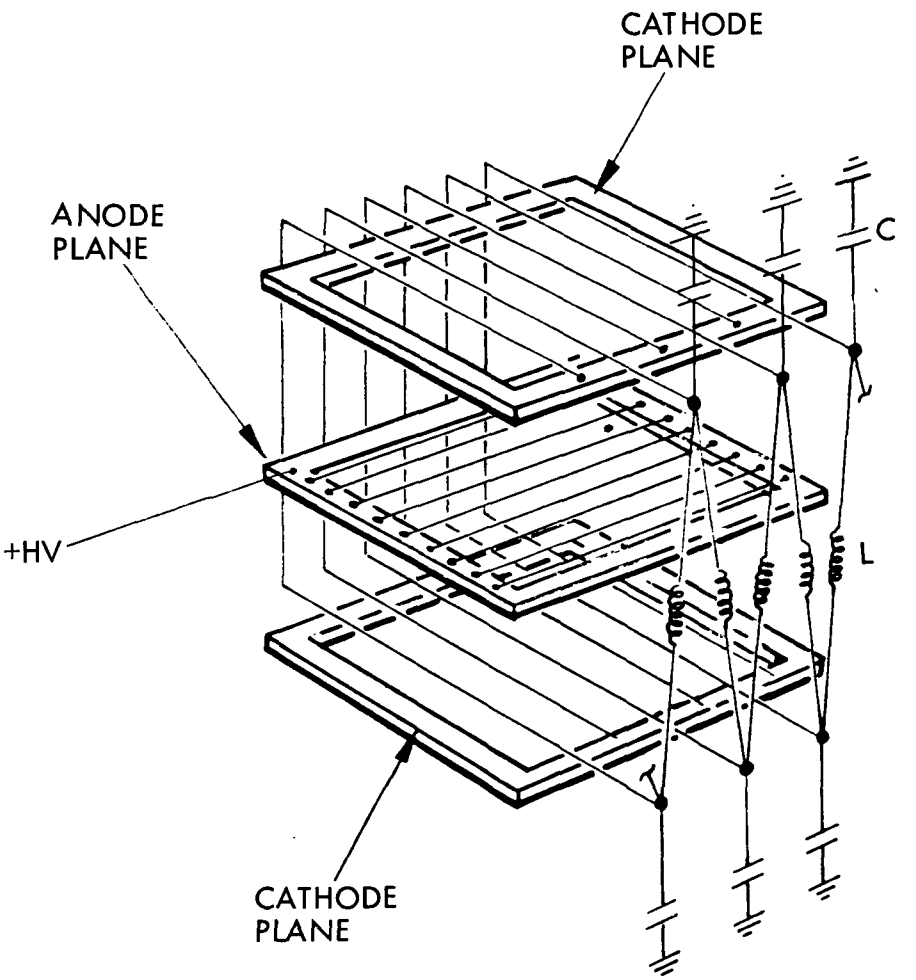

FIGURE 6-5 Adopted delay line - chamber configuration

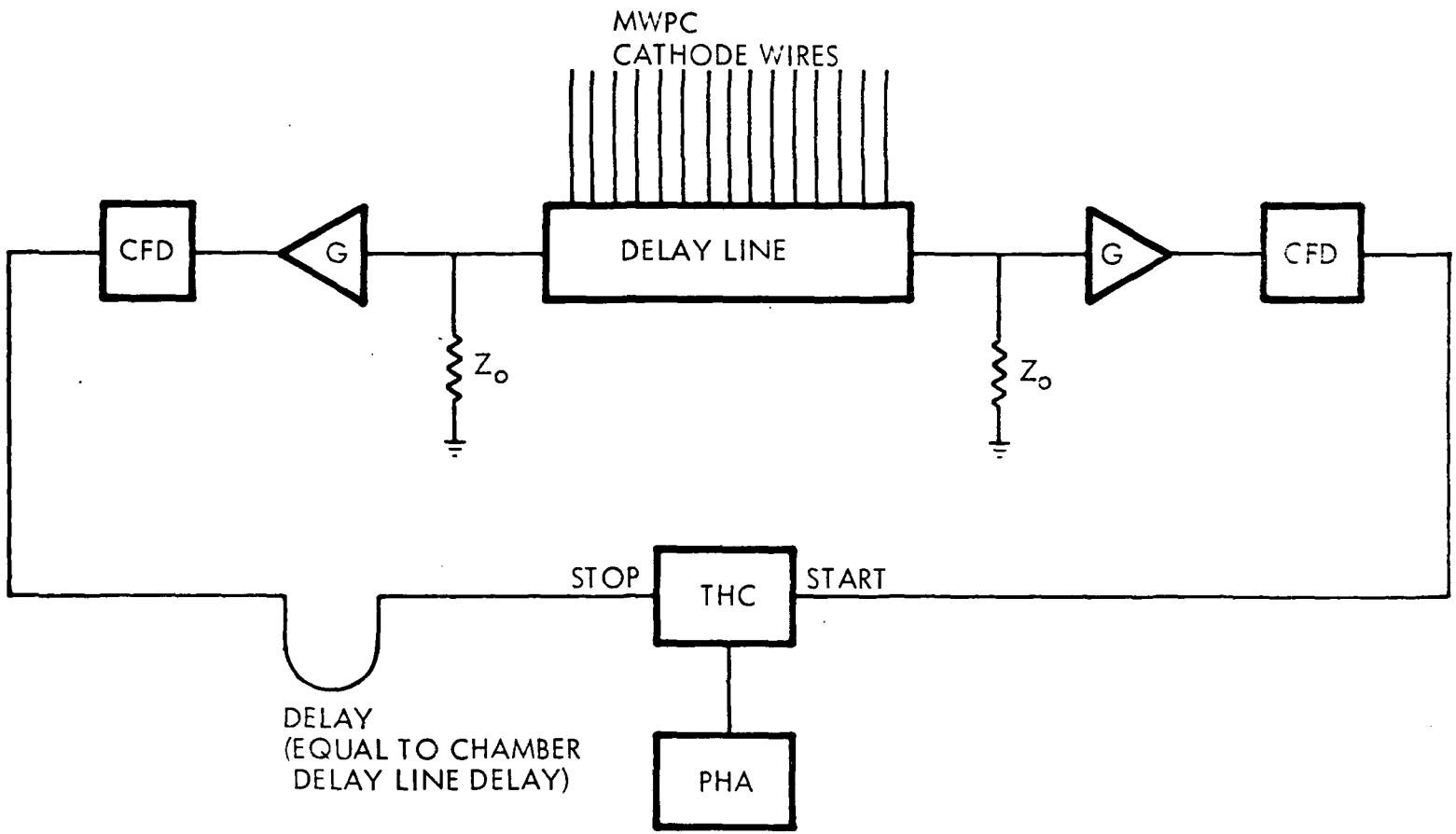

FIGURE 6-6. Experimental setup for resolution measurements

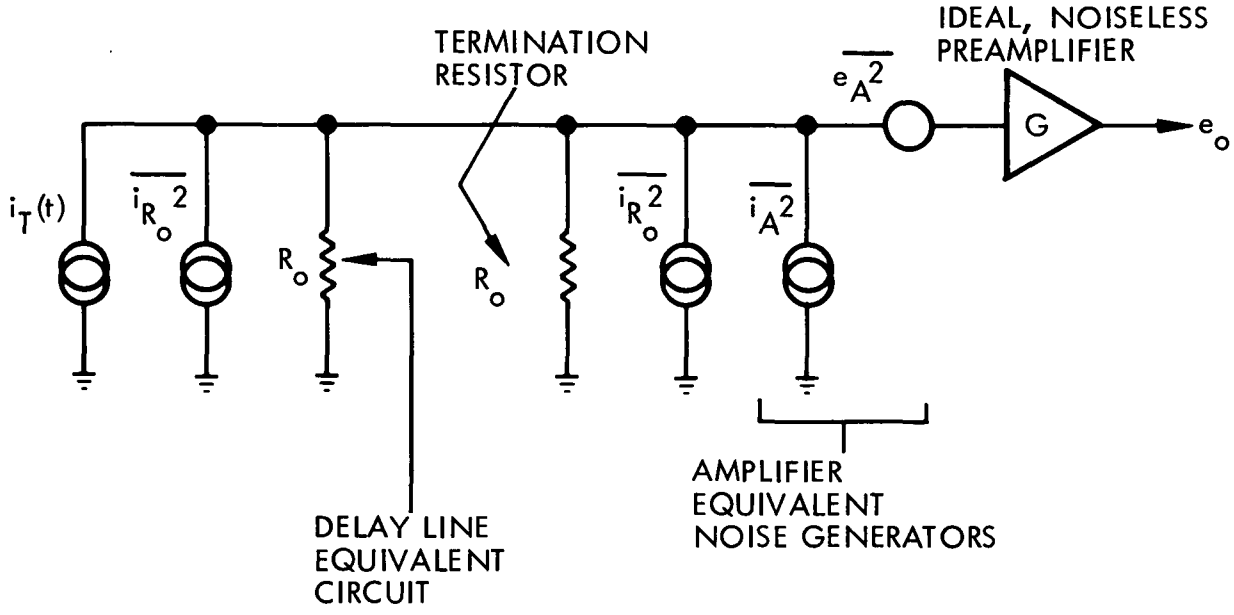

FIGURE 6-7. Delay-line and preamplifier equivalent circuit

$$\overline{e_{no}^2} = G^2\{\overline{e_A^2} + \overline{i_A^2}\,\frac{R_o^2}{4} + \overline{i_R^2}\}\ (V^2/Hz) \qquad (6\text{-}13)$$

where

$$\overline{i_R^2} = 2KTR_o \text{ and}$$

where K is Boltzman's constant and T is the absolute temperature (°K).

The bandwidth required to pass the delay line output signal is a function of the risetime of the signal. The noise bandwidth may then be expressed as

$$NBW = \frac{K_1}{t_{ro}}$$

Computer plots of the delay line output as expressed by Equation 6-11 show the signals to be approximately Cos^2 in shape. If one assumes that a system bandwidth sufficiently wide to encompass 90% of the signal energy is required in order to faithfully reproduce it, then $K_1 = 0.6$.

The output noise power in this bandwidth is therefore simply

$$\overline{e_{no}^2} = G^2\ \{\overline{e_A^2} + \overline{i_A^2}\,\frac{R_o^2}{4} + 2KTR_o\}\,\frac{K_1}{t_{ro}}\ (Volts^2)$$

The peak output signal amplitude is

$$\hat{e}_o = \frac{GR_o}{2}\,\hat{i}_T\,.$$

Defining the normalized peak output current for a given t_{d1} as

$$f(\frac{td_1}{\tau}) = \frac{\hat{i}_T\ (t_{d1})}{\hat{i}_T\ (t_{d1}=0)}$$

we can write that (from Equation 6-3)

$$\hat{i}_T = \frac{Q}{\tau}\,e^{-1}\,f(\frac{t_{d1}}{\tau})\,.$$

The output peak-signal to rms noise voltage ratio is then

$$S/N = \hat{e}_o / \sqrt{\overline{e_{no}^2}}$$

$$= \frac{R_o\, e^{-1}}{2\tau}\, Q\, f\, \left(\frac{t_{dl}}{\tau}\right)\, \left(\frac{t_{ro}}{K_1}\right)^{1/2}\, \left(\overline{e_A^2} + \overline{i_A^2}\, \frac{R_o^2}{4} + 2KTR_o\right)^{-1/2}$$

Using the simple model of Figure 6-8 for the effect of noise upon the timing accuracy of the CFD yields an estimate of the rms timing jitter:

$$\sqrt{\overline{t_j^2}} = \frac{(1 - f_1)\, t_{ro}}{0.8\ S/N}$$

where f_1 if the fraction,

or

$$\left(\overline{t_j^2}\right)^{1/2} = \frac{2(1-f_1)\tau}{0.8e^{-1}Q}\, \frac{(K_1 t_{ro})^{1/2}}{f\, \left(\frac{t_{dl}}{\tau}\right)}\, \frac{\left(e_A^2 + i_A^2\, \frac{R_o^2}{4} + 2KTR_o\right)^{1/2}}{R_o} \qquad (6\text{-}14)$$

The time jitter described by Equation (6-14) is dependent upon the location of the peak of the charge distribution on the line. Except for the special case of an event centered on the line, it is necessary to evaluate the two delay line outputs and sum in quadrature the CFD time jitters to arrive at the total system jitter. For the purposes of simplicity, we will assume that the event occurred at the center of the line and, hence, the overall jitter is given by Equation (6-14) multipled by $\sqrt{2}$. Computer studies of the delay line readout system indicate that the resolution achieved with a charge located above the center of the chamber is maintained out to approximately a gap width from the edge of the active area where it begins to degrade due to the truncation of the mirrored cathode charge distribution.

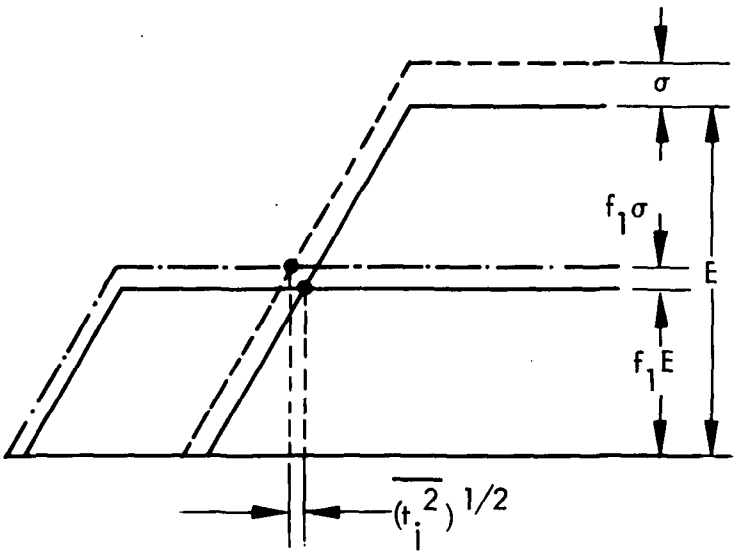

FIGURE 6-8. Simplified model for calculating time jitter of constant fraction discriminator due to noise

The spatial resolution, σ_s, achieved is given by

$$\sigma_s = \frac{S}{t_{dl}} \left(\frac{\overline{t_j^2}}{2}\right)^{1/2}$$

$$= 4.805 \frac{(1-f_1)S}{Q} (K_1\tau)^{1/2} \frac{(tro/\tau)^{1/2}}{\frac{t_{dl}}{\tau} f\left(\frac{t_{dl}}{\tau}\right)} \frac{\left(\overline{e_A^2} + \overline{i_A^2}\frac{R_o}{4} + 2KTR_o\right)^{1/2}}{R_o} \quad (6\text{-}15)$$

for an event located at the center of the chamber.

The spatial resolution clearly has a minimum (i.e. a minimum of the spatial inaccuracy) at the maximum of the function,

$$g = \frac{t_{dl}}{\tau} f\left(\frac{t_{dl}}{\tau}\right) / \left(\frac{t_{ro}}{\tau}\right)^{1/2}$$

This function is plotted in Figure 6-9 for a 50 cm chamber with cathode wire spacing of 2 mm and an anode-cathode spacing of 5 mm. The model pulse time constant was 20 ns and the loading effect was included.

The plot of Figure 6-9 indicates that there exists an optimum interwire delay of approximately 4 ns for the cathode readout line for this particular MWPC. It should also be noted that this optimum is fairly broad, hence some flexibility in component selection is available to make use of standard values, for example.

The last term of Equation (6-15) is dependent upon preamplifier and termination resistor noise levels. The resolution improves as $\sqrt{R_o}$, hence as large as delay line impedance as practical is desired. The spatial resolution of the chamber described above with a delay line of 1000Ω characteristic impedance, a delay of 4.5 ns/section (i.e. 2.25 ns/mm) and a preamplifier with $(\overline{e_A^2})^{1/2} = 5$ nV/$\sqrt{\text{Hz}}$ and $(\overline{i_n^2})^{1/2} = 0.3$ pA/$\sqrt{\text{Hz}}$ is given by $\sigma_s = 4.22 \times 10^{-14}$ mm-coul/Q for $f_1 = 0.5$, $K_1 = 0.6$, and the "loading" effect considered.

Considering only the electronic system, it appears that a resolution of 100 microns can be achieved with an anode charge of 4.2×10^{-13} coul

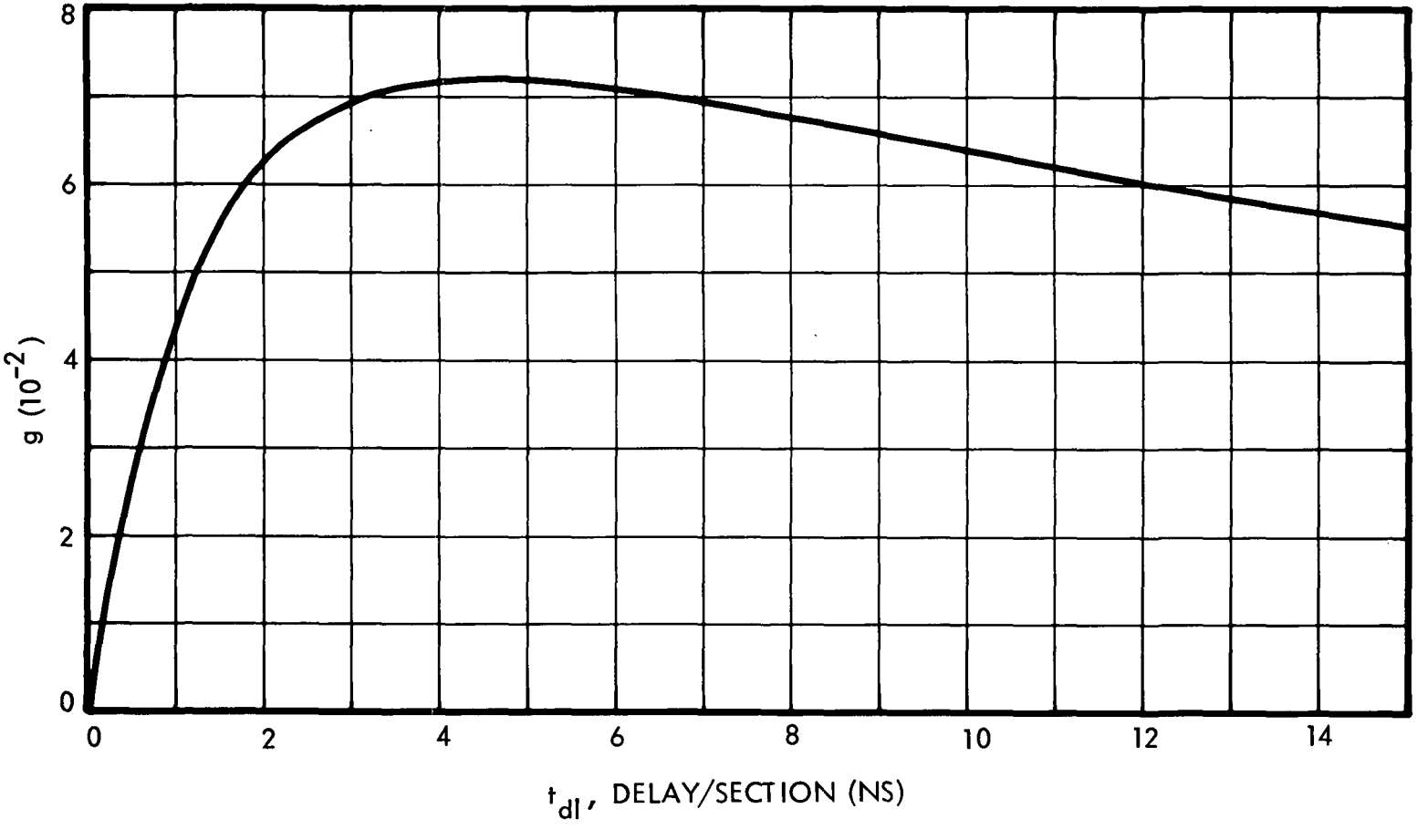

FIGURE 6-9. Optimum delay per section for chamber with N_1=250, N_o=125 s = 2mm, L=5mm and for a model-pulse time constant, τ = 20 ns loading effect considered

corresponding to approximately 2.7 x 10^6 electrons dependent, of course, on Q_I.

6.5 Experimental Work

An experiment was performed with our standard chamber in order to test the validity of the analysis in predicting the achievable spatial resolution. The chamber was operated with a flowing gas mixture of 90% Argon-10% CO_2 at one atmosphere.

The delay line was designed to utilize standard component values and was found to have a delay of 8.8 ns/section (i.e. 4.4 ns/mm) and a characteristic impedance of 825 ohms.

The test setup of Figure 6-6 was used with a micrometer mounted, collimated Fe^{55} source. The voltage preamplifier exhibited an estimated rms voltage noise of 5 $nV\sqrt{Hz}$ and current noise of 0.3 $pA\sqrt{Hz}$.

The experimental results are plotted in Figure 6-10 as a function of chamber high voltage and anode charge, which represents the relative gas gain as explained in Section 3. As expected, the resolution improves with increasing high voltage until it becomes limited by chamber properties. These sources of resolution degradation are discussed in Section 5.

According to the above analysis, applied to this chamber configuration, the experimental MWPC readout system should exhibit a resolution given by

$$\sigma = 3.86 \times 10^{-14} \text{ mm-coul/Q}$$

for the source centered on the chamber and with loading considered. The same system with a noiseless preamplifier would have a resolution given by

$$\sigma = 1.80 \times 10^{-14} \text{ mm-coul/Q}$$

under the same conditions. Based on these results (considering only the readout system as limiting the resolution), it should be possible to achieve a 100 micron resolution for 2.4 x 10^6 electrons using a practical preamplifier.

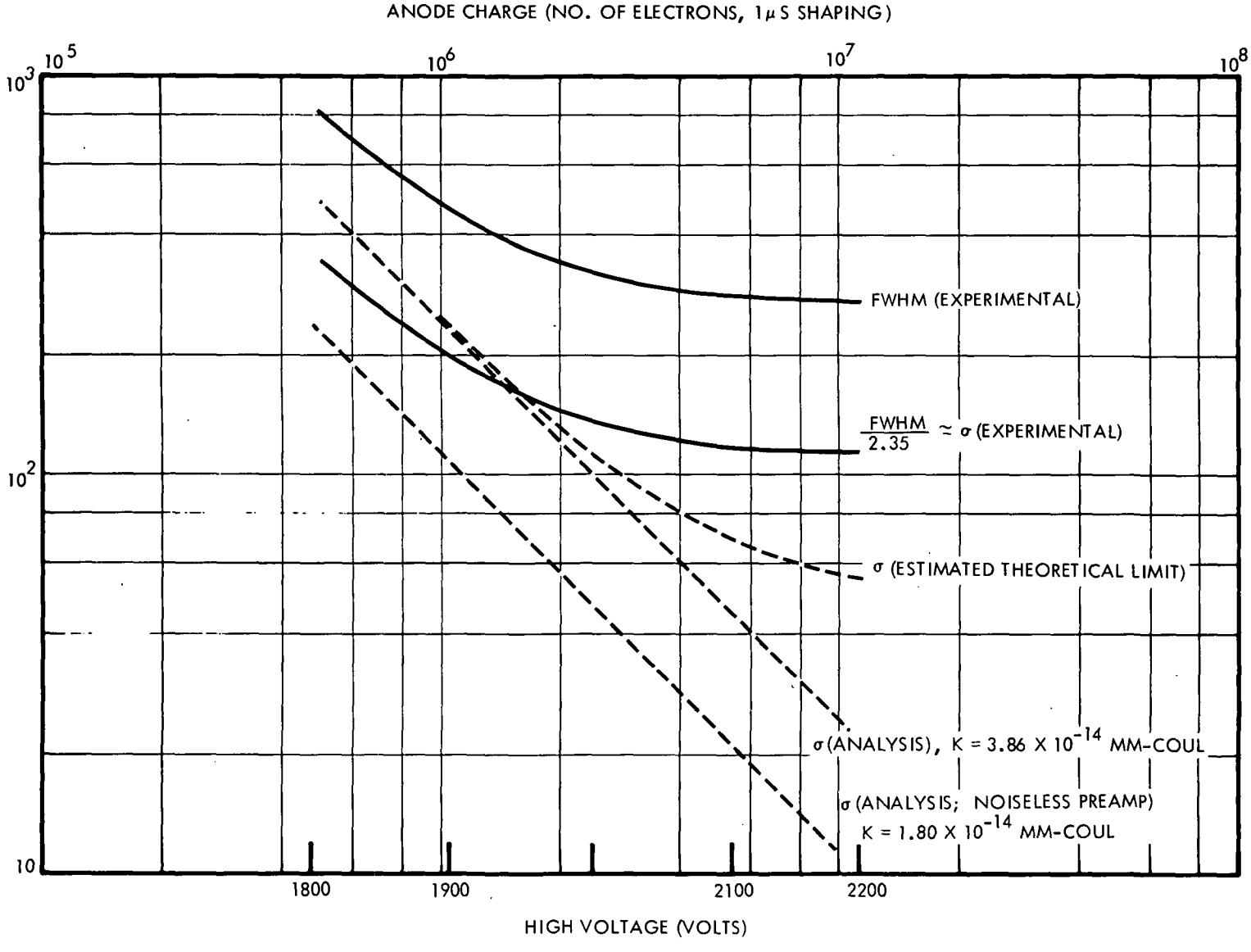

FIGURE 6-10 Spatial resolution as function of H.V. and anode charge in 90% A + 10% CO_2 with a collimated Fe-55 source. Comparison of experimental and theoretical results.

For an Fe^{55} X-ray source (5.9 KeV) and normal gases, approximately 220 primary electrons are created requiring a chamber gas gain of approximately 1.8×10^4. (When one speaks of gas gain in this context, it must be remembered that the readout system is only responsive to the cathode charge pulse for a time of the order of the total line delay time. The charge contained in the cathode signals in this period is some 40 to 50 percent of the total anode charge (for a $\sim$ 1 μs long line). The total delay of the experimental line was approximately 200 ns and the anode charge was measured with a charge sensitive preamplifier followed by single integration, double differentiation shaping of equal 1 μs time constants. The difference in these two "integration times" (i.e., that of the anode signal processing electronics and the delay line electrical length of $\sim$ 200 ns) should yield an error of about 25% in the estimate of the anode charge. Because of this discrepancy, the actual resolution is correspondingly better than indicated by the graph of Figure 6-10.

7. SPATIAL RESOLUTION MEASUREMENTS

Resolution measurements were carried out with our standard chamber which was outfitted with a lumped element delay line which is described in detail in Section 6. The measurements were carried out with a collimated Fe-55 source and a collimated β-source (Ru-106/Rh-106). The experimental setup for measurements with the β-source is shown in Figure 7-1. Each end of the delay line was viewed by a low noise voltage amplifier which feeds into a constant fraction discriminator (CFD). The individual CFD outputs were used as start and stop pulses for a time to amplitude converter (TAC) whose output was accumulated in a multichannel analyzer. The analyzer then displayed the position distribution. The width of the distribution represents the spatial resolution.

Fe-55 Source: The Fe-55 source was deposited on a 25μ diameter wire and collimated by an adjustable slit. It could be moved across the thin chamber window in accurately measured steps by a micrometer mounted source holder. The width of the x-ray beam in the chamber gap was calculated to be

$$\sigma = 45\mu$$

β-Source: The β-source which was used to study the effect of inclined tracks, was similar to the Fe-55 source in construction. However, even with a well collimated source ($\sigma \leq 50\mu$ in our case) it is difficult to achieve a well collimated electron beam in the sensitive region of the chamber because of multiple scattering of the electrons. To reduce the amount of scattering we mounted the source in a vacuum housing which was separated from the MWPC gap by a 1-mil Mylar window, as shown in Figure 7-2. The source could be rotated to measure the spatial resolution as a function of the angle of inclination. The average r.m.s. width of the electron beam in the 1 cm gap at 0° inclination was calculated to be about 150μ for 3 MeV electrons. This increased to about 200μ for 2 MeV electrons.

For our measurements with the β-source we placed a plastic sintillator behind the chamber to select only high energy electrons above about 2 MeV. The PHA was gated by the discriminator output.

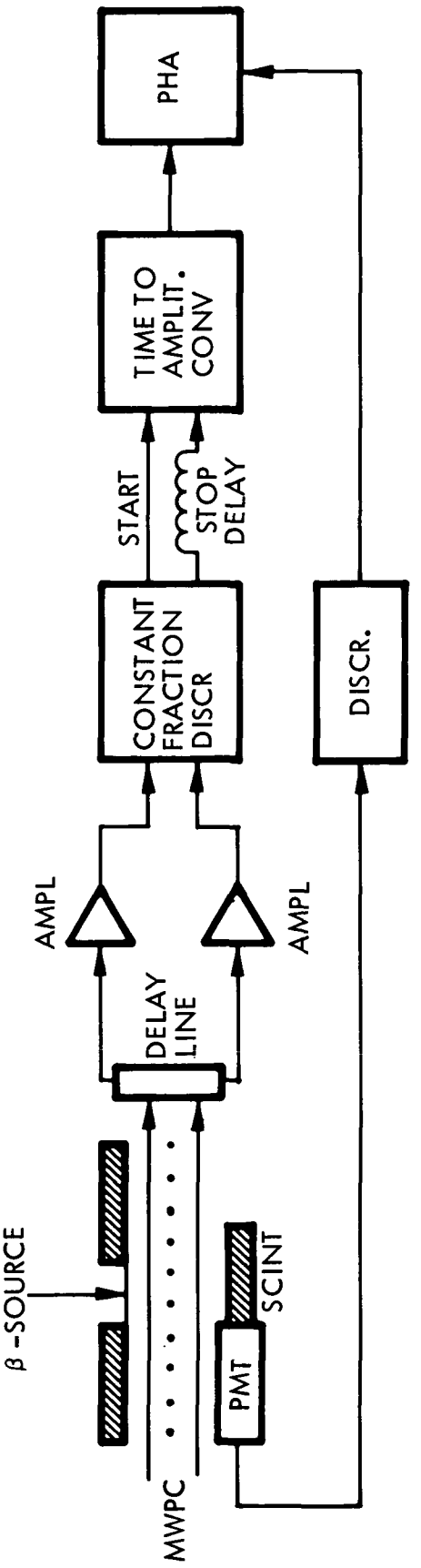

FIGURE 7-1. Experimental setup for resolution measurements with β-source

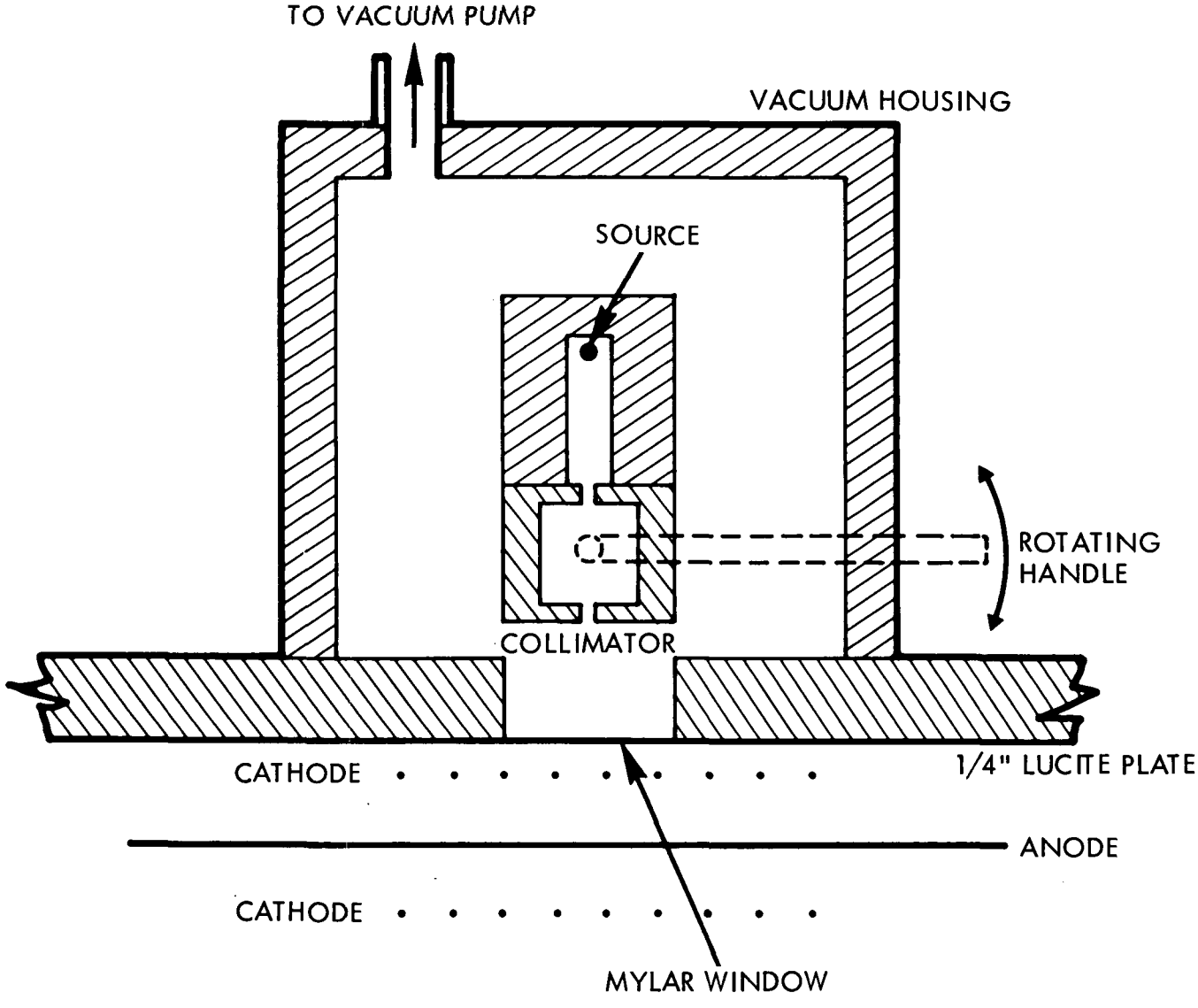

FIGURE 7-2. Source arrangement for collimated β-source

7.1 Results with Fe-55 Source

Figure 6-10 from the previous section shows the results of resolution measurements with a collimated Fe-55 source in 90% Ar + 10% CO_2 as a function of the chamber voltage. The corresponding gas gain curve is curve b in Figure 4-4. Plotted is the observed f.w.h.m. of the position distribution and the spatial resolution which is defined as

$$\sigma = \frac{\text{f.w.h.m}}{2.35}$$

Also shown is the resolution of the electronic readout system predicted by the delay-line analysis and the estimated contributions to the position uncertainty due to electron diffusion, lateral range of the primary ionization and source width.

The somewhat surprising results are that the measured resolution does not significantly increase with increasing signal to noise ratio but rather flattens out to a value of 120μ, and that the measured resolution does not approach the estimated theoretical limit. Since the noise of the system according to the delay line analysis is insignificant at the higher voltages, this may indicate that the spread of the discharge along the anode wire could be a significant limiting effect, which compensates the improvement in signal to noise ratio.

Position distributions taken at four different positions at 2100 volts are shown in Figure 7-3. The distance between points was on the average 3.3 mm. Figure 7-4 shows the position resolution at 2000 volts. The PHA calibration was 27.5μ/channel in both cases.

7.2 Results with Electrons

Measurements with the collimated electron source were carried out to investigate the effect of inclined tracks on spatial resolution. The measurements were done with 90% Ar + 10% CO_2 at 2300 volts. The corresponding beam width at 0° inclination was calculated to be σ = 200μ. The source width increased with increasing inclination due to the longer pathlength of the electrons in the MWPC gas:

$$\sigma = \frac{200}{\cos^{5/2}\theta}$$

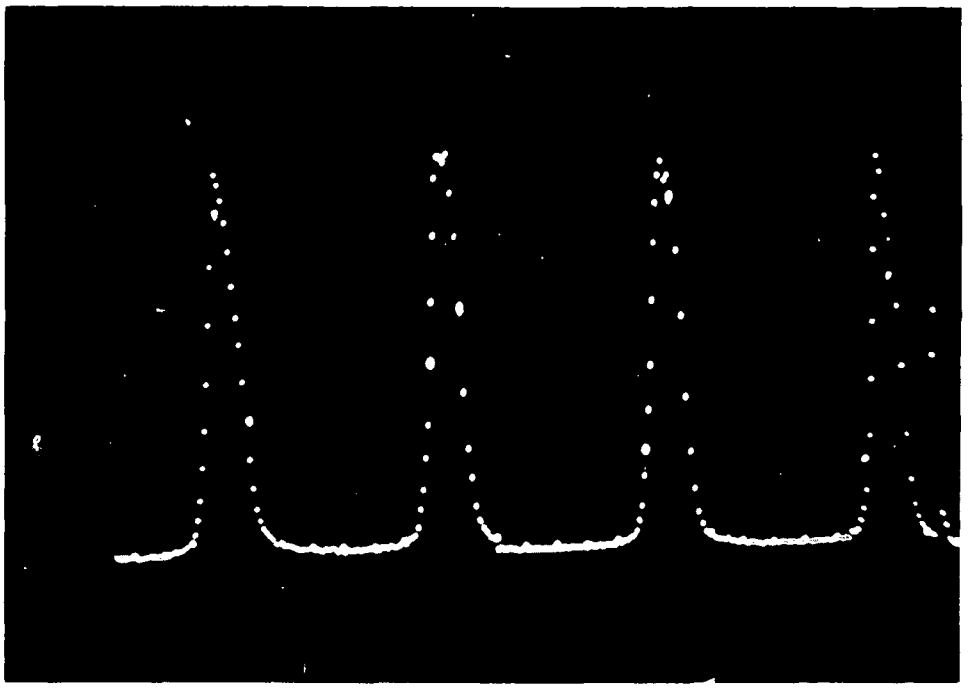

FIGURE 7-3 Position distributions for collimated Fe-55 source at 2100 volts in 90% Ar + 10% CO_2. Distance between peaks: 3.3 mm

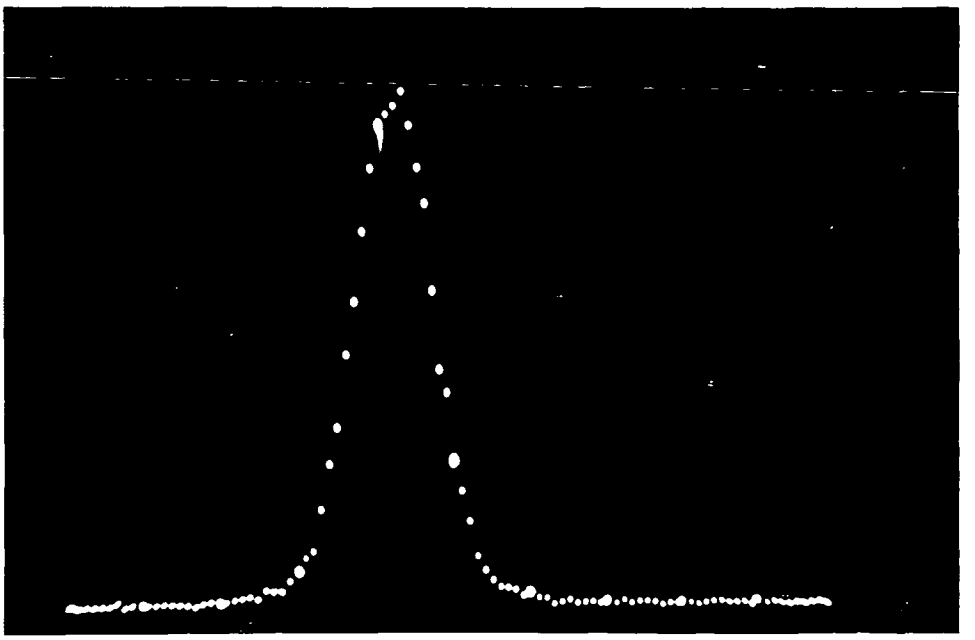

FIGURE 7-4. Position distribution at 2000 volts

The source width was unfolded from the measured width of the position distribution according to

$$\sigma^2_{measured} = \sigma^2_{real} + \sigma^2_{source}$$

The measured and real resolution as a function of angle of inclination is shown in Table VII-1, which shows that the spatial resolution deteriorates significantly with increasing angle of inclination.

TABLE VII-1

Resolution as a function of angle of inclination HV = 2300 volts, 90% Ar + 10% CO_2.

Inclination	σ meas.	σ real
0°	246μ	140μ
5°	293μ	213μ
10°	305μ	227μ
15°	328μ	245μ
20°	422μ	350μ
24°	504μ	437μ

8. DELTA-RAY CALCULATIONS

8.1 Introduction

One of the limitations on the spacial resolution of a MWPC is the spatial distribution of the primary ionization produced by the passage of a charged particle through the MWPC gas. Specifically, secondary electrons (delta-rays) are produced which have energies such that their range is greater than the magnitude of the uncertainties in position location that we have been discussing. On the average, the delta-rays are produced symmetrically with respect to the particle trajectory and if the position determination was based upon the centroid of the charge collected in the MWPC, no systematic bias would be produced. However, the frequency of high-energy delta-ray production is low enough that the statistical fluctuations in delta-ray production might significantly increase the uncertainty of the position measurement of individual events. In addition,

if the MWPC does not linearly multiply the ionization deposited, due to space charge effects, the problem may be aggrevated. In effect, the ion pairs produced by delta-rays outside of the main core of primary ionization would be more heavily weighted because of the reduction in multiplication of the primary ionization column by space charge effects. The extreme case would be saturated chamber operation (e.g., "magic" gas operation) for which the MWPC response to an individual delta-ray would be equal to that for the primary ionization column. Finally, the whole problem is complicated if there is a magnetic field present. The Lorentz forces on the delta-rays are sufficient to radically alter their trajectories in a systematic way and to produce errors in the position determination.

In order to make a quantitative estimate of the potential severity of these delta-ray effects, a computer program was generated that uses Monte-Carlo techniques to perform a computer simulation of delta-ray effects. For this first-order assessment of the problem, a number of simplifications were used to limit the complexity of the problem. The most significant of these simplifications are the neglect of the effects of multiple coulomb scattering and magnetic fields on the delta-ray trajectories. Delta-rays were propogated in a straight line from their point of production to the end of their range. In addition, range straggling was also neglected. Magnetic-field and multiple-Coulomb-scattering effects can be added to the computer simulation if necessary, but at the cost of a considerable increase in program complexity and computing time. The following is a description of the first-order computer simulation and a summary of the results for a simple detector configuration.

8.2 Description of the Computer Program

The geometry of the problem used in the computer simulation is shown in Figure 8-1. The formulae used in the computer simulation for delta-ray production by heavy, charged particles are given in Table VIII-1. The program is set up to handle up to five layers of material along the incident particle direction. The first material layer is treated as the sensitive region of the MWPC. The program simulates the passage of incident particles through this combination of materials on an event-by-event

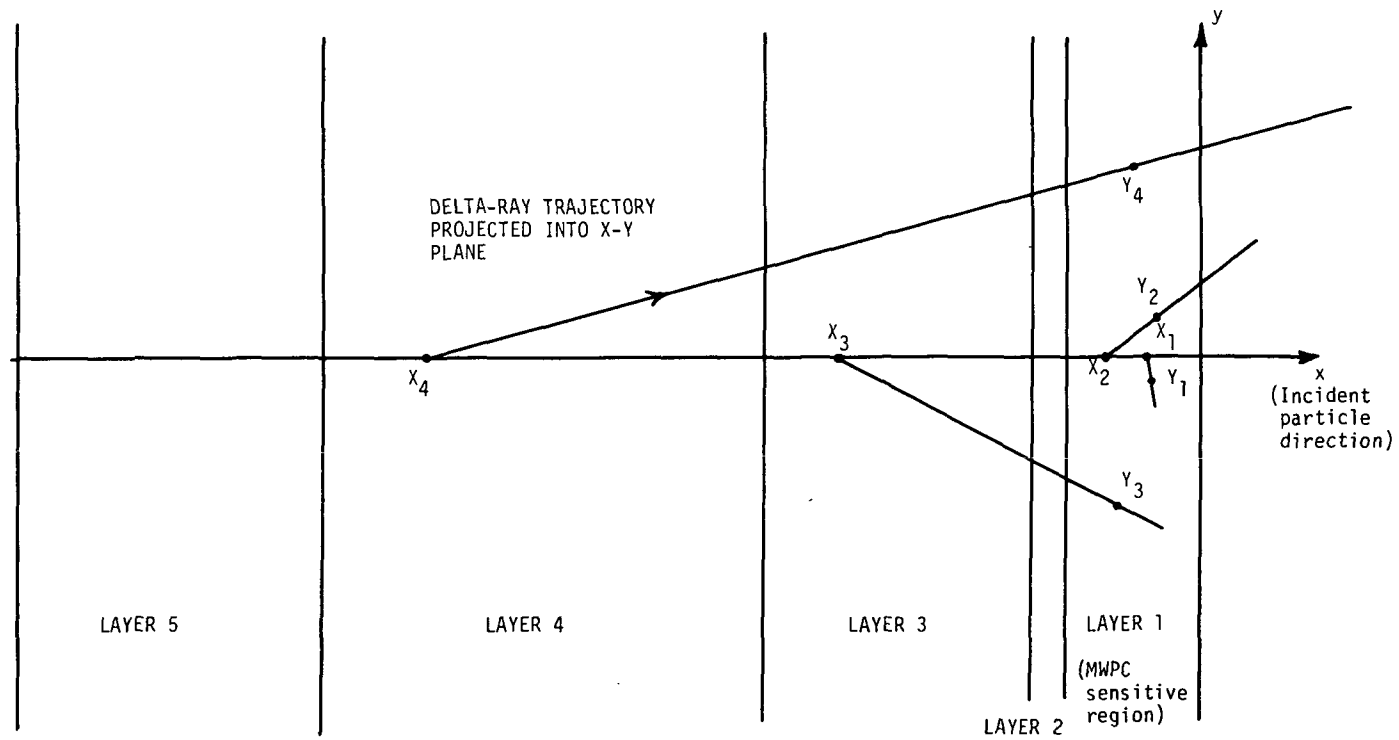

FIGURE 8-1. Geometry for delta-ray computer program

TABLE VIII-1. BASIC FORMULAE FOR DELTA-RAY PRODUCTION

Definition of Symbols

- E : Incident particle kinetic energy per nucleon.
- z : Incident particle charge.
- β : Incident particle velocity/velocity of light.
- γ : Incident particle total energy/rest mass.
- M : Atomic mass unit (= 931.16 MeV).
- m : Electron mass (= .511 MeV).
- Z : Absorber atomic number.
- A : Absorber atomic weight.
- I : Absorber mean ionization potential.
- ω : Delta-ray kinetic energy.
- W : Maximum delta-ray kinetic energy ($=2m\beta^2\gamma^2$.)
- ω_o : Minimum delta-ray kinetic energy.
- Θ : Angle of delta-ray emission with respect to incident particle direction.
- R : Delta-ray empirical range (g/cm^2)

The probability that a heavy (mass >>m) charged incident particle will produce a delta-ray within the energy interval of ω to $\omega + d\omega$ while traversing one $gram/cm^2$ of absorber is:

$$\frac{d^2n}{dxd\omega} = \frac{\cdot 15353 z^2 Z}{\beta^2 A} \left(1 - \beta^2 \frac{\omega}{W} \right) \frac{1}{\omega^2} \qquad (8\text{-}1)$$

The number of delta-rays with energy > ω_o per g/cm^2 is:

$$\left.\frac{dn}{dx}\right\}_{\omega_o} = \frac{\cdot 15353 z^2 Z}{\beta^2 A \omega_o} \left\{ 1 - \frac{\omega_o}{W} + \beta^2 \frac{\omega_o}{W} \ln \left(\frac{\omega_o}{W}\right) \right\} \qquad (8\text{-}2)$$

The ionization energy loss per g/cm^2 due to collisions that produce delta-rays with energies < ω_o is:

$$\left.\frac{dE}{dx}\right\}_{\omega_o} = \frac{\cdot 15353 z^2 Z}{\beta^2 A} \left\{ \ln \left(\frac{W\omega_o}{I^2} \right) - \beta^2 \right\} \qquad (8\text{-}3)$$

The usual additional term for the density effect is neglected here because it is very small for practically all cases of interest.

TABLE VIII-1 (Continued)

The relationship between the production angle and energy for delta-rays is

$$\cos \Theta = \frac{1}{\beta} \{\omega/(\omega + 2m)\}^{1/2} \qquad (8\text{-}4)$$

The following empirical range-energy relationships are used for delta-rays (low energy electrons).

$$R = \begin{cases} .412\omega^{(1.265 - .0954 \ln \omega)}, & \omega < 3\text{MeV} \\ .526\omega - .106, & \omega \geq 3\text{MeV} \end{cases} \qquad (8\text{-}5)$$

basis. The spatial distribution of the energy deposited in the form of ionization in the MWPC sensitive region by delta-rays produced in all layers is calculated for each event and various distributions are accumulated in the form of histograms for a specified number of incident particles (events).

The production of delta-rays by each incident particle is treated by starting with the incident particle at one boundary of the combination of materials. The delta-ray production coefficient (eqn. 8-2) is calculated and the distance to the first collision which produces a delta-ray with energy above ω_o is randomly generated from the corresponding exponential distribution. If this distance is beyond the boundary for the layer in question, the process is reinitiated at the boundary of the next layer. Next, the delta-ray energy, ω, is randomly generated from a ω^{-2} distribution which is a simplifying approximation to the actual energy distribution (eqn. 8-1). In turn, the angle of emission is calculated from eqn. 8-4, the range of the delta-ray is calculated from eqn. 8-5, and the projected range is checked to see if the delta-ray is able to penetrate to the first layer. If the delta-ray stops before reaching the first layer, it is neglected and the calculation starts again with generation of the point of the next delta-ray production. If the delta-ray can penetrate the first layer, the azimuth angle of emission is randomly generated from a uniform distribution and the trajectory is projected into the x-y plane to determine the y-coordinate at entry into the first region. The range-energy relationships (eqn. 8-5) and the corresponding inverse energy-range relationships are used to determine the energy at entrance. The delta-ray is further propogated along a straight-line until it exists the first region or stops. The y-coordinate and energy at exit or the y-coordinate of the stopping point are calculated. The energy deposition in the first region is the difference between the entrance and exit energies and the lateral position of the energy deposition is approximated by the y-coordinate of the mid-point of the delta-ray trajectory in the first layer. This sequence is repeated until the incident particle has passed through the entire combination of materials. The several possibilities depending upon whether the delta-ray was produced in the first layer or prior to the first layer and whether

the delta-ray stops in the first layer or exists the first layer are graphically depicted in Figure 8-1. All lateral positions are projected into one plane because this is the quantity measured by the MWPC systems with which we are dealing.

The ionization energy loss in the first layer due to incident particle collisions in which the energy transferred to the secondary electron is less than ω_o (so called soft collisions) is calculated according to eqn. 8-3. This energy deposit is treated as if it is concentrated along the incident particle trajectory (i.e., y = 0). The MWPC is assumed to respond linearly to the ionization produced by delta-rays and the MWPC gain nonlinearity is approximated by assuming that the MWPC response to the soft-collision ionization is proportional to the square-root of the energy deposited, in correspondence with our experimental results (see Section 9).

For each incident particle, the lateral centroid of the energy deposition in the first layer by delta-rays produced in each of the layers and for the energy deposition from all layers is calculated. This distribution of lateral centroids of energy deposition is the primary result of the computer simulation because it represents the distribution of position measurements which a true centroid-sensitive MWPC system would produce. In addition, the lateral distributions of energy deposition in the first layer due only to delta-rays produced in each of the layers, and the distributions of the fraction of the total energy loss in the first layer due to delta rays produced in each of the layers are also generated. These distributions are mainly useful for diagnostic purposes and for checking the relative importance of the individual layers.

8.3 Results of the Computer Simulation

The computer program described above was run for the following simple configuration: a 1-cm. thick layer of Argon (the MWPC sensitive region) preceded by a 0.001-in thick Mylar layer (the MWPC window) and a 1-m. thick layer of air. One-thousand event runs for incident particles with E = 2.1 GeV/nucleon and z = 4, 8, 12, 16, 20 and 26 were performed. A summary of the results is contained in Table VIII-2 and representative distributions generated are shown in Figures 8-2 through 8-5.

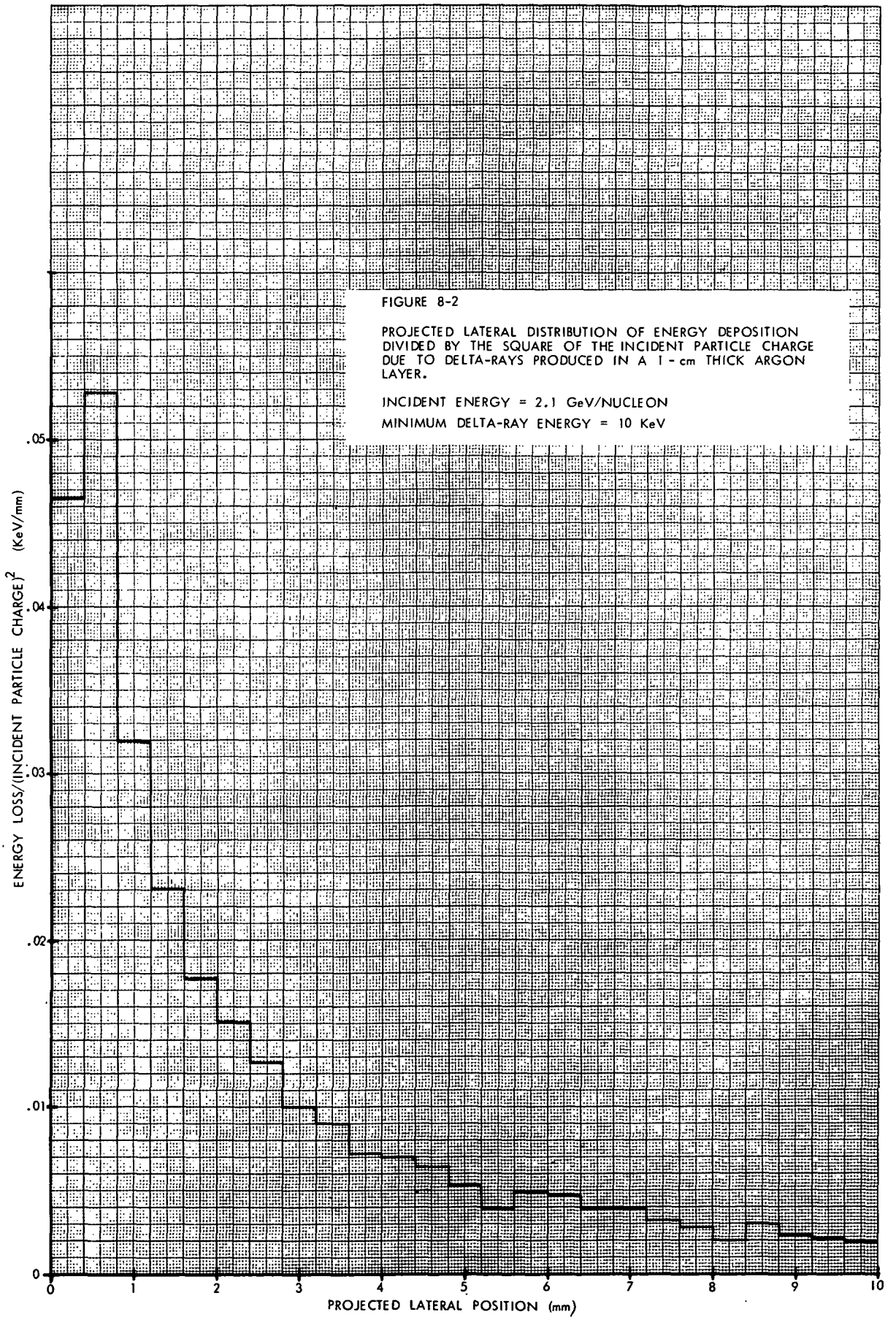

FIGURE 8-2

PROJECTED LATERAL DISTRIBUTION OF ENERGY DEPOSITION DIVIDED BY THE SQUARE OF THE INCIDENT PARTICLE CHARGE DUE TO DELTA-RAYS PRODUCED IN A 1 - cm THICK ARGON LAYER.

INCIDENT ENERGY = 2.1 GeV/NUCLEON

MINIMUM DELTA-RAY ENERGY = 10 KeV

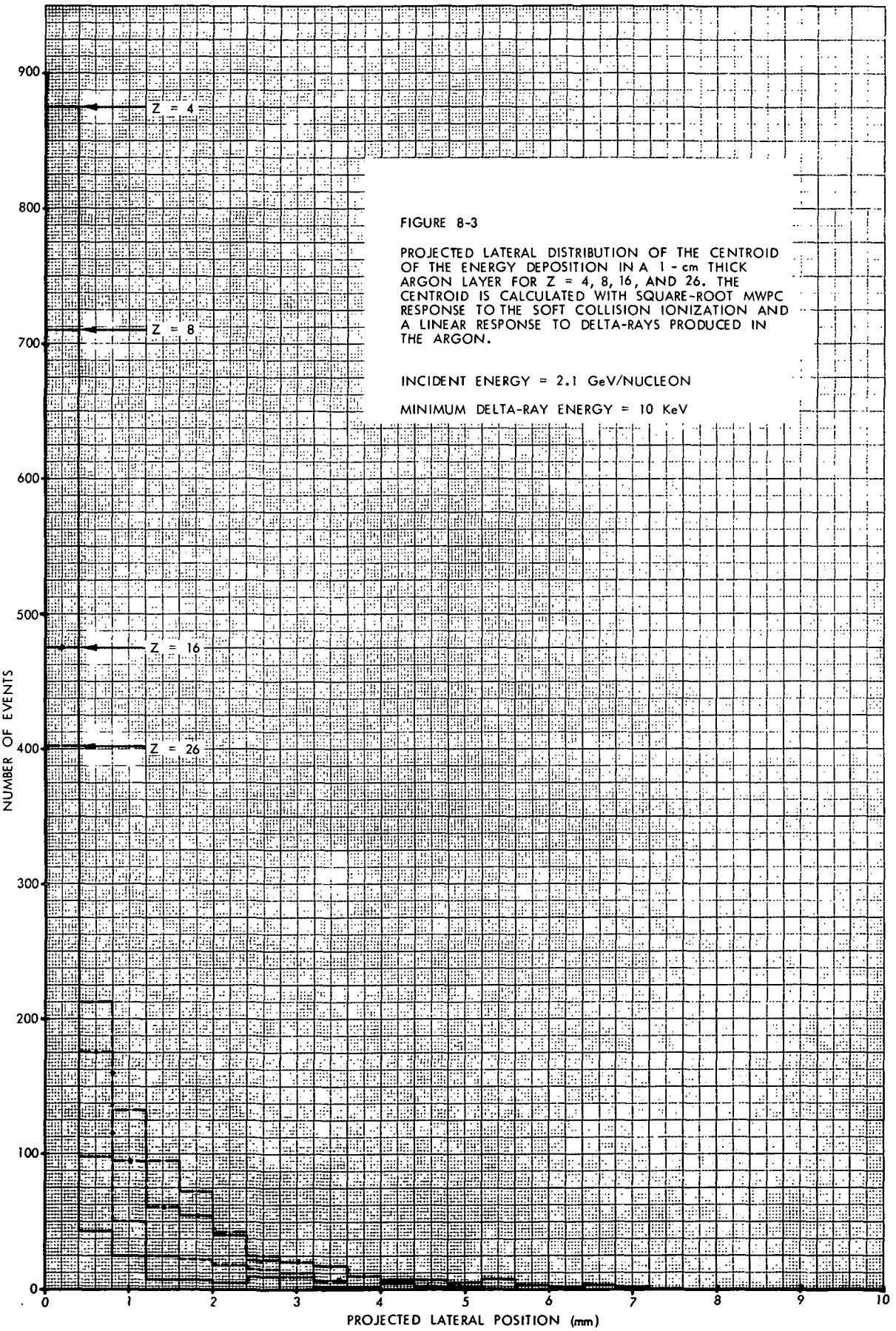

FIGURE 8-3

PROJECTED LATERAL DISTRIBUTION OF THE CENTROID OF THE ENERGY DEPOSITION IN A 1 - cm THICK ARGON LAYER FOR Z = 4, 8, 16, AND 26. THE CENTROID IS CALCULATED WITH SQUARE-ROOT MWPC RESPONSE TO THE SOFT COLLISION IONIZATION AND A LINEAR RESPONSE TO DELTA-RAYS PRODUCED IN THE ARGON.

INCIDENT ENERGY = 2.1 GeV/NUCLEON

MINIMUM DELTA-RAY ENERGY = 10 KeV

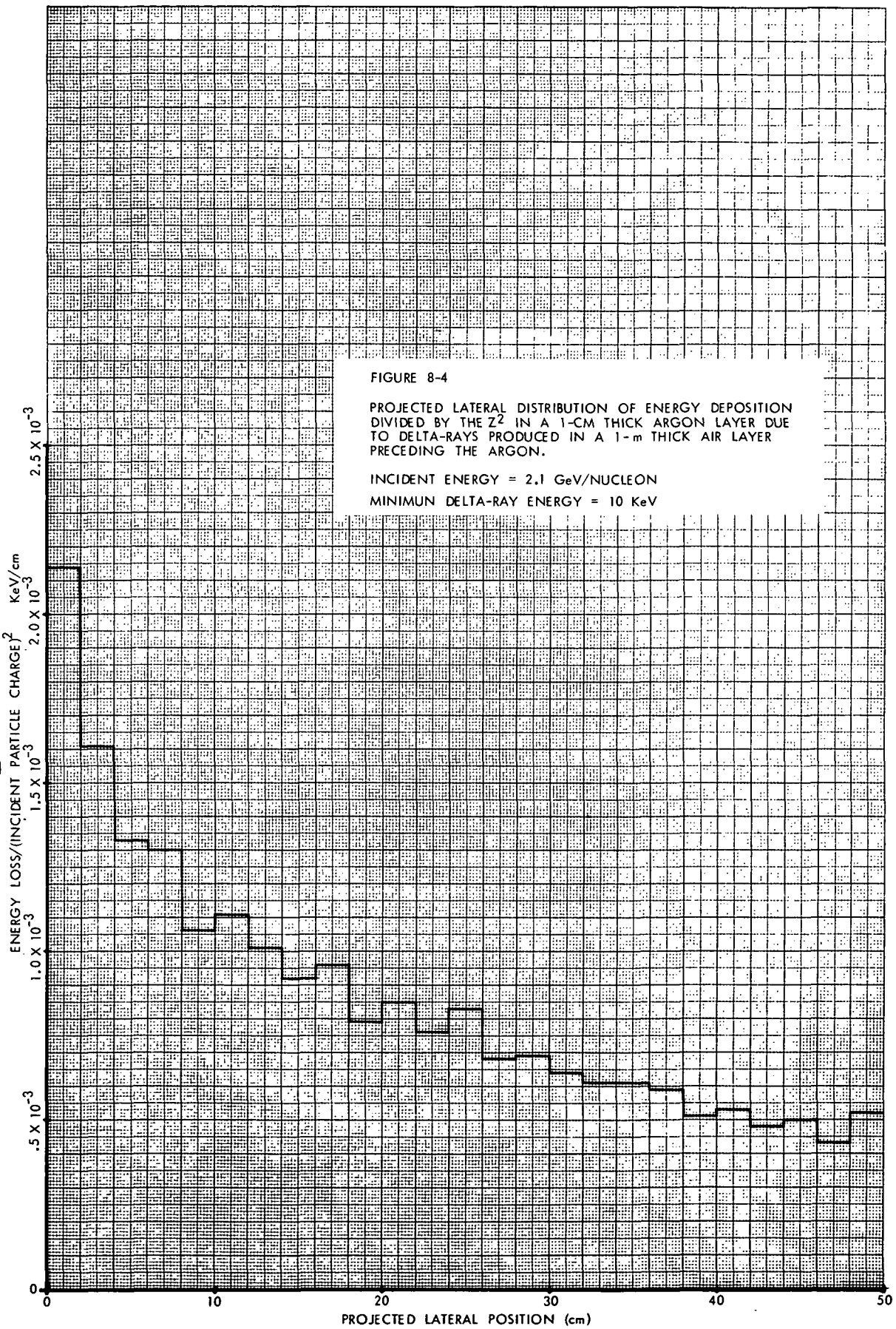

FIGURE 8-4

PROJECTED LATERAL DISTRIBUTION OF ENERGY DEPOSITION DIVIDED BY THE Z^2 IN A 1-CM THICK ARGON LAYER DUE TO DELTA-RAYS PRODUCED IN A 1-m THICK AIR LAYER PRECEDING THE ARGON.

INCIDENT ENERGY = 2.1 GeV/NUCLEON

MINIMUN DELTA-RAY ENERGY = 10 KeV

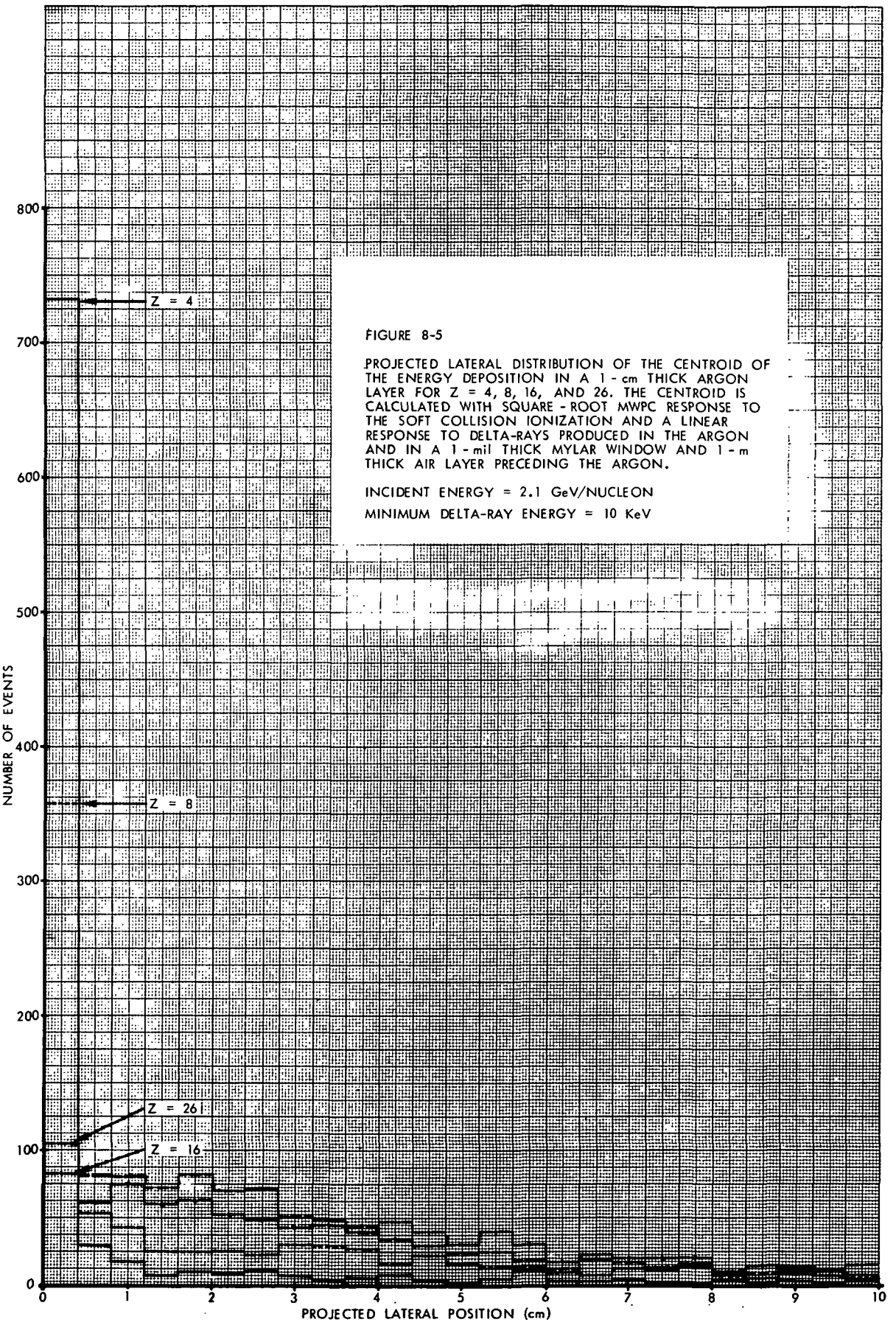

FIGURE 8-5

PROJECTED LATERAL DISTRIBUTION OF THE CENTROID OF THE ENERGY DEPOSITION IN A 1 - cm THICK ARGON LAYER FOR Z = 4, 8, 16, AND 26. THE CENTROID IS CALCULATED WITH SQUARE - ROOT MWPC RESPONSE TO THE SOFT COLLISION IONIZATION AND A LINEAR RESPONSE TO DELTA-RAYS PRODUCED IN THE ARGON AND IN A 1 - mil THICK MYLAR WINDOW AND 1 - m THICK AIR LAYER PRECEDING THE ARGON.

INCIDENT ENERGY = 2.1 GeV/NUCLEON

MINIMUM DELTA-RAY ENERGY = 10 KeV

The figures showing the projected lateral distributions of the energy deposition in the MWPC sensitive region (layer 1) due to delta-rays produced in layer 1 and layer 3 (the 1-m air layer preceding the MWPC) are valid for all incident charges. For any value of incident charge, z, the ordinate should be multiplied by z^2. No distribution is given for layer 2 (the Mylar window) because its contribution was negligible in all cases. In order to get a feel for the contribution to the total energy deposition due to delta-rays relative to the energy deposition due to soft collisions, it should be noted that the energy deposition due to soft collisions (energy transfers < ω_o = 10 KeV) divided by z^2 is equal to 1.87 KeV. Delta-rays with an energy < 10 KeV are emitted at angles > 80 degrees and have a range < 1mm in Argon. Therefore, the energy deposition due to soft collisions is contained in a column of radius < 1mm and has a mean projected lateral energy deposition density divided by z^2 equal to .935 KeV/mm, or about 20 times the maximum density due to delta-rays. Although the lateral energy deposition density due to delta-rays is much lower than that due to soft collisions, the delta-ray contribution is spread over very large lateral distances. This is especially true of the contribution from the 1-m air layer as would be expected from the geometry of the problem. When we consider the lateral distribution of the centroid of the energy deposition, we see that the delta-rays from the air layer produce a long tail on the lateral distributions. Our treatment of the non linearity of the MWPC response produces an accentuation of the delta-ray effects because while the delta-ray contributions are increasing as z^2 as z increases, the soft collision contribution is only increasing as z. However, even if the MWPC responded linearly the delta-rays will produce a position measurement distribution which is definitely not Gaussian. This can be seen by comparing the rms and 68% widths for low z in Table VIII-2. If the distributions were Gaussian the two widths would be equal. The fact that 68% widths are smaller than rms widths reflects the fact that the distributions have a central spike with very broad, low-level tails. The fact that the widths of the centroid distributions level-off or even decrease as z increases above 12 to 16 comes about because the delta-ray production is becoming frequent enough that statistical fluctuations are starting to average out in the centroid.

TABLE VIII-2

Configuration Definition

Layer	Material	Density (g/cc)	Thickness (cm)
1	Argon	1.784×10^{-3}	1.0
2	Mylar	1.18	2.54×10^{-3}
3	Air	1.205×10^{-3}	100.0

Incident Particle Definition

Energy = 2100 MeV/nucleon

Maximum delta-ray energy = 9.81 MeV

Minimum delta-ray energy = 0.01 MeV

	Units	Charge 4	8	12	16	20	26
Mean soft collision energy deposited in layer 1	KeV	29.9	119.6	269.1	478.4	748	1263
Mean energy deposited in layer 1 by delta-rays produced in:	KeV						
layer 1		4.2	15.3	36.9	59.1	95.1	161.8
layer 3		1.9	7.1	16.3	29.2	45.0	78.0
Mean total energy deposited in layer 1	KeV	36.0	142.0	322.3	566.7	888	1503
Widths of projected lateral distribution of energy deposition in layer 1 by delta-rays produced in:							
layer 1 - rms	cm	.44	.45	.43	.44	.43	.43
- 68%*		.34	.28	.32	.31	.28	.30
layer 3 - rms		41.7	42.9	42.0	42.8	43.1	43.5
- 68%*		40	42	42	42	42	42
Widths of projected lateral distribution of the centroid of energy deposition in layer 1 including delta-rays produced in:							
layer 1 - rms	cm	.12	.15	.15	.15	.13	.11
only - 68%*		<.02	.04	.08	.09	.10	.10
all layers - rms		8.63	9.69	7.17	6.66	5.38	4.53
- 68%*		<.2	5.0	5.3	5.4	4.4	3.9

* 68% width = y such that $\int_{-y}^{+y}$ contains 68% of the events.

As previously noted, the effects due to delta-rays produced in materials such as the air layer preceding the MWPC may be greatly reduced by the presence of a magnetic field component perpendicular to the incident direction which prevents delta-rays from moving very far in the incident particle direction. Also many of the delta-rays produced in the air layer penetrate the MWPC at distances which are far enough from the point at which the incident particle traverses the MWPC to produce separated pulses on the delay line. In this case of separated pulses, it is possible that the effects of the delta rays could be electronically minimized. However, even if we limit ourselves to the effects of the delta-rays produced in the MWPC gas itself, the delta-rays produce a rms position uncertainty of about 1 to 1.5 mm for a 1 cm thick sensitive region. If we consider the 68% width as a better indication of the spacial resolution, we see that the delta-ray effects are essentially the order of or less than other limits discussed in the section on the spacial resolution for $z \leq 4$, and rise to about 1 mm for $z = 26$.

8.4 Energy Loss Calculations for Gas Mixtures

In order to calculate dE/dX for the mixture we need the mean ionization potential and Z/A of the mixture. If the fraction by weight of each element in the mixture is denoted by f_i

$$\left.\frac{Z}{A}\right\}_{mix} = \sum_i f_i \left(\frac{Z}{A}\right)_i$$

$$\left. \ln I \right\}_{mix} = \sum_i f_i \left(\frac{Z}{A}\right)_i \ln I_i \Big/ \sum_i f_i \left(\frac{Z}{A}\right)_i$$

With I_{mix}, the dE/dX is determined by looking up the stopping power for I_{mix} of a proton with equal velocity in Barkas & Berger[24], Table I and multiplying by $\left.\frac{Z}{A}\right\}_{mix}$.

For nuclei with 2.1 GeV/nucleon kinetic energy the equivalent (i.e. equal velocity) proton energy is 2.12 GeV.

We have worked with the following mixtures:

Mix	Constituent Ar_2	CO_2	C_4H_{10}	X_e	
1	0.94	0.06	-	-	
2	0.90	0.10	-	-	
3	0.80	0.20	-	-	(fraction by volume)
4	0.90	-	0.10	-	
5	0.75	-	0.25	-	
6	0.81	0.05	-	0.14	

The four gases in the mixture have the following properties

		Ar	CO_2	C_4H_{10}	Xe
Density	(mg/cc)	1.784	1.977	2.673	4.587
Molecular Wgt.	(g)	39.95	44.01	58.12	131.30

The mixtures have the following properties:

Mix	Constituent	Ar	CO_2	C_4H_{10}	Xe	Density of Mix (mg/cc)
1	Partial Density	1.677	.119	-	-	1.796
	(Fraction by Weight)	(.934)	(.066)			
2		1.606	.198	-	-	1.804
		(.890)	(.110)			
3		1.428	.385	-	-	1.813
		(.786)	(.214)			
4		1.606	-	.267	-	1.873
		(.857)		(.143)		
5		1.339	-	.668	-	2.007
		(.665)		(.335)		
6		1.440	.103	-	.643	2.186
		(.659)	(.047)		(.294)	

Finally we have for the mixtures in terms of fractional weights by elements:

Element	H	C	O	Ar	Xe
Mix					
1	-	.018	.048	.934	-
2	-	.030	.080	.890	-
3	-	.058	.156	.786	-
4	.025	.118	-	.857	-
5	.058	.277	-	.665	-
6	-	.013	.034	.659	.294
Z/A	1.0	.5	.5	.451	.411
I (eV)	19	78	103	210	555

The results of the equations above are:

Mix	Z/A_{mix}	I_{mix}	Stopping power	$\frac{dE}{dX}$ ($\frac{MeV}{g/cm^2}$)
1	.454	199	3.357	1.521
2	.457	188	3.373	1.540
3	.462	175	3.400	1.568
4	.471	161	3.432	1.614
5	.497	119	3.530	1.752
6	.442	288	3.235	1.430

These are mean loss rates. A correction needs to be applied for escaping delta-rays and entering delta rays from materials preceding the MWPC.

For pure Argon $\frac{dE}{dX} = 1.505$ MeV/g/cm^2

and hence ΔE in 1 cm = 2.68 KeV

The delta-ray calculations gave an energy loss $/Z^2 = 2.23$ KeV

Therefore our best estimate of energy deposited is .832 of mean dE/dX.

To calculate the no. of ion pairs produced in the MWPC gas we also need to know the mean energy required to produce an ion pair. The values in the summary table below were calculated following Hurst et al[25]:

Gas Mixture	94% Ar 6% CO_2	90% Ar 10% CO_2	80% Ar 20% CO_2	90% Ar 10% C_4H_{10}	75% Ar 25% C_4H_{10}	81% Ar 14% Xe 5% CO_2
Density (mg/cc)	1.796	1.804	1.813	1.873	2.007	2.186
Mean dE/dX (MeV/ g/cm^2) for Z=1, β = .952	1.521	1.540	1.568	1.614	1.752	1.430
Energy Deposition Rate (MeV/ g/cm^2) dE/dX .0.832	1.265	1.280	1.302	1.341	1.458	1.189
Energy Deposited per cm @ STP (KeV/cm)	2.27	2.31	2.36	2.52	2.93	2.60
Mean energy to form an ion pair (eV)	26.2	26.4	27.2	24.3	25.4	24.0
Ion pairs per cm (cm^{-1}) for Z=1, β = .952	87	88	87	104	115	108

9. BEVATRON MEASUREMENTS AND RESULTS

A series of measurements was carried out with several of our standard MWPC's in a relativistic heavy ion beam at the Bevatron. Two heavy ion beams were available at the Bevatron:

2.1 GeV/nucleon C^{12}

and

2.1 GeV/nucleon O^{16}

The purpose of our measurements was to measure the gas gain curves for C^{12} and O^{16} nuclei in various gases for comparison with the gas gain curves obtained with Fe-55 x-rays. We also wanted to study the pulse shapes of the MWPC current pulses, charge pulses and delay-line pulses as a function of the MWPC gas and supply voltage.

The experimental setup contained 4 chambers as shown in Figure 9-1. The chambers were mounted on a common base plate with electrical and gas feed throughs. The base plate itself was mounted to a turn-table. A hood made out of aluminum foil was placed over the setup to act as an RF-shield.

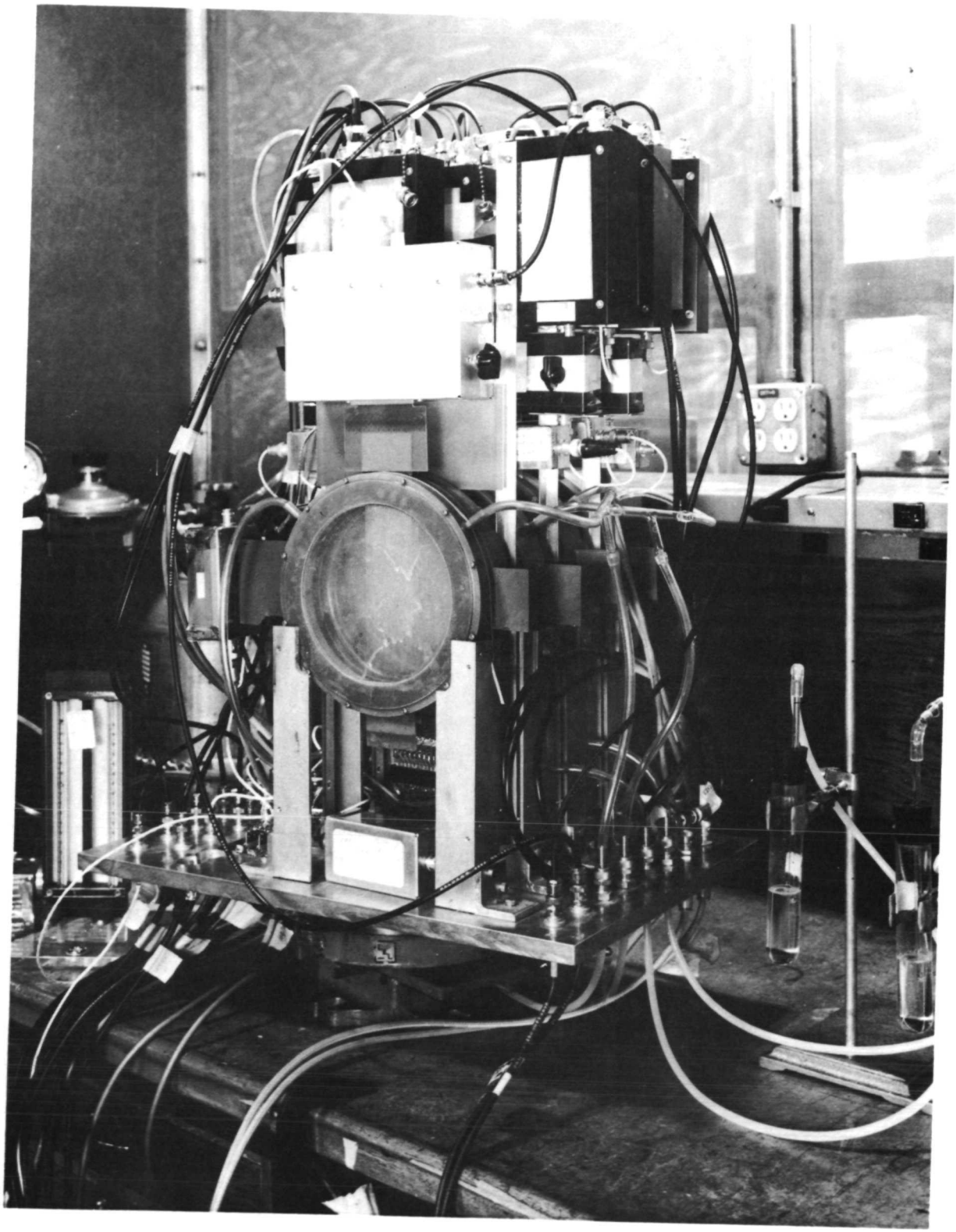

FIGURE 9-1. Experimental setup for Bevatron measurements

Three of the chambers (chambers No. 2, 3, and 4 in Figure 9-1) were outfitted with a capacitively coupled, bulk delay line of the Perez-Mendez type and chamber No. 1 was connected to a directly coupled, lumped element delay-line described in Section 6. The anodes of chamber 2, 3 and 4 were connected to Ortec 109-PC charge sensitive amplifiers. The cathode of each of the chambers 2, 3 and 4 which was not coupled to the bulk delay-line was connected to a fast current amplifier. A current amplifier was also connected to the anode wires of chamber No. 1. Figure 9-2 shows the block diagram of the experimental setup. A coincidence telescope, which consisted of two 1 cm x 1 cm plastic scintillators, defined the particle beam and was used to trigger the oscilloscope camera and to gate the pulse height analyzer.

The gas gain was measured in three different gases,

80% Ar + 20% CO_2
75% Ar + 25% Isobutane (C_4H_{10})
81% Ar + 14% Xe + 5% CO_2 (for C^{12} - runs only)

with C^{12} and O^{16} nuclei and Fe-55 x-rays.

The pulse shapes of the current pulses, delay-line pulses and charge pulses as a function of HV were photographed for C^{12} and O^{16} nuclei in 80% Ar + 20% CO_2 and 75% Ar + 25% Isobutane, and for C^{12} nuclei only in 81% Ar + 14% Xe + 5% CO_2.

The results of the gas gain measurements are plotted in Figure 9-3 for C^{12} and in Figure 9-4 for O^{16}. The ordinate of these two figures is the number of electrons collected at the MWPC anode as measured with the amplifier system using 1 μsec shaping time constants. These data can be converted to relative* gas gain by dividing the number of electrons collected by the number of primary electron-ion pairs produced in the MWPC sensitive region (see Section 8.4). In Figure 9-5, we show the relative gas gain for Fe-55, C^{12}, and O^{16} in 80% Argon and 20% CO_2. We see, as can be expected from our considerations of space charge effects in Section 4.4, that the onset of deviation from strict proportionality occurs at lower gas gains with increasing primary ionization densities. The

*Recall that, as discussed in Section 3, an additional correction for the fraction of the total charge collected in the ~ 1 μsec time constant of the amplifier would have to be made to obtain absolute gas gains.

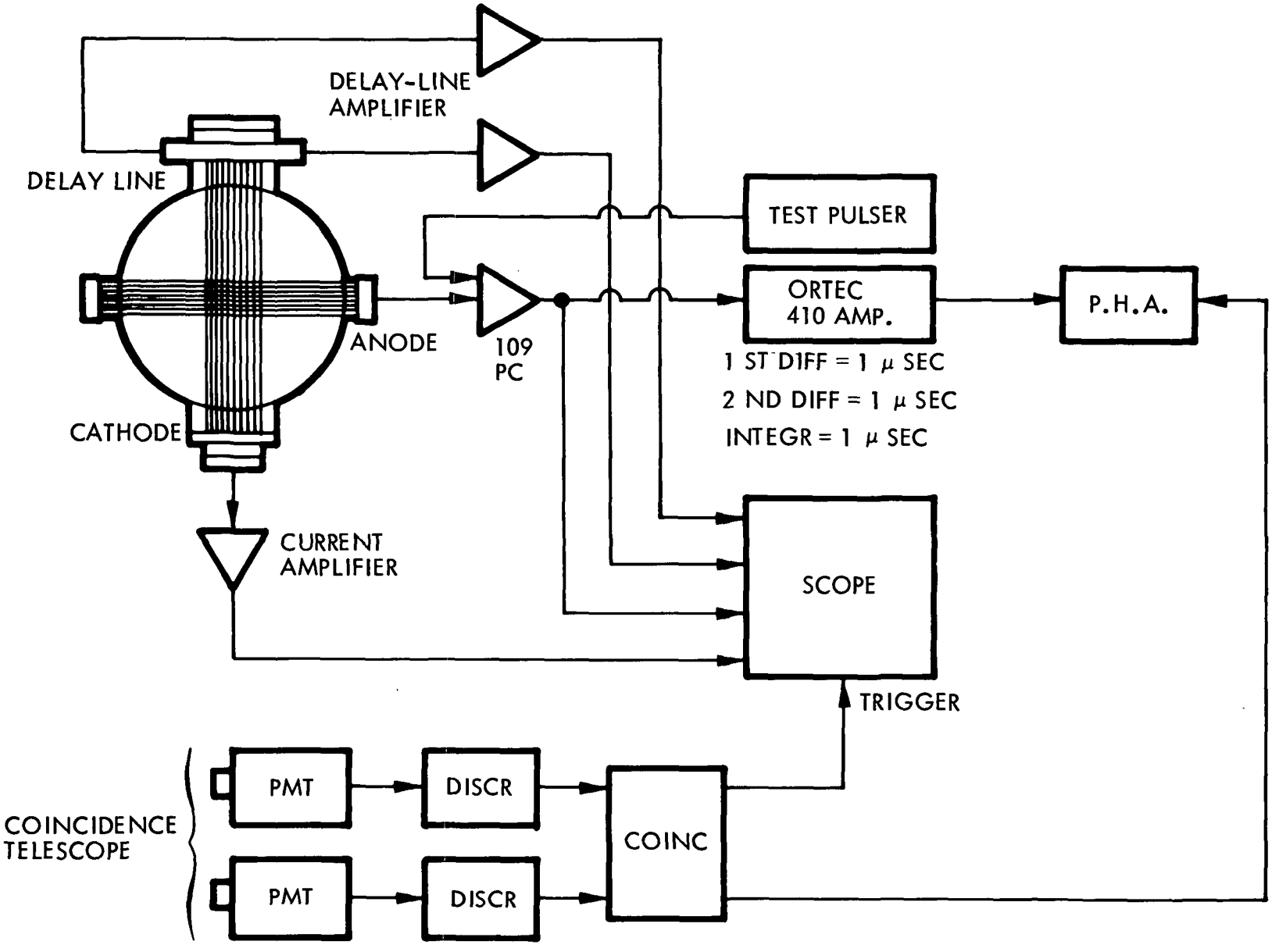

FIGURE 9-2. Block diagram of Bevatron experimental setup

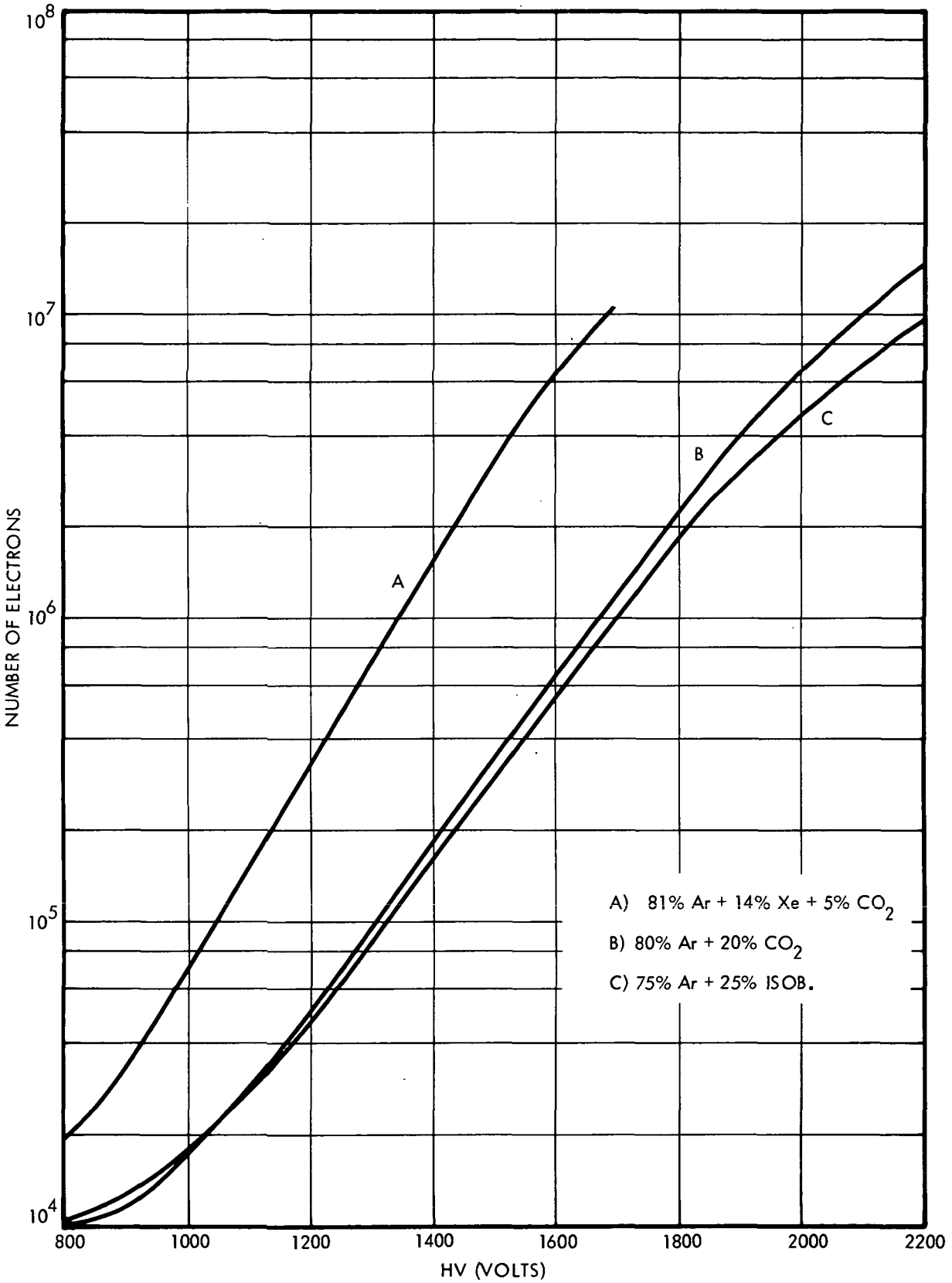

FIGURE 9-3. Gas gain for 2.1 GeV/nucleon C^{12}-nuclei

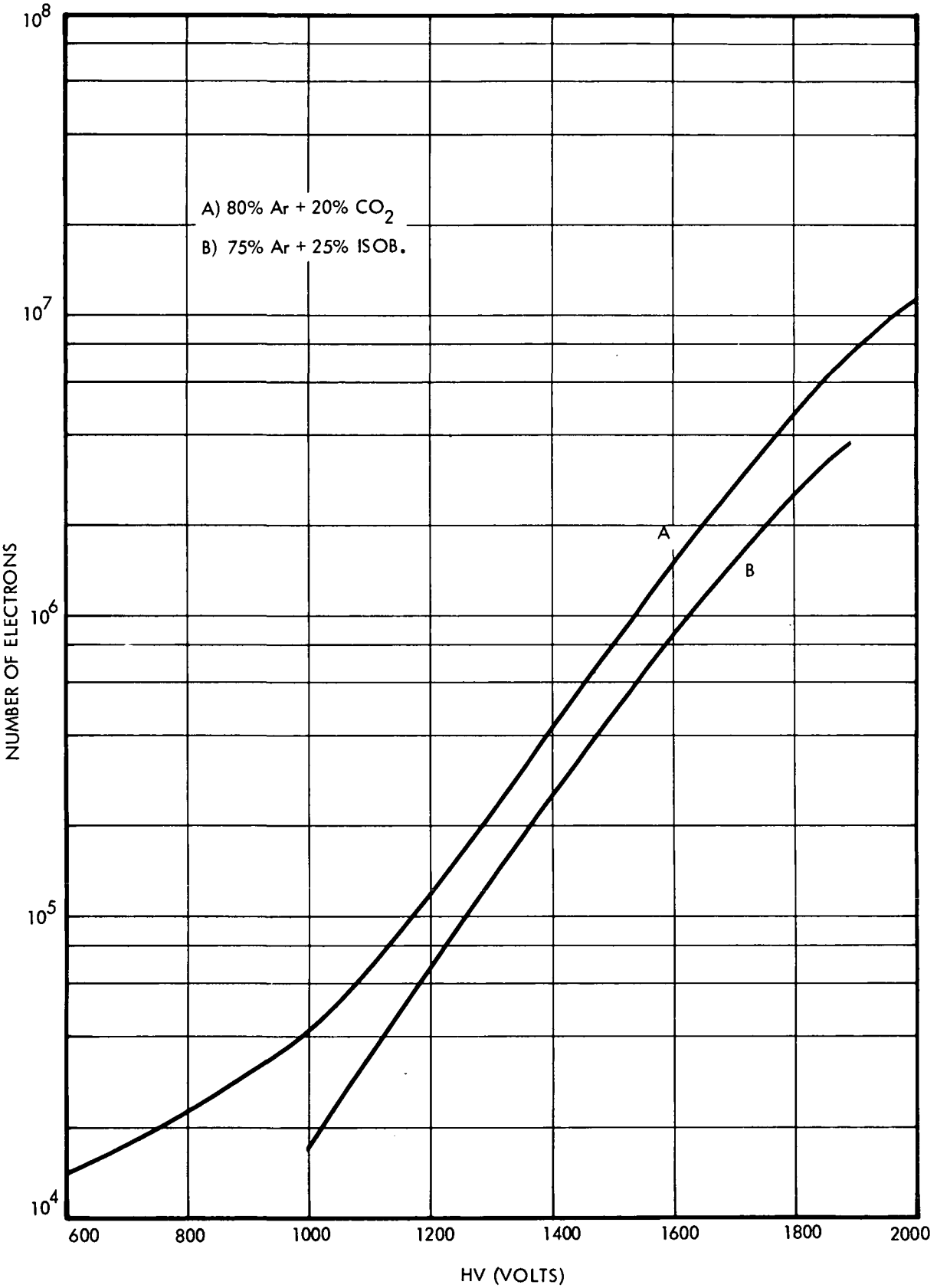

Figure 9-4. Gas gain for 2.1 GeV/nucleon O^{16}-nuclei

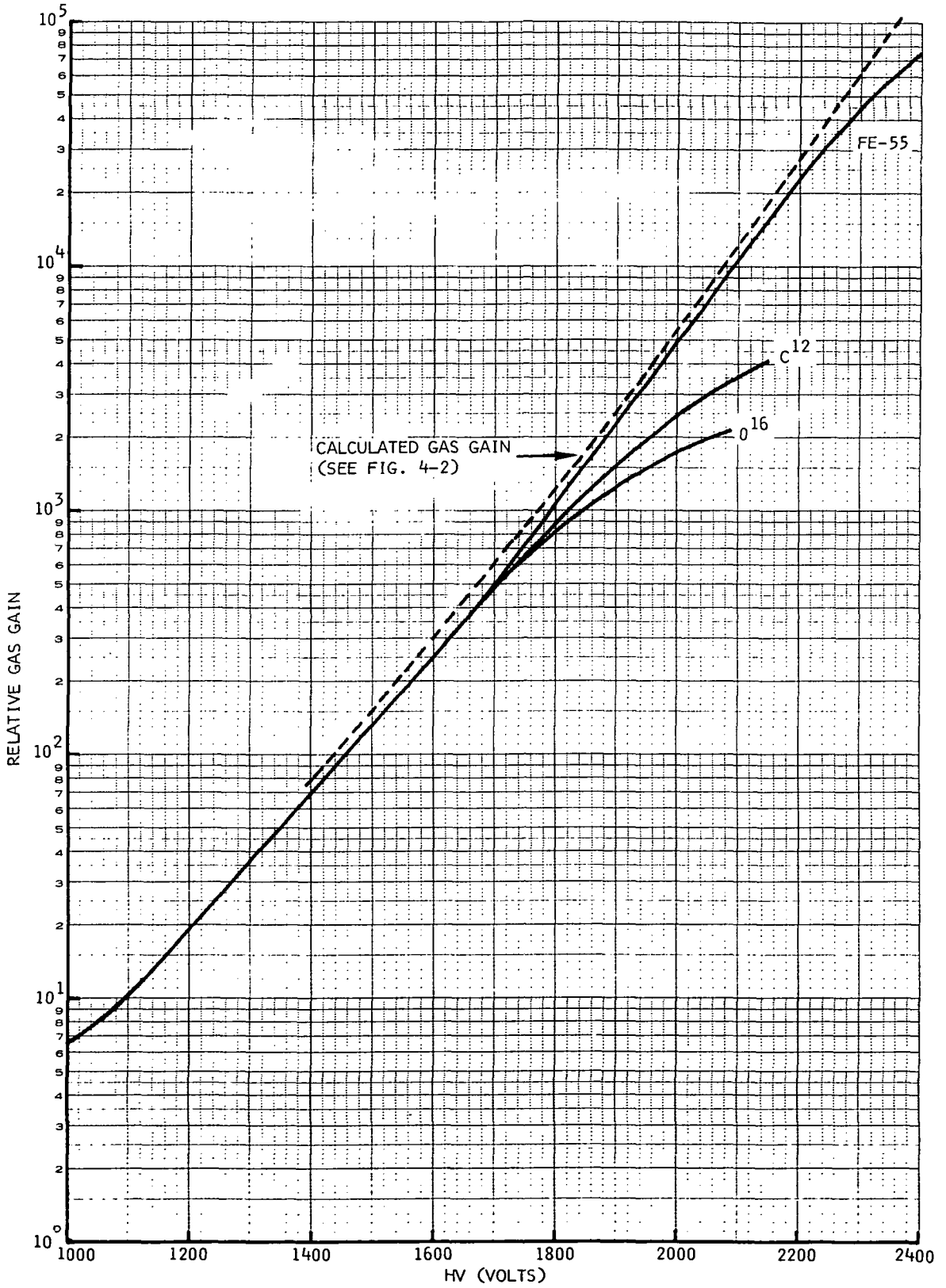

FIGURE 9-5. Comparison of gas gain of Fe-55 x-rays and C^{12} and O^{16} nuclei in 80% Ar + 20% CO_2

magnitude of the reduction in gain was proportional to the total charge in the signal. At a given high voltage, the charge in the signal is proportional to the primary ionization, and hence the reduction in gain is an increasing function of the primary ionization density. We also see that the relative reduction in gain increases as the voltage increases, again as expected, since the amount of charge in the signal increases with increasing voltage.

Another way of looking at the saturation characteristics of our chambers is to plot the measured number of electrons for Fe-55, C^{12} and O^{16} for the three gases as a function of the energy loss in the chamber gap. This was done in Figure 9-6 on log-log paper. The energy loss is expressed in terms of the energy loss of a minimum ionizing particle and is corrected for delta-ray effects. (see Section 8.4). Strict proportionality would be represented by a slope of + 1 in this plot. The effect of saturation is to reduce the slope of the lnN vs $\ln\Delta E$ plot. In Figure 9-7 we have plotted the slopes from Figure 9-6 as a function of the number of electrons collected for a minimum ionizing (z = 1) particle. The increasing saturation with increasing gain shows very clearly and is seen to be approximately equal for the various gases. We have already noted that this deviation from proportionality will accentuate the detrimental effects of delta-rays on spatial resolution. It is, therefore, desirable to operate MWPC's at the lowest possible gain that still affords enough signal to achieve the required spatial resolution for the least ionizing particles of interest. We have seen in Section 6.5 that a signal of approximately 2×10^6 electrons is required for a spatial resolution approaching 100 μm with the lumped element delay line. If we require that signal for minimum ionizing particles, we see from Figure 9-7 that the MWPC response as a function of primary energy deposition in the MWPC will be approximately $\Delta E^{1/2}$ (i.e. slope $\simeq$ 0.5). This square-root MWPC response was what we used in the analysis of the delta-ray problem in Section 8.

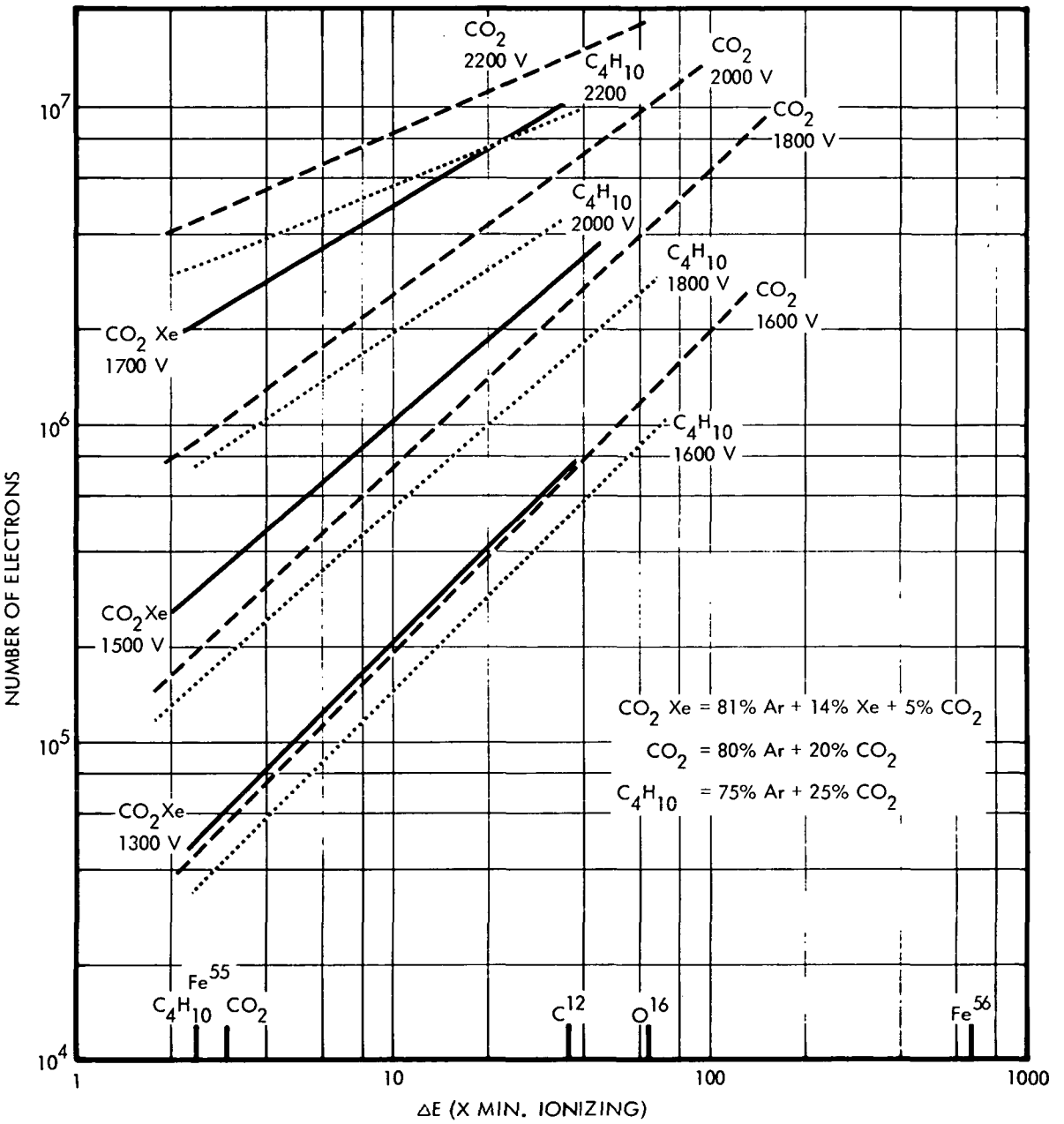

FIGURE 9-6. Measured number of electrons v.s. energy loss of Fe-55 x-rays and C^{12}- and O^{16}-nuclei in three different gases as a function of HV.

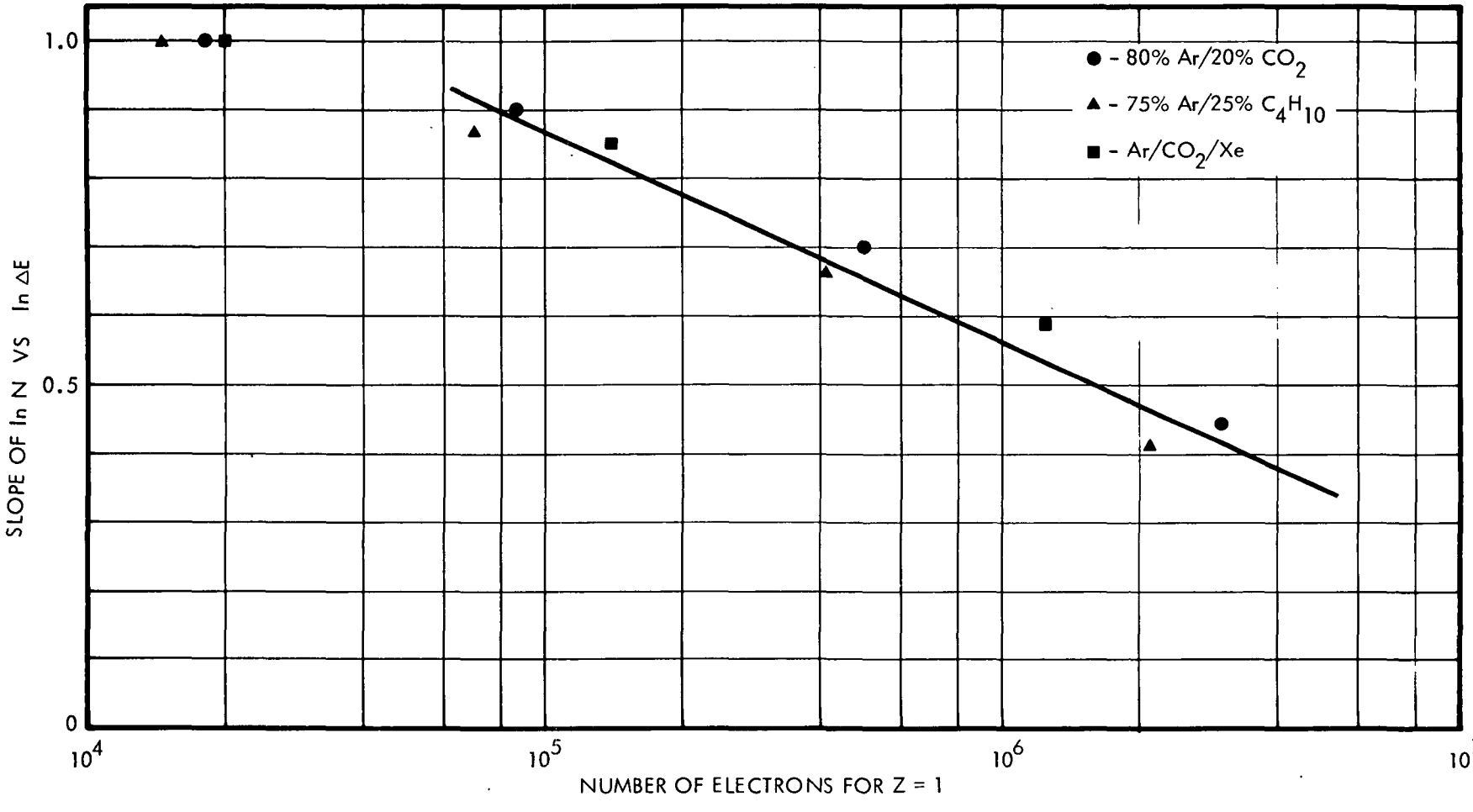

FIGURE 9-7. Saturation characteristics for minimum ionizing Z=1 particles

In Section 2 we noted that the desired range of incident charge for cosmic ray spatial detectors is commonly $1 \leq z \leq 26$. Our Bevatron measurements obviously do not answer the question of whether the response observed for $1 \leq z \leq 8$ can be extrapolated to $z = 26$. Recall that in Section 4.5 we found that the space charge saturation limit on the signal charge density was about 10^9 electrons/cm (i.e., about 0.5 esu/cm) for our MWPC electrode geometry with operating voltages of about 2200V. Since we expect the effective width of the discharge along the anode to be the order of 0.1 cm, we should reach space charge saturation at about 10^8 electrons. We can see that all of the curves in Figure 9-6 extrapolate to less than 10^8 electrons for a ΔE value corresponding to $z = 26$, and hence such an extrapolation at least does not violate the space charge saturation limit.

10. MWPC - DESIGN CONSIDERATIONS

In Section 2 we discussed some of the requirements for a typical spatial detector system for a high energy cosmic ray experiment, which in this case was the superconducting magnetic spectrometer experiment on HEAO-B. One of the important requirements for the MWPC frame in that experiment was the minimum septum width of the frame along the wall of the cryostat. The frame material had to be non-magnetic and had to exhibit low outgasing.

The minimum septum width for a given frame material is dependent on the frame load due to the tensioning of the anode and cathode wires. To calculate the frame load due to the anode wire tensioning one has to consider the electrostatic problems in MWPC's, i.e. the electrostatic stability of the anode wires. The minimum tension, t_c, required to keep the anode wires in equilibrium is

$$t_c = \frac{q^2 l^2}{s^2} \tag{10-1}$$

where q is the charge per unit length, l is the wire length and s the anode wire spacing.

The charge per unit length was given previously as

$$q = \frac{V_o}{2X}$$

V_o is the chamber voltage and X is a function of the geometrical configuration:

$$X = \frac{\pi L}{s} - \ln \frac{\pi d}{s}$$

where L is the anode to cathode spacing and d is the anode wire diameter

The total frame load with wires at the critical tension is

$$W = \frac{1}{s} t_c = \frac{q^2 l^3}{s^3} \qquad (10\text{-}2)$$

To calculate the frame load for a specific case we choose the large area chamber of Section 2 with $l = 66$ cm, with our geometrical configuration, i.e. L = 0.5 cm, s = 0.4 cm and d = 20×10^{-3} cm, 50×10^{-3} cm and 100×10^{-3} cm.

The critical tension and the total frame load are plotted in Figure 10-1 as a function of the operating voltage V_o which determines the charge per unit length. The solid curves cover the voltage range for which the relative gas gain was measured for Fe-55 x-rays in 80% Ar + 20% CO_2. (See Figure 4-2). The arrow indicates at which point the relative gas gain was 3.5×10^3. From the results of Figure 10-1 and equation (10-2), it is obvious that it is desirable to use small diameter, widely spaced anode wires to minimize the total frame load. According to our earlier results this condition is also preferable from an operational point of view, i.e. small diameter, widely spaced anode wires result in an increase in the maximum charge per unit length that can be accumulated and thus increases the strictly proportional region of the chamber.

The actual tension that will be put on the anode wires is above the critical tension but below the yield tension, so that any changes in wire tension due to temperature effects will keep the tension in a safe range from an operational and mechanical point of view.

Tensioning of the cathode wires is normally not as critical as tensioning of the anode wires. The tension mainly has to be large enough to prevent sagging of the cathode wires. In MWPC's with integral delay-line readout, however, tensioning of the cathode-or sense wires can be a problem since wires of rather large diameter (e.g. 150μ) have to be used to minimize

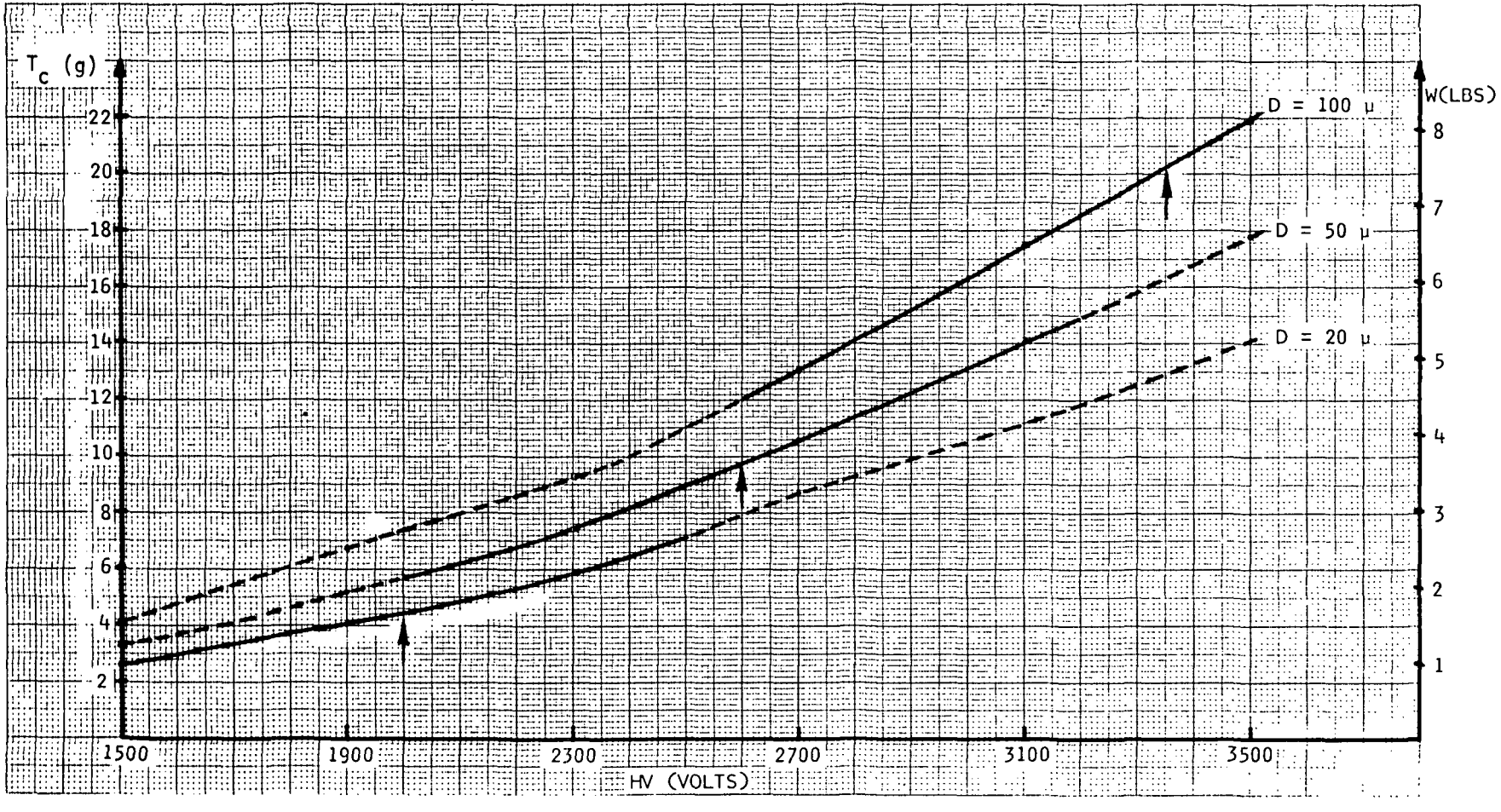

FIGURE 10-1 Critical anode wire tension t_c (in grams) and total frame load (in pounds) for a large area MWPC as a function of HV, arrows indicate HV at which the relative gas gain for Fe-55 x-rays is 3.5×10^3

the attenuation of the delay-line. Considerable tension has to be put on large diameter wires simply to keep them straight, and this can lead to rather large frameloads.

The frame material has to be limited to nonmagnetic materials, and since the frame also has to insulate anode from cathode planes, G-10 fiberglass is usually selected for the frame material. The disadvantages of G-10 are its outgassing characteristics and the possibility of creeping under long term, high loading. Other materials which are suitable are Mycalex-400, which is used as frame material for large area spark chambers for satellite experiments, and glass. Glass has very good mechanical and thermal properties and is very low in outgassing. Table X-1 summarizes some of the properties of G-10, Mycalex-400, and glass.

TABLE X-1

COMPARISONS OF FRAME MATERIALS

MATERIAL	DENSITY LB/CU IN	COEF. OF THERM. EXP. IN/IN/°F	TEN. STR. P.S.I.	YOUNG'S MOD. P.S.I.	SPEC. STIFF-NESS E/P	OUTGASSING
GLASS-SODA LIME	.090	5×10^{-6}	14,000	10×10^{6}	111	VERY GOOD
EPOXY GLASS G-10	.065	10.5×10^{-6}	40,000	2.5×10^{6}	42	POOR
MYCALEX-400	.108	10.5×10^{-6}	5,000	7.5×10^{6}		GOOD

REFERENCES

1. L. W. Alvarez et al., Superconducting Magnetic Spectrometer Experiment for HEAO, UCB SSL No. 374 (unpublished).
2. J. F. Ormes et al., Composition and Spectra of High Energy Cosmic Rays - A Proposal for an Orbiting Laboratory for the HEAO, GSFC-Report X-661-71-1, January 1971 (unpublished).
3. R. Golden et al., Proc. 12th Int. Conf. Cosmic Rays, Vol. 4, Paper TECH-21 and TECH-22, Hobart, Tasmania (1972).
4. G. Charpak et al., Nucl. Instr. Meth. 62, 262 (1968).
5. G. Charpak, Ann. Rev. Nucl. Sci. 20, 195 (1970).
6. R.Z. Fuzesy et al., Nucl. Instr. Meth. 100, 267 (1972).
7. R. Bouclier et al., Nucl. Instr. Meth. 88, 149 (1970).
8. F. Lacy (unpublished Report).
9. A.J.F. den Boggende et al., J. Sci. Instr. 2, 701 (1969).
10. G. Charpak et al., Nucl. Instr. Meth. 99, 279 (1972).
11. F. C. Tarle and H. Verweij, Nucl. Instr. Meth. 78, 93 (1970).
    J. R. Simanton et al., Nucl. Instr. Meth. 81, 13 (1970).
    R. Pages, Nucl. Instr. Meth. 85, 211 (1970).
12. H. Cunitz and W. Sippach, Nucl. Instr. Meth. 91, 211 (1971).
13. R. S. Larsen, IEEE Trans. Nucl. Sci. NS-19, No. 1,483 (1972).
14. R. Grove et al., Nucl. Instr. Meth. 89, 257 (1970).
    R. Grove et al., Nucl. Instr. Meth. 99, 381 (1972).
15. A. Rindi et al., Nucl. Instr. Meth. 77, 325 (1970).
16. D. P. Boyd et al., IEEE Trans. Nucl. Sci. NS-19, No. 3 , 148 (1972).
17. G. Charpak et al., Nucl. Instr. Meth. 65, 217 (1968).
18. D. M. Lee et al., Nucl. Instr. Meth. 104, 179 (1972).
19. J. R. Gilland and J. G. Emming, Nucl. Instr. Meth. 104, 241 (1972).
20. M. E. Rose and S. A. Korff, Phys. Rev. 59, 850 (1941).
    S. D. Curran and F. D. Craggs, Counting Tubes (Academic Press, New York, 1949) p. 32.
21. G. Bouclier et al., Ref. 7 and CERN NP Internal Report 70-2 (1970), unpublished.
22. J. Hough, Nucl. Instr. Meth. 105, 323 (1972).
23. J. Millman and H. Taub, Pulse, Digital and Switching Waveforms (McGraw-Hill, 1965), p. 798.
24. W. H. Barkas and M. F. Berger, Tables of Energy Losses and Ranges of Heavy Charged Particles, NASA SP-3013 (1964).
25. G. S. Hurst et al., F. Chem. Phys. 42 713 (1965).

BIBLIOGRAPHY

These papers have, for the most part, been published since the appearance of the review article by G. Charpak, "The Evolution of Automatic Spark Chambers", Annual Review of Nuclear Science, Volume 20, pp. 195-254 (1970), which contains an extensive list of prior references.

MWPC Systems - including construction, operation, and performance.

1. R. Bouclier et al., "Operation of Multiwire Proportional Chambers with Small Wire Spacing", CERN Internal Report NP 70-22, July 1970.
2. G. Charpak et al., "Some Developments in the Operation of Multiwire Proportional Chambers", Nucl. Instr. Meth. 80, 13 (1970).
3. C. Bemporad et al., "Performance of a System of Proportional Wire Chambers", Nucl. Instr. Meth. 80, 205 (1970).
4. L. J. Koester, Jr. et al., "Measurements of Efficiency and Time Resolution of Multiwire Proportional Counters", Nucl. Instr. Meth. 82, 67 (1970).
5. M. Atac and J. Lach, "High Spatial Resolution Proportional Chambers", Nucl. Instr. Meth. 86, 173 (1970).
6. R. Bouclier et al., "Investigation of Some Properties of Multiwire Proportional Chambers", Nucl. Instr. Meth. 88, 149 (1970).
7. P. Schilly et al., "Construction and Performance of Large Multiwire Proportional Chambers", Nucl. Instr. Meth. 91, 221 (1971).
8. A. H. Walenta et al., "The Multiwire Drift Chamber - A New Type of Proportional Wire Chamber", Nucl. Instr. Meth. 92, 373 (1971).
9. G. Charpak and F. Sauli, "Multiwire Chambers Operating in the Geiger-Muller Mode; New Simple Method of Particle Localization", Nucl. Instr. Meth. 96, 363 (1971).
10. G. Charpak et al., "Some Features of Large Multiwire Proportional Chambers", Nucl. Instr. Meth. 97, 377 (1971).
11. S. Parker et al., "Multiwire Proportional Chambers with Uniform Gain", Nucl. Instr. Meth. 97, 181 (1971).
12. J. Buchanan et al., "A multiwire Proportional Counter System for Use in Low, Medium, and High Energy Physics", Nucl. Instr. Meth. 99, 159 (1972).
13. E. Bloom et al., "A Proportional Chamber System for the Slac 20 GeV Spectrometer", Nucl. Instr. Meth. 99, 255 (1972).
14. T. Tomitani, "Analysis of Potential Distribution in a Gaseous Counter of Rectangular Cross-Section", Nucl. Instr. Meth. 100, 179 (1972).

15. V. D. Peshekhonov and Yu. V. Zanevsky, "Some Properties of Multiwire Proportional Chambers", Nucl. Instr. Meth. 100, 505 (1972).

16. R. Lanza and N. Hopkins, "Inexpensive Large Area Counters Using Multiwire Proportional Chambers", Nucl. Instr. Meth. 102, 333 (1972).

MWPC Applications - without MWPC details.

17. Z. Dimcovski et al., "High-Energy Charged Particles Separation by Means of a Cascade of Multiwire Proportional Chambers", Nucl. Instr. Meth. 94, 151 (1971).

18. B. Merkel, "A High Resolution Beam Hodoscope Using Multiwire Proportional Chambers", Nucl. Instr. Meth. 94, 573 (1971).

19. H. Becker et al., "A Multiwire Proportional Chamber for Use in a Magnetic Spectrograph of High Dispersion", Nucl. Instr. Meth. 95, 525 (1971).

20. H. Uto et al., "Detection of X-Ray Transition Radiation with Multiwire Proportional Chambers", Nucl. Instr. Meth. 97, 389 (1971).

21. T. Katsura et al., "Energy Resolution of a Multiwire Proportional Quantameter", Nucl. Instr. Meth. 105, 245 (1972).

MWPC Readout Techniques

22. J. C. Tarle and H. Verweij, "An Amplifier, Trigger and Memory for Signals from Proportional Wire Chambers", Nucl. Instr. Meth. 78, 93 (1970).

23. J. R. Simanton et al., "A Low Cost Amplifier/Discriminator/Limiter for Proportional Mode Wire Chambers", Nucl. Instr. Meth. 81, 13 (1970).

24. R. Pages, "Electronics Circuits Associated to Multiwire Proportional Chambers", Nucl. Instr. Meth. 85, 211 (1970).

25. R. Grove et al., "Electromagnetic Delay Line Readout for Proportional Wire Chambers", Nucl. Instr. Meth. 89, 257 (1970).

26. H. Cunitz and W. Sippach, "A 5000 Wire Proportional Chamber Readout System for A Large-Aperture Magnet Spectrometer", Nucl. Instr. Meth. 91, 211 (1971).

27. P. Y. Bertin and E. J. Planchard, "Systeme de Lecture D'Une Chambre Proportionnelle a Fils Au Moyen D'Une Ligne a Retard Magnetrostrictive", Nucl. Instr. Meth. 95, 493 (1971).

28. G. C. Bonazzola et al., "A Simple Coding System for Multiwire Proportional Counters", Nucl. Instr. Meth. 98, 273 (1972).

29. D. F. Jones and E. R. Martin, "A System for Separating Amplifiers from Wire Proportional Chambers", Nucl. Instr. Meth. 98, 535 (1972).

30. E. R. Martin and D. F. Jones, "A Fast Total Information Readout System for Multiwire Proportional Chambers", Nucl. Instr. Meth. 98, 541 (1972).

31. D. P. Boyd et al., "Coaxial and Printed Circuit Delay Lines for Multiwire Proportional Chamber Readout", IEEE Trans. Nucl. Sci. NS-19, No. 3,148 (1972).

32. R. S. Larsen, "Interlaboratory Development of an Integrated Circuit for Multiwire Proportional Chambers", IEEE Trans. Nucl. Sci. NS-19, No. 1, 483 (1972).

33. R. Grove et al., "Phase Compensated Electromagnetic Delay Lines for Wire Chamber Readout", Nucl. Instr. Meth. 99, 381 (1972).

34. D. Aebischer et al., "A Fast Process and Coding System for a Set of Multiwire Proportional Chambers", Nucl. Instr. Meth. 99, 405 (1972).

35. G. Fischer and J. Plch, "The High Voltage Readout for Multiwire Proportional Chambers,", Nucl. Instr. Meth. 100, 515 (1972).

36. J. G. Emming and J. R. Gilland, "A Multiwire Proportional Counter with Integral Readout Delay Line", IEEE Nucl. Sci. Symp.; Miami, Florida; Dec. 1972; to be published in IEEE Trans. Nucl. Sci.

37. D. M. Lee and S. E. Sobottka, "A Bifilar Helical Multiwire Proportional Chamber for Position Sensitive Detection of Minimum Ionizing Particles", Nucl. Instr. Meth. 104, 179 (1972).

MWPC Gas Properties

38. G. S. Hurst et al., "Ionization and Excitation of Argon with Alpha Particles", J. Chem. Phys. 42, 713 (1965).

39. R. W. Hendricks, "Space Charge Effects in Proportional Counters", Rev. Sci. Instr. 40, 1216 (1969).

40. A. J. F. den Boggende et al., "Comments on the Ageing Effect of Gas-Filled Proportional Counters", J. Sci. Instr. 2, 701 (1969).

41. G. Charpak et al., "Time Degeneracy of Multiwire Proportional Chambers", Nucl. Instr. Meth. 99, 279 (1972).

42. R. Z. Fuzesy et al., "A Gas Mixture for Multiwire Chambers with High Proportional Gain", Nucl. Instr. Meth. 100, 267 (1972).

43. L. E. Kline and J. G. Siambis, "Computer Simulation of Electrical Breakdown in Gases; Avalanche and Streamer Formation", Phys. Rev. A 5, 794 (1972).

44. R. W. Hendricks, "The Gas Amplification Factor in Xenon Filled Proportional Counters", Nucl. Instr. Meth. 102, 309 (1972).